

Epithelial paraphagy is a luminal lipophilic signal sensor and promotes transepithelial cholesterol clearance

Bao Li Zhang (Co-first)

1 School of Life Science and Technology, ShanghaiTech University; 2 Chinese Academy of Sciences, Center for excellence in Molecular Cell Science, Shanghai, China 3 University of Chinese Academy of S

Bao Ying Liu (Co-First)

1 School of Life Science and Technology, ShanghaiTech University; 2 Chinese Academy of Sciences, Center for excellence in Molecular Cell Science, Shanghai, China 3 University of Chinese Academy of S

Da Yuan Gao (Co-First)

1 School of Life Science and Technology, ShanghaiTech University; 2 Chinese Academy of Sciences, Center for excellence in Molecular Cell Science, Shanghai, China 3 University of Chinese Academy of S

Xin Zhou

1 School of Life Science and Technology, ShanghaiTech University; 2 Chinese Academy of Sciences, Center for excellence in Molecular Cell Science, Shanghai, China 3 University of Chinese Academy of S

Xin Yu Xu

1 School of Life Science and Technology, ShanghaiTech University; 2 Chinese Academy of Sciences, Center for excellence in Molecular Cell Science, Shanghai, China 3 University of Chinese Academy of S

Ze Peng Zhang

1 School of Life Science and Technology, ShanghaiTech University; 2 Chinese Academy of Sciences, Center for excellence in Molecular Cell Science, Shanghai, China 3 University of Chinese Academy of S

Xiao Kang Wu

1 School of Life Science and Technology, ShanghaiTech University; 2 Chinese Academy of Sciences, Center for excellence in Molecular Cell Science, Shanghai, China 3 University of Chinese Academy of S

Su Meng Shi

1 School of Life Science and Technology, ShanghaiTech University; 2 Chinese Academy of Sciences, Center for excellence in Molecular Cell Science, Shanghai, China 3 University of Chinese Academy of S

Stacey Cheng Zhang

School of Life Science and Technology, ShanghaiTech University,

Yuchuan Zhou

Jing Jiang

Genome Tagging Project (GTP) Center, State Key Laboratory of Cell Biology, Shanghai Key Laboratory of Molecular Andrology, CAS Center for Excellence in Molecular Cell Science, Shanghai

Hui-juan Shi

Shanghai Institute of Planned Parenthood Research

Shuo Shi

ShanghaiTech University

christopher antos

ShanghaiTech University

Tiffany Horng

ShanghaiTech University <https://orcid.org/0000-0002-9265-4559>

Jinsong Li

State Key Laboratory of Cell Biology, Shanghai Institute of Biochemistry and Cell Biology, Center for Excellence in Molecular Cell Science, Chinese Academy of Sciences <https://orcid.org/0000-0003-3456-662X>

Yonglian Zhang

Shanghai Institute of Biochemistry and Cell Biology, Chinese Academy of Sciences

Winnie Shum (✉ shumw@shanghaitech.edu.cn)

1 School of Life Science and Technology, ShanghaiTech University; 2State Key Laboratory of Cell Biology, Shanghai Institute of Biochemistry and Cell Biology, CAS Center for excellence in Molecular C <https://orcid.org/0000-0001-7575-6097>

Article

Keywords: Epithelial endocytosis, membrane trafficking, LC3-associated phagocytosis, tight junctions, occludin, membrane cholesterol, cholesterol clearance, low-affinity IgG receptor Fcgr2b, transepithelial lipid transport, ectopic lipid deposition inhibition, vitamin-K carboxylation, matrix Gla protein.

Posted Date: February 1st, 2021

DOI: <https://doi.org/10.21203/rs.3.rs-141184/v1>

License:   This work is licensed under a Creative Commons Attribution 4.0 International License.

[Read Full License](#)

1 **Epithelial paraghagy is a luminal lipophilic signal sensor and**
2 **promotes transepithelial cholesterol clearance**
3

4 Bao Li Zhang^{#1,2,3}, Bao Ying Liu^{#1,2,3}, Da Yuan Gao^{#1,2,3}, Xin Zhou^{1,2,3}, Xin Yu Xu^{1,2,3}, Ze Peng
5 Zhang^{1,2,3}, Xiao Kang Wu^{1,2,3}, Su Meng Shi^{1,2,3}, Stacey Cheng Zhang¹, Yu Chuan Zhou⁴, Jing
6 Jiang², Hui Juan Shi⁵, Shuo Shi^{1,6}, Christopher L. Antos¹, Tiffany Horne¹, Jin Song Li², Yong
7 Lian Zhang², Winnie Waichi Shum^{*1,2}

8
9 #Equal contribution.

10 *Correspondence: Winnie Shum (shumw@shanghaitech.edu.cn).

11
12 ¹School of Life Science and Technology, ShanghaiTech University, Shanghai 201210, China

13 ²State Key Laboratory of Cell Biology, Shanghai Institute of Biochemistry and Cell Biology,
14 Chinese Academy of Sciences, CAS Center for excellence in Molecular Cell Science, Shanghai
15 200031, China

16 ³University of Chinese Academy of Sciences, Beijing, China

17 ⁴International Peace Maternity and Child Health Hospital, School of Medicine, Shanghai Jiao
18 Tong University, Shanghai 200030, China.

19 ⁵Key Lab of Reproduction Regulation of NPFPC, Shanghai Institute of Planned Parenthood
20 Research, Reproduction and Development Institution, Fudan University, Shanghai 200032,
21 China

22 ⁶Shanghai Institute for Advanced Immunochemical Studies, ShanghaiTech University,
23 Shanghai 201210, China
24

25

26

27

28

29

30

31

32

33

34
35
36
37
38
39
40
41
42
43
44
45
46
47
48
49
50
51
52
53
54
55
56
57
58

ABSTRACT

Epithelial endocytosis is essential for physiological homeostasis. The current dogma is that all endocytotic mechanisms involve only single-membrane vesicles at the plasma membrane. Here, we report a previously undescribed LC3-associated phagocytosis mechanism which forms double-membrane phagosomes from the epithelial tight-junction paracellular membranes, which we term “paraphagy”. We observed that paraphagy is present in epithelia of the renal, respiratory, circulatory, and male reproductive systems. In the epididymis, paraphagy takes up lipophilic cargo, including apolipoproteins, by involving the surface low-affinity IgG-receptor Fcgr2b and occludin-bound intracellular HDL-receptor ATP5b. In this way, extracellular lipophilic signals are sensed and intracellular phagolysosomes are maintained. Occludin-null male mice show arrested paraphagy and impaired phagolysosome in proximal epididymal compartments, accompanying cholesterol accumulation, ApoJ deposition and dysregulated metabolic-dependent processes in distal compartments, including redox-promoted VK-dependent MGP-carboxylation. We propose that paraphagy senses and distinguishes the luminal lipophilic signals in epithelia and modulates their function via crosstalk across physiological compartments.

Key words: Epithelial endocytosis; membrane trafficking, LC3-associated phagocytosis; tight junctions; occludin; membrane cholesterol; cholesterol clearance; low-affinity IgG receptor Fcgr2b; transepithelial lipid transport; ectopic lipid deposition inhibition; vitamin-K carboxylation; matrix Gla protein.

INTRODUCTION

Epithelium is the frontline barrier for physiological homeostasis and protection of a host. Epithelial cells are biologically engineered to tackle both general and organ-specialized

59 physiological demands, in addition to the defence against pathogenic challenges and the
60 maintenance of effective communication between external and internal environments of organs.
61 They are therefore able to carry out tremendous material exchanges and signal transduction to
62 fulfil all these processes by involving intricate vesicle endocytosis and exocytosis¹⁻³. All these
63 activities occur along epithelia made up of epithelial cells that are connected using tight
64 junctions (TJs) at the apical paracellular plasma membranes to form a tight barrier. Epithelial
65 endocytosis is the primary step of material exchanges and extracellular-to-intracellular signal
66 transduction. It also allows epithelial cells to sample the extracellular milieu and to control
67 plasma membrane homeostasis by membrane internalisation⁴⁻⁶. Thus, modulation of epithelial
68 endocytosis, particularly TJ endocytosis, controls physiological functions and homeostasis,
69 however, the TJ endocytosis mechanism is not fully understood.

70

71 The current understanding of endocytotic pathways in cells is that all endocytosis
72 events involve single membrane vesicle process. They are broadly categorised into two main
73 types either based on vesicle size (i.e. phagocytosis or pinocytosis) and on vesicle coat proteins
74 (e.g. CME for Clathrin-Mediated Endocytosis and CIE for Caveolae- and Clathrin-Independent
75 Endocytosis)⁷⁻¹⁰. These types are then subdivided based on their membrane features, *viz.* CME
76 in non-lipid-raft membrane domains; phagocytosis and macropinocytosis in mixed domains,
77 and CIE in rafted domains⁷⁻¹⁰. Intriguingly, LC3-associated phagocytosis (LAP), characterised
78 by external single-membrane phagosomes originating from plasma membranes of cells by
79 recruiting autophagic machinery, is also an essential type of endocytosis¹¹⁻¹⁷.

80

81 Cholesterol is a central molecule for cell membrane properties and steroid hormone
82 synthesis. Both are also subject to the regulation of endocytosis^{18,19}. Cholesterol aberrant
83 accumulation associates with many metabolic diseases. Cholesterol clearance in non-adipose

84 tissues is known²⁰⁻²². However, this physiological demand is particularly heavy in epididymis,
85 where spermatozoa have to go through maturation processes by replacing their membranes
86 enriched with cholesterol and saturated fatty acids with new membranes with high
87 polyunsaturated fatty acids (PUFA) for the motility and fertilization competence^{19,23-27}.
88 Cholesterol overload has been clearly associated with male infertility²⁷⁻²⁹ and metabolic
89 syndrome in infertile patients^{26,30,31}, however, the mechanisms involved in regulating
90 cholesterol homeostasis in plasma membrane are still unclear.

91

92 It has been reported that loss of occludin (Ocln), a known TJ protein, results in male
93 infertility³². The cause of this phenotype remains elusive. Using epididymis as an epithelial
94 model in *Ocln*-KO male mice, we found a new unconventional phagocytosis that regulates
95 membrane cholesterol and is featured by forming double-membrane phagosome—a dogma of
96 canonical autophagy thought to occur only intracellularly^{33,34}—derived from the plasma
97 membranes of epithelial TJs and. This process, which we term paracellular heterophagy or
98 paraphagy, involves the interaction of Ocln at the TJs with the participation of autophagy
99 protein LC3 and Fcgr2b receptor for lipophilic cargo endocytosis to promote cholesterol
100 removal from TJ plasma membranes. We also provide evidence that this is a general
101 mechanism applicable to other epithelia, including airway bronchia, renal tubules, digestive
102 intestine and circulation endothelium, but is particularly profound in epididymis in
103 reproductive tract. Thus, we show that paraphagy at TJs is a novel mechanism which senses
104 the luminal lipophilic signals and modulates cholesterol homeostasis in epithelia.

105

106

RESULTS

107 ***Ocln*-KO mice have arrested Ω -shaped double-membrane vesicles at peri-TJ paracellular**
108 **membranes and downregulated phagolysosomes in epithelial cells**

109 To understand the cellular consequence of the loss of Ocln, we examined the junctional
110 integrity of epididymal epithelium using high-pressure-freeze (HPF)-TEM. We observed
111 plasma membrane-associated Ω -shaped double-membrane vesicles (pm- Ω -DMVs, \sim 300 nm in
112 diameter) were detected beneath the TJ membrane of caput epididymal principal cells (Fig.
113 1a), a region that displayed enriched Ocln expression (Fig. S1-2). These pm- Ω -DMVs occurred
114 more frequently in the *Ocln*-KO males and might have been derived from the TJ surface, as
115 matured DMVs, a hallmark of autophagosomes with a similar composition to TJ membranes
116 immediately beneath the TJ surface of the KO principal cells (Fig. 1a double-arrow). Only the
117 pm- Ω -DMVs were significantly increased in the KO caput cells, whereas, the phagolysosomes
118 were decreased (Fig. 1a'), the latter consistent with depletion of lysosome markers Lamp1 and
119 Rab7 and the loss of F-actin-positive macrovesicles (Fig. S3). Quantification of vesicles
120 adhering to paracellular membranes showed that only the vesicles (non-DMVs) with greater
121 diameters (\sim >0.35 μ m) were significantly decreased in the KO caput principal cells (Fig.1b).

122 To explore the molecular nature of the pm- Ω -DMVs, *i.e.* paraphagosomes, we
123 examined the cellular localisation of TJ-paracellular membrane markers claudins³⁵. We found
124 that the localisation of claudin-3 (Cldn-3), but not claudin-1 or -4, was related to these
125 structures in WT caput segment, and that it was accumulated near the TJs of KO caput principal
126 cells (Fig. S4). Double-immunolabelling of Cldn-3 and the TJ marker ZO1 highlighted
127 numerous heterogeneous vesicles adhering to the paracellular TJs of WT caput principal cells
128 (Fig. 1c). No heterogeneous vesicles were observed to adhere to paracellular TJs of KO
129 principal cells of the same epididymal region. We then examined the epididymal epithelium
130 from HA-Ocln mice and found the same vesicular structures in the principal cells of the same
131 region (Fig. 1d). Similar HA-Ocln-labelled vesicular structures were also present in the TJs of
132 bronchi and kidney mucosa (Fig. 1e-f), and vascular endothelium (Fig. 1g), but not in testis or

133 trachea (Fig. 1h and 1i). OcIn-labelled vesicular structures were also observed in human small
134 intestine (Fig. 1j). Thus, OcIn ablation led to the TJs' accumulation of paraphagosome.

135

136 **OcIn is essential for membrane dynamics but not epithelial TJ integrity and barrier**
137 **function**

138 To further assess TJ integrity, we examined the apical junctional structures of principal cells at
139 the caput epididymidis, where OcIn is abundantly expressed. We found no difference in the
140 lengths of TJs or zonula adhaerens between epithelial cells WT and *OcIn*-KO mice (Fig. 2a);
141 however, the adhesion junctions between paracellular membranes of adjacent principal cells
142 were prominently increased in mice lacking OcIn (Fig. 2a'). We tested the tissue barrier
143 integrity of WT and KO mice by lanthanum perfusion and observed that no tracer penetrated
144 beyond the junctional complexes (Fig. 2b). We also perfused biotin and found no difference in
145 penetration to the lumen of the epididymis by immunofluorescence detection in WT and KO
146 animals (Fig. 2c). Furthermore, we observed no difference in epithelial resistance and
147 impedance parameters of the monolayers of WT and *OcIn*-KO DC2 cells using electric cell-
148 substrate impedance sensing measurement (Fig. 2d). These results confirmed the epithelial
149 barrier integrity in the epididymis of *OcIn*-KO animals.

150 When we performed TEM image analyses, we observed the paracellular membrane of
151 KO epithelial cells were thinner than WT cells, which we confirmed with quantification
152 analysis (Fig. 2e). Our further analyses indicated higher cholesterol level, lower membrane
153 fluidity and overload of the lipoprotein conjugator DiD in the organelles in the *OcIn*-KO DC2
154 (Fig. 2f-h). Consistent with these observations, expressing OcIn but not its deletion mutant in
155 DC2 cells was able to increase membrane activities of DC2 cells, with many vesicles around
156 the highly convoluted paracellular membranes (Fig. 2i), suggesting the loss of membrane

157 dynamics in the *Ocln*-KO DC2 cells. As expected, expressing Ocln in *Ocln*-KO cells can rescue
158 the phenotype (Fig. 2i'). Finally, organelles appeared to be arrested during membrane fusion
159 events in the caput principal cells of *Ocln*-KO mice (Fig. S5). Thus, *Ocln*-KO cells displayed
160 disordered membrane dynamics and apposition events.

161

162 **Ocln is required for transepithelial transport and prevents cholesterol accumulation in** 163 **epithelia of mice**

164 A permeability assay involving 3 kDa dextran showed no difference in the first 30 min in WT
165 and KO DC2 monolayer cells (Fig. 2j), suggesting there was no difference in paracellular
166 transport, which is expected to occur at a higher rate than transcellular transport³⁶. However,
167 we consistently found that dextran permeability was significantly decreased in the KO cells,
168 indicating impaired transepithelial transport.

169

170 The membrane dynamic disorders and cholesterol overload in cultured cells suggested
171 cholesterol overload in the *Ocln*-KO mice. This was true in all epididymal segments.
172 Specifically, in the KO epididymis, cholesterol accumulated in apical domains and paracellular
173 membranes of epithelial cells of entire regions of the epididymis (Fig. 2k), as well as in the
174 luminal contents throughout the tubule (Fig. 2k'), and particularly in the acrosome and
175 midpiece of KO spermatozoa (Fig. 2l). Cholesterol also accumulated in the mucosa of kidney
176 and liver of KO mice (Fig. 2l' and l'').

177

178 **Ocln regulates phagosome-associated cholesterol transport and metabolic pathways**

179 To explore how *Ocln*-KO leads to paraphagosome arrest and complex physiological
180 phenotypes, we investigated the transcriptomes and proteomes from the caput segment and

181 whole epididymis, respectively; we analysed differentially expressed genes (DEGs) with an
182 integrative approach by combining RNAseq and proteomic datasets (Fig. S6-8) and the KEGG-
183 based PathActNet analyses. We summarized the results as the Cytoscape plots (Fig. 3a). We
184 found in the caput-only dataset that the gene clusters of the phagosome and lipid-metabolic
185 pathways involving cytochrome/quinone gene components were the top-scored pathways,
186 while the vesicular trafficking to the lysosome component, which was the common
187 downstream effector of the phagosome pathway and the Fc-gamma receptor-mediated
188 phagocytosis pathway, was the unique down-regulated pathway within this dataset. In the
189 whole epididymis analysis, genes in the metabolic pathways of glycosphingolipid and hormone
190 biosynthesis pathway were those down-regulated, while the pathways of infectious diseases-
191 related genes were the primarily up-regulated with the phagosomes enriched gene cluster as
192 the downstream pathway.

193

194 The cholesterol accumulation in *Ocln*-KO tissues, together with the bioinformatic
195 identification of lipid-metabolic pathways identified, suggested that cholesterol homeostatic
196 pathways might be dysregulated in *Ocln*-KO animals. We thus investigated the expression
197 profiles of the genes in related pathways. In the whole epididymis dataset, we observed no
198 change in gene expressions of cholesterol synthesis and Liver X receptor (Lxr) pathways,
199 though a mild downregulation of transcription was observed in the caput-only dataset (Fig. 3b).
200 We attributed these results to a compensation mechanism in response of the disorder of other
201 pathways and we concluded that this pathway is a secondary effector rather than primary cause
202 of defects in *Ocln*-KO animals. Our transcriptomic and proteomic results showed that the lipid
203 carriers ApoJ was the most abundant lipid carrier in the epididymis. We observed other
204 apolipoproteins at lower levels in the proteomes (Fig. 3c). In the KO epididymis, ApoJ was
205 significantly upregulated, indicating that the lipid-metabolic disorder in *Ocln*-KO epididymis

206 is related to cholesterol transport. Supporting this hypothesis was the disordered expression
207 levels of apolipoprotein uptake receptors (Fig. 3d). Most genes in intracellular cholesterol
208 trafficking pathway were significantly downregulated (Fig. 3e), as were the genes of
209 cholesterol efflux and scavenging pathways, with high expression levels in caput epididymidis
210 (Fig. 3f). Overall, we conclude that cholesterol accumulation in *Ocln*-KO animals was
211 primarily caused by dysregulation of cholesterol transport and trafficking pathway(s) rather
212 than *de novo* synthesis or transcription regulation.

213

214 ***Ocln*-KO results in dysregulated membrane proteins with long-TMDs**

215 We found that over 50% of the DEGs were not associated with reported KEGG pathways (see
216 Fig. S4d); therefore, we performed subsequent analyses manually (Fig. S9-S10), on the basis
217 of two rationales. The first is that the arrested paraphagy events in the *Ocln*-KO epididymis
218 leads to the accumulation of specific membrane proteins at the plasma membranes or
219 specialised compartments. The second is that the longer transmembrane domains (TMDs) of
220 the Ocln protein is its unique property such that other proteins, *e.g.* claudins, with shorter TMDs
221 are unable to compensate^{37,38}. The latter hypothesis was supported by the results that 12 of 118
222 DEGs (10%) were shortlisted to contain long TMDs in the caput-only downregulated dataset
223 versus only 2 in 68 DEGs (3%) in the whole epididymis dataset (Fig. 3g). We thus conclude
224 that the membrane proteins with long TMDs are dysregulated in the membranes of TJs and
225 organelles after *Ocln* ablation. A hypothetical physiological model is proposed for the role of
226 Ocln-promoted paraphagy at TJs as the primary entry step for cholesterol transepithelial
227 transport from luminal side of WT epididymal epithelium towards basolateral side, and this
228 process is interrupted in Ocln ablation and resulted in cholesterol accumulation (Fig. 3h).

229

230 **Ocln-promoted paraphagy prevents ectopic apolipoprotein ApoJ deposition**

231 Our current results and other studies^{39,40} show that ApoJ is the key lipid carrier in the epididymis.
232 Confocal immunofluorescence analysis showed high abundance of ApoJ in the large vesicular
233 organelles of WT proximal caput principal cells (Fig. 4a), which were decreased in the same
234 region of KO mice, as revealed in the scatter plots. In the distal caput region, the high-ApoJ
235 larger organelles diminished in the WT; whereas, in the KO caput principal cells, numerous
236 intermediate-size vesicles were still present. In the subsequent distal regions of epididymis,
237 ApoJ levels were increased in the KO epithelium and in the lumen, suggesting increased ApoJ
238 secretion. We also found increased ApoJ in the principal cells of kidney cortical collecting
239 ducts of *Ocln*-KO mice (Fig. 4b). Thus, we concluded that the ectopic increase in ApoJ
240 expression in the *Ocln*-KO epithelium is a general phenomenon.

241

242 **Fcgr2b is the surface receptor associated with paraphagy at the TJs**

243 Interestingly, we observed no immunostaining signals for the classical apolipoprotein receptors
244 Lrp1 and Lrp2 in the apical surface of caput epithelial cells of adult mice (Fig. 4c). We then
245 investigated the shortlisted DEGs membrane proteins and found that low-affinity IgG Fc
246 fragment receptor Fcgr2b is one of them, showing significantly accumulated Fcgr2b protein
247 but downregulated mRNA in *Ocln*-KO. Consistently, Fcgr2b was located at the TJs of WT
248 caput cells, accompanying endocytotic structures extending underneath the TJs (Fig. 4d, arrows
249 in 3D-serts). Whereas it was accumulated and contained in close proximity to ZO1-labelled
250 TJs in the *Ocln*-KO caput cells (Fig. 4d' and d''). We detected the co-localisation of Ocln with
251 Fcgr2b on the plasma membranes of Ocln-GFP transfected cells (Fig. 4e). The colocalization
252 of Fcgr2b and ZO1 at the TJs were also found in the other epithelial tissues, including epithelial
253 cells of kidney collecting duct, small intestine, bronchia and endothelium (Fig. S11),

254 suggesting that Fcgr2b functions as a non-classical lipophilic receptor and that this is a general
255 mechanism in these epithelia.

256

257 **Ocln-promoted paraphagy maintains MGP-carboxylation to facilitate apolipoproteins**
258 **scavenging by involving Fcgr2b**

259 To correlate the complex phenotypes in *Ocln*-ablated animals with the arrested paraphagy in
260 the upstream compartments but ApoJ and cholesterol ectopic accumulation in the downstream
261 compartments, in addition to the loss of membrane dynamics and accumulation of Fcgr2b at
262 the TJs in *Ocln*-KO cells, we thus speculated that Fcgr2b functions as the receptor for ApoJ
263 apolipoproteins. Consistently, the colocalization of Fcgr2b and ApoJ was observed in the apical
264 domain of epididymal caput cells (Fig. 4f). We further speculated that the shortlisted long-
265 TMDs DEGs identified from our bioinformatic analysis is associated with the ApoJ ectopic
266 deposition in the epididymis. We identified that the *Vkorc1* protein is one of the shortlisted
267 long-TMDs DEGs and found that *Vkorc1* and other proteins of the VK-dependent
268 carboxylation pathway were downregulated in *Ocln*-KO caput epididymidis (Fig. S12). We
269 attributed the downregulation of *Vkorc1* transcription to the impaired paraphagic uptake of
270 transcriptional factor or depleted phagolysosomal signalling or both. *Vkorc1* is a redox-
271 sensitive membrane enzyme and maintains the VK cycle that activates matrix Gla-protein MGP
272 by *Ggcx*-mediated carboxylation⁴¹. Carboxylated MGP is a well-known ubiquitous inhibitor of
273 ectopic calcification. We have reported that MGP is highly expressed in the epididymis and
274 that the activated MGP chelates numerous phospholipids and lipid carriers to form aggregates
275 by binding with extracellular calcium⁴². Since we found that ApoJ is abundant in the MGP-
276 calcium aggregated proteomes of rat kidney and epididymis⁴², we propose that downregulated
277 *Vkorc1* in the *Ocln*-KO leads to impaired MGP carboxylation and dampens its function in
278 preventing ectopic ApoJ deposition. To test this, we analysed the cellular distribution of MGP

279 by immunofluorescent labelling on cryosections of epithelial sections from *Ocln*-KO and WT
280 mice. We observed the co-localisation of Ocln with MGP on the plasma membranes of Ocln-
281 GFP transfected cells (Fig. 4g), suggesting the Ocln-promoted paraphagy is a pathway
282 mediating the calcium-facilitated MGP chelating of ApoJ and other aggregates. Consistently,
283 granular vesicles double-labelled with ApoJ and MGP were also observed in the apical surface
284 as well as in some intracellular vesicles in the epithelial cells of epididymis, airway and kidney
285 of WT mice (Fig. 4h). In addition, we also observed Vkorc1 present in Rab7-positive vesicles
286 in WT but not KO caput principal cells (Fig. 4i), suggesting the involvement of Rab7 in
287 Vkorc1-dependent carboxylation process. We found that the overall MGP
288 immunofluorescence was decreased in the KO epididymis (Fig. S13a). However, the
289 immunofluorescence of Gla-proteins, all the VK-dependent carboxylation products, was
290 increased in the entire length of epididymal epithelium (Fig. 4j and S13b) as well as kidney
291 glomerulus and airway alveoli (Fig. 4k and S14). These results are consistent with the notion
292 of compensatory mechanism for Vkorc1⁴³, as well as the presence of uncharacterised
293 carboxylation protein substrate(s). However, other Gla-proteins might not be as effective as
294 MGP in preventing ApoJ deposition. We conclude that carboxylated MGP, the extracellular
295 calcium chelator, facilitates ApoJ uptake via Ocln-promoted paraphagy and that Ocln ablation
296 results in a carboxylation disorder and MGP-dependent ectopic ApoJ accumulation in multiple
297 organs of *Ocln*-KO mice.

298

299 **Ocln facilitates rafted plasma membrane microdomain retrieval and recycling via bulk-** 300 **endocytosis**

301 As our results showed that Ocln promotes the uptake of bulky lipophilic cargo, we speculated
302 that paraphagy is a clathrin-independent pathway that involves cholesterol-rich raft
303 microdomains^{7,10}. To investigate this hypothesis, we performed endocytosis assays with raft

304 stain CTxB-FITC. CTxB binds to GM1, a ganglioside receptor on the membrane, and its
305 accumulation is correlated with the membrane cholesterol content⁴⁴. From these assays, we
306 observed that CTxB endocytosis in KO cells was obviously slower in WT cells at 2 min (Fig.
307 5a). The decrease in CTxB-FITC endocytosis was associated with CTxB accumulation at the
308 plasma membranes of KO cells, whereas CTxB-FITC intensity was higher in the intracellular
309 vesicles of WT cells. However, after 5 min the CTxB-FITC intensity at the plasma membrane
310 of KO cells became significantly less (Fig. 5a and S15), indicating that CTxB-microdomain
311 recycling is defective in KO cells.

312

313 To characterise the membrane recycling dynamics further, we used a patch-clamp
314 method to measure the passive membrane properties of the cells (Fig. 5b and S16). Endocytosis
315 recycles fused vesicles upon exocytosis to maintain plasma membrane homeostasis. This
316 phenomenon involves pinching off regions of the bilipid membrane from the plasma membrane.
317 Endocytosis decreases the surface area of the plasma membrane⁵, while exocytosis, which
318 fuses vesicles to the plasma membrane, increases the surface area^{45,46}. These changes are
319 associated with changes in cell capacitance because it is proportional to the area of the plasma
320 membrane, and thereby the changes in capacitance over time can be interpreted as changes of
321 surface area⁴⁷. We observed that the WT DC2 cells tended to exhibit smaller initial capacitance,
322 with values of 9.9 ± 3.3 pF ($n = 11$) compared with *Ocln*-KO cells values of 15.0 ± 6.0 pF (n
323 $= 7$), although there was no statistical difference. This corresponds to a membrane of about
324 $1000 \mu\text{m}^2$, roughly that of a spherical cell of diameter of $\sim 18 \mu\text{m}$ for WT and $\sim 22 \mu\text{m}$ for KO,
325 assuming $1 \mu\text{F}/\text{cm}^2$ unitary specific capacitance⁴⁶. The larger cell membrane capacitance of KO
326 cells suggests altered membrane events in these cells.

327

328 We analysed the passive membrane properties of individual cells, including cell
329 capacitance and transient current time constant—an indicative of membrane dynamics—by the
330 measurements from the transient current responses obtained by repeatedly applying a
331 hyperpolarising step to -70 mV from the holding potential of 0 mV at 5 sec intervals. Our
332 results showed that upon hyperpolarisation WT DC2 cells activated at least two types of
333 exocytotic mechanisms, one small fast component occurring infrequently and a slow but larger
334 component with a lag-time of tens of seconds (Fig. 5b-a). The second component was usually
335 accompanied with a small wane of capacitance before the prominent raise (arrows in Fig. 5b-
336 a), which implies a decrease in membrane capacitance, *i.e.* endocytosis, occurring before the
337 slow component of exocytotic events. In KO cells, instantaneous exocytotic mechanisms occur
338 consistently; however, the activities of the second slow component was significantly impaired.
339 Digital subtraction of hyperpolarised-induced capacitance (Fig. 5b-b) from that of
340 repolarisation-induced responses (Fig. S16f), revealed a slow endocytotic component with a
341 lag-time of ~ 35 sec in WT cells (Fig. 5b-c, arrow), however, this component was completely
342 absent from *Ocln*-KO cells (Fig. 5b-c). The time-constant of the transient current upon
343 hyperpolarisation, an indicative of membrane dynamics, was significantly smaller and
344 quiescent in KO cells than in WT cells in the first 200 sec of recording (Fig. 5b-d), suggesting
345 less membrane activity in these cells. It is worthwhile mentioning that some membrane
346 activities were activated prominently in KO and moderately in WT cells during the intense
347 hyperpolarisation-repolarisation stimulation after 200 sec (Fig. 5b-b,c). It seems to be a simple
348 mechanism, merely in response to voltage changes, that protects cells from intensive
349 stimulation. The smaller resting conductance in KO *versus* WT cells implies the incapability
350 to recycle the electrogenic transporters across the plasma membrane (Fig. 5b-e), consistent
351 with our immunofluorescence results showing dislocation of the electrogenic transporter

352 Slc1a1 in *Ocln*-KO caput epithelium (Fig. 5c), and likely involving other long TM transporters
353 (see Fig. 3g).

354

355 Our observations that *Ocln* is involved cholesterol levels and endocytosis suggest that
356 molecules involved in cholesterol sensing in the plasma membrane may be involved. It has
357 been reported that flotillin plays important functions in raft-dependent clathrin-independent
358 endocytosis⁴⁸ and membrane cholesterol sensing⁴⁹. We then determined if flotillin-1
359 microdomain was involved in paraphagy. We observed that in WT caput cells flotillin-1 was
360 present in the intracellular vesicular organelles, the TJs and paracellular membranes (Fig. 5d
361 and S17) while in KO cells, the number of flotillin-positive vesicles was significantly decreased.
362 This accompanied decreased staining for flotillin in the peri-apical membranes but increased
363 staining in lower part of paracellular lateral membranes (Fig. 5e). Co-localisation of flotillin
364 with *Ocln*-N-GFP was found in the paracellular membranes and is likely present in the nascent
365 vesicles from plasma membrane (Fig. 5f insert). It is known that caprin1 is an endocytotic
366 substrate of flotillin1-microdomains, also known as GPI-anchored RNA-binding protein
367 (RBPs)^{50,51}. This result suggests that *Ocln* facilitates paraphagytotic uptake of RBPs via a
368 flotillin-aided microdomain mechanism, which might be related to the ribosomal proteins (RPs)
369 as found in the *Ocln*-flag interactomes (see Fig. 7a).

370

371 Acidification of vesicles is involved in vesicle maturation and trafficking^{52,53}. To
372 understand whether *Ocln*-mediated endocytosis is associated with traffic of vesicles to acidic
373 endosomes, we performed live-cell imaging of N-GFP-*Ocln* DC2 cells loaded with lysotracker
374 (Fig. 5g). The results showed that heterogeneous vesicles formed dynamically from the *Ocln*-
375 expressed paracellular membranes of adjacent cells. Some *Ocln*-positive endocytotic vesicles

376 diffused laterally along the plasma membrane before invaginating and separating from the
377 membrane (Fig. S18). Interestingly, these vesicles were elongated after the first invagination,
378 suggesting membrane expansion before the completion of detachment from the membrane. We
379 observed no co-localisation for these vesicles with lysotracker was observed, suggesting that
380 Ocln-mediated endocytosis does not directly involve acidic organelles, such as endosomes.

381

382 **Ocln-promoted paraphagy involves autophagy protein LC3 but not Beclin-1**

383 Our results suggested that Ocln-promoted paraphagic endocytosis does not directly involve
384 acidic endosomes but is essential for the degradation of ApoJ⁺ vacuoles, which are associated
385 with Rab7 that is also known to be essential for late autophagic vacuoles maturation^{54,55}. We
386 speculated that autophagy mechanisms are involved in Ocln-dependent paraphagic events and
387 thus investigated the DEGs in caput omics datasets (Fig. 6a). We found that only Map1Lc3a
388 (LC3a) was significantly downregulated. We confirmed this observation by immunostaining
389 with a pan-LC3 antibody (Fig. 6b). LC3 was located in the endocytotic vesicles in the apical
390 surface of IS principal cells (Fig. 6b arrow) and in the large phagocytotic-like vesicles near the
391 TJ paracellular membranes of caput principal cells (Fig. 6b double-arrow). We observed co-
392 localisation of Ocln and LC3 was observed in the plasma membrane of Ocln-GFP and LC3-
393 RFP co-transfected DC2 cells (Fig. 6c). Double-labelling showed that LC3 colocalises with
394 ZO1 at the TJs of WT proximal caput cells, particularly in close proximity to the paraphagy-
395 like structures (Fig. 6c). In the KO, LC3 expression and paraphagy-like events were
396 significantly decreased. Noteworthy, in the WT caput cells the LC3-labeled intensity was not
397 only higher in the close proximity of ZO1-labeled TJs (Fig. 6e arrows) but was also present
398 inside the enlarged paraphagy-like structures extending from the ZO1-labeled TJs (Fig. 6e
399 asterisks). This phenomenon supports the hypothesis that LC3 is involved in paraphagosome
400 biogenesis at the TJ membranes, as a mechanism similar to autophagy initiation³³. The co-

401 localisation of LC3 with ApoJ⁺ vesicles was more frequent in WT than in *Ocln*-KO caput cells
402 (Fig. 6f). Another LC3-associated phagocytotic LAP protein Beclin1¹¹ has been reported to
403 colocalise with Ocln in the intestine⁵⁶, however, we observed no Beclin1 immunofluorescence
404 in the epididymal TJs with the same antibody (Fig. 6g). Overall, our results suggest that Ocln-
405 promoted paraphagy at TJ membranes involves LC3 but not beclin-1, but our results do not
406 exclude other non-conventional autophagy and LAP proteins being involved in paraphagy in
407 the epididymis.

408

409 **Ocln promotes the transport of ApoA1 and ApoJ to ATP5b in the proximal epididymidis**

410 To identify Ocln targets responsible for altered paraphagy phenotype, we analysed the
411 immunoprecipitated Ocln-flag proteins by IP-MS and found that four key proteins ATP5b,
412 Hsp90, Ppia and Capzb precipitated with Ocln. According to a protein cluster analyses, these
413 proteins are associated with endocytosis, chaperone cycle, antigen presentation and organelle
414 biogenesis and maintenance (Fig. 7a and Fig. S19a). Capzb was present in the intracellular
415 vesicular compartment of WT caput principal cells, but it was almost absent from the same
416 region of the *Ocln*-KO, although it was still located at the TJ compartment (Fig. S19b). A larger
417 gap between Ppia-labelled extracellular matrix and TJ surface was observed in the *Ocln*-KO
418 caput cells compared to *Ocln* WT animals (Fig. S19c). The chaperone protein Hsp90 was
419 increased in the caput epididymidal lumen and on the apical surface of principal cells of *Ocln*-
420 KO mice (Fig. S19c, double-arrow). The interaction of ZO1 with Hsp90 at the TJ membrane
421 was less extensive in *Ocln*-KO compared with WT caput cells. All these results indicated the
422 role of Ocln in promoting uptake of lipophilic matter.

423

424 As ATP5b is a receptor for high-density lipoprotein (HDL) ApoA1 and a subunit of
425 F1/F0 ATP synthase in mitochondria⁵⁷, we proposed that Ocln might bind ATP5b and takes up
426 lipoproteins, subsequently transporting them directly or indirectly to mitochondria. We also
427 proposed that the failure of these cargoes to meet their fates in specialised compartments
428 underlies the metabolic disorders in *Ocln*-KO mice. We first confirmed the interaction of Ocln-
429 Flag with ATP5b by IP followed with WB analysis (Fig. 7a). Immunofluorescence labelling
430 showed that ATP5b was intracellularly expressed but sparsely co-localised with Ocln-GFP in
431 transfected cells (Fig. 7b). We speculated that the interaction of ATP5b and Ocln occurs more
432 frequently in epithelium *in vivo*. Supporting our hypothesis, we observed numerous co-
433 localisations of ATP5b and HA-Ocln beneath the TJ of mouse caput principal cells (Fig. 7c
434 and S20a,c). We also observed decreased ATP5b immunofluorescence in distal segments of
435 the *Ocln*-KO epididymis compared with WT, consistent with the notion of downregulated
436 metabolism in the *Ocln*-KO (Fig. 7d and 7e). Thus, our results identified ATP5b as an Ocln
437 intracellular target.

438

439 We found no detectable ApoA1 transcripts but abundant proteins in the epididymis (see
440 Fig. 3c). The strong ApoA1 immunofluorescence in the basal lamina of WT caput epididymidis
441 was decreased in the KO compared with WT caput epididymidis (Fig. 7d). In distal epididymal
442 regions, the ApoA1-labelled large cellular debris surrounding WT spermatozoa acrosomes was
443 absent from KO spermatozoa, but weak signals around the stereocilia of KO principal cells
444 were detected (Fig. 7d). Co-localisation of ApoA1 and ATP5b around mitochondria was more
445 frequent in WT than in KO caput cells (Fig. 7e). Co-localisation of ApoA1 and HA-Ocln in
446 the cargo near the luminal surface of the caput epithelium was strong, while weak signals were
447 present in the paracellular membranes and some intracellular vesicles of principal cells (Fig.
448 7f). These results suggested that ATP5b facilitates ApoA1 transepithelial transport, which is

449 dysregulated in the *Ocln*-KO caput epithelium and that the ApoA1 is responsible for the
450 impaired transepithelial transport of cholesterol.

451

452 To determine whether ApoJ interacts with Ocln and to find out where possible
453 interactions occur, we performed immunohistochemistry for each protein on the same
454 cryosections. We observed co-localisation at the apical tight junction, where it was also in close
455 proximity to large ApoJ-positive (ApoJ⁺) vesicular organelles (the paraphagosomes) that were
456 likely derived from plasma membranes and that we call paraphagosomes (Fig. 7g and S20b,d).
457 This supported the notion that Ocln can take ApoJ up at the TJ membranes by paraphagy. The
458 co-localisation of ApoJ and ATP5b in WT proximal caput principal cells (Fig. 7h) suggested
459 the participation of ATP5b in intracellular ApoJ transport. In WT distal caput principal cells,
460 most ApoJ⁺ granules were diminished and showed weak co-localisation with ATP5b. However,
461 numerous large ApoJ⁺ granules were still present in the KO caput cells, and occasionally some
462 of them were arrested at the apical surface and labelled by ATP5 (Fig. 7h, purple arrows),
463 which structurally resembled the pm- Ω -DMV (Fig. 7h, insert). These results suggested that
464 Ocln can interact with ApoJ⁺ vesicles through ATP5b to undergo pharaphagy at TJ and
465 paracellular membranes.

466

467 To explore the role of Ocln-dependent ApoJ⁺-vesicles in phagolysosome maintenance,
468 we first immunostained HA-Ocln cryosection with the late endocytic marker Rab7 and
469 lysosome marker Lamp1 (Fig. 7i and i'). We observed HA-Ocln immunostaining in some of
470 these late endocytotic compartments, suggesting the participation of Ocln in the lysosomal
471 degradation pathway. We then immunostained the ApoJ⁺ vesicles of epididymal sections with
472 these late endocytotic markers. In WT caput principal cells (Fig. 7j) we observed that a few

473 ApoJ⁺ vesicles were surrounded by Rab7, but in *Ocln*-KO cells, Rab7 expression was
474 decreased, accompanying an increase in the number of intermediate-size vesicles containing
475 high intensity of ApoJ with weak Rab7 on their surface, as well as the accumulation of ApoJ
476 in the apical surface of principal cells and in the lumen. These results suggested that ApoJ is
477 accumulated in the late endocytotic compartment and at the apical membrane of these cells.
478 The Lamp1⁺ large vesicles (*i.e.* phagolysosomes) containing low levels of ApoJ were observed
479 in WT caput principal cells (Fig. 7j'), suggesting that endocytosed ApoJ is subjected to
480 degradation. However, in KO caput cells, phagolysosomes were absent but the smaller Lamp1⁺
481 lysosomes and the ApoJ⁺ endosomes were increased. These results suggest defects in fusion of
482 lysosomes and ApoJ⁺ phagosomes after KO of *Ocln*. We also labelled the ApoJ⁺ vesicles with
483 early endosome Eea1 and we observed that some co-localisation of ApoJ⁺ and Eea1 in small
484 vesicles as well as in the late endosomes in the apical domain (Fig. 7j'' and S21). We attribute
485 this to the clathrin-dependent CEM pathway. Overall, we conclude that ApoJ endocytosis in
486 WT caput principal cells can be mediated by heterogeneous pathways, involving the
487 conventional CME pathway via early endosomes as well as the *Ocln*-dependent paraphagy
488 pathway via an unknown mechanism. In *Ocln*-KO caput principal cells, the CME pathway was
489 upregulated and the late endocytic vacuoles were accumulated when paraphagy pathway was
490 impaired. In addition, our results suggested that the *Ocln* is required for the fusion of
491 paraphagosomes and lysosomes to form phagolysosomes for the degradation of vesicles
492 containing ApoJ⁺ cargo in the epididymis.

493

494 Our results have already indicated that the long TMDs of *Ocln* plays a crucial role in
495 membrane thickness and dynamics, and we propose that the unique lengths of *Ocln* TMDs
496 plays an indispensable role to match mixed thickness membranes for the fusion of
497 heterogeneous vesicles, and this function is lost after *Ocln* ablation. To test whether the long

498 TMD-associated function in *Ocln*-KO could be rescued, we constructed a plasmid
499 (*Cldn3/Ocln*-TM-GFP) by replacing the four shorter transmembrane domains of *Cldn-3* with
500 the longer TMDs of *Ocln* (*i.e.* 23-25 amino acids). We chose *Cldn-3* because it is in close
501 proximity to *Ocln* at TJs but has shorter length TMDs (*i.e.* 21 amino acids), and because it
502 shares a similar protein structural topology to the TMDs of *Ocln*⁵⁸. We used the plasmids of
503 WT GFP-*Ocln* and WT GFP-*Cldn-3* and transfected into *Ocln*-KO DC2 cells as controls. We
504 then immunostained the transfected cells and the anti-ApoJ immunofluorescent intensity in
505 intracellular granular structures were measured on those cells, except KO cells, with mature
506 paracellular membranes by showing continuous GFP strands (Fig. 7k). The results showed that
507 over-expression of truncated *Ocln*-KO plasmid into KO cells caused an increase in ApoJ⁺
508 granules with higher intensity than in *Ocln*-WT transfected cells. WT *Cldn-3*-transfected cells
509 showed only slight effect whereas the TM-replaced *Cldn-3*-transfected cells rescued the effect
510 on ApoJ⁺ granule populations towards the phenotypes of WT transfected cells. These findings
511 showed that ApoJ⁺ vesicles require *Ocln* for proper degradation, and supported our hypothesis
512 that the long TMDs of *Ocln* play an essential role in vesicle fusion in the same scenario, *i.e.*
513 fusion of paraphagosomes and lysosomes to form phagolysosomes in the WT cells, whereas
514 such vesicle fusion is arrested and the late endocytotic vacuoles are accumulated in the KO
515 cells.

516

517

DISCUSSION

518 In the present study we found that double-membrane phagosomes can be derived from
519 epithelial TJs plasma membranes and that they sense and take up large lipophilic cargoes by
520 bulk endocytosis in a receptor-mediated manner. This previously unrecognised endocytotic
521 mechanism—paraphagy—serves specialised tasks for paracellular entry of lipophilic cargo,

522 e.g. lipoproteins and vesicular membranes and RBPs, into cells, while raft-rich plasma
523 membranes were retrieved and epithelial integrity was preserved. A schematic view of our
524 current model for OcIn-promoted TJ paraphagic endocytosis and membrane trafficking in
525 epithelium is illustrated in Fig. 8. Our study also provides evidence for the presence of
526 paraphagy in the TJs of several epithelial tissues, including proximal epididymis in the
527 reproductive system, collecting duct in the renal system, bronchi in the respiratory system and
528 endothelium in the vascular system, indicating that it is a widespread phenomenon that could
529 have general significance to epithelial biology with far-reaching implications for human health.
530

531 **Paraphagy is a non-canonical LAP and a luminal lipophilic signalling sensor**

532 In the proximal epididymis, we found that OcIn-facilitated paraphagy functions with LC3 to
533 engulf cell remnants by employing an unconventional LC3-associated phagocytosis LAP,
534 characterised by double-membrane vesicles at the TJ multicellular membranes and involving
535 the low-affinity receptor Fcgr2b rather than the classical Lrp1 or Lrp2 receptors to sense
536 luminal bulky lipophilic signals. Although co-localisation of OcIn with the autophagy protein
537 Beclin1 has been reported in intestines⁵⁶, our results show that paraphagy in the epididymis
538 mainly involves unconventional rather than conventional autophagy Atg and LAP proteins¹¹.
539 While paraphagy initiation and maturation mechanisms are still unclear, our study supports the
540 view that it begins with small DMVs that become larger vesicles after LC3 recruitment,
541 following separation from the membrane by an OcIn-dependent action. We cannot rule out the
542 possibility that paraphagy engulfs exosomes or membrane-bound vesicles to construct DMVs
543 directly; however, the Ω -curvature of internal hemi-vesicles in the pm- Ω -shaped DMVs
544 supports the first scenario.

545

546 **Ocln promotes paraphagy by facilitating raft-membrane retrieval and recycling**

547 Our study shows that membrane repolarisation favours the Ocln-dependent bulk-endocytosis,
548 *i.e.* paraphagic vesicle fission under physiological conditions. This implies that the protein
549 moieties and lipids in the pro-paraphagic inner membrane leaflets have a positively charged
550 tendency, holding them to the outer leaflet, from which a temporary release can be initiated by
551 an intracellular negative electrical environment by repolarisation, and which promotes the
552 inward membrane curvature for vesicle invagination, presumably involving rafted flotillin-
553 microdomains⁴⁹. Consistently, our results support the involvement of electrogenic transporters
554 such as the glutamate transporter Slc11a1⁵⁹ in Ocln-dependent conductance, implying that the
555 pH-sensitive local intracellular depolarisation might be involved that drives paraphagy to occur.

556

557 Failure of cholesterol retrieval from the plasma membrane directly results in disorders
558 of membrane composition and steroid hormone synthesis by the cells^{4,7}. Our results show that
559 Ocln is required on the TJs for maintenance of membrane thickness, the retrieval of cholesterol-
560 rich rafted membranes and for paraphagic events. These mechanisms might involve the
561 function of the long TMDs of Ocln to match the mixed membranes. Rafted microdomains are
562 thicker than non-rafted membranes, in addition, they are usually docked with GPI-linked
563 proteins and thus they can transport selected membranes and function as signalling platforms¹⁸.
564 The failure of matching and retrieval of cholesterol-rich rafted membranes in *Ocln* ablated
565 epithelial cells could be the origin of the subsequent metabolic-associated pathological
566 conditions in multiple organs, including the depletion of micromembranes necessary for
567 recycling to the plasma membrane, as well as impairment of phagolysosome maintenance and
568 the downstream diverse physiological and signalling functions downstream^{8,18,40,60,61}.

569

570 **Epithelial paraphagy is a lipid clearance promoter**

571 It is known that phagolysosome formation completes the degradation cycle and provides new
572 cellular materials for biosynthetic pathways. *Ocln*-promoted paraphagy, by involving *Fcgr2b*
573 but not classical lipoprotein receptors, to take up the lipoproteins ApoJ and ApoA1, which are
574 known to shuffle cholesterol-rich membranes shed from spermatozoa into the epididymal
575 lumen⁴⁰ and could be the materials for new PUFA membranes and steroids hormone
576 synthesis^{19,23-27}. The high binding affinity of *Ocln* to ATP5b and the localization of ATP5b
577 around mitochondria are consistent with the notion that *Ocln* facilitates the transport of
578 lipoproteins to mitochondria for lipid metabolism^{62,63}. Although the paraphagy-promoted
579 cholesterol clearance mechanism remains unclear, we speculate that it involves reverse
580 cholesterol transport and that is mediated by ApoA1, because it has a high cholesterol
581 sequestering ability⁶⁴, and because the presence of cholesterol efflux transporters on the lateral
582 membrane of epididymal epithelial cells. In addition, flotillin was accumulated in these
583 paracellular membranes and the expression of cholesterol efflux transporters was
584 downregulated in *Ocln*-KO mice.

585

586 **Paraphagy prevents ectopic lipoprotein deposition and associated with complex multi-**
587 **organ metabolic disorder**

588 Our findings shows that the *Vkorc1* is downregulated after *Ocln*-KO. We propose that the
589 *Vkorc1* downregulation is due to impaired new membrane biogenesis for *Vkorc1* and other
590 membrane proteins with long TMDs. Alternatively, the downregulation of *Vkorc1* might be
591 due to insufficient uptake of transcription factors, such as exosomes for epigenetic
592 regulation^{65,66}. Consistently, numerous transcription-regulating proteins have been found in the
593 *Ocln*-interacting proteomes.

594

595 Our previous study showed that MGP can bind to phospholipids and lipophilic proteins
596 in a calcium-dependent manner and plays an important role in maintaining low calcium in the
597 epididymal fluids⁴². We propose that this mechanism is associated with the calcification
598 phenomenon in *Ocln*-KO mice³² and in neuronal malfunction patients with calcification and
599 *OCNL* mutation⁶⁷. We found that *Ocln* ablation results in *Vkorc1* downregulation and
600 carboxylation disorders, and subsequently ectopic deposition of ApoJ in downstream
601 compartments, such as distal epididymal lumen and renal medullar tubules. This pathological
602 condition might be the underlying cause of the complex phenotypes in multiple organs of *Ocln*-
603 KO mice and in patients, although the molecular and pathological mechanisms await
604 verification.

605

606 While we have focused on the cholesterol clearance and regulation of carboxylation-
607 dependent ectopic deposition in the male reproductive tract, we propose that epithelial
608 paraphagy at the TJs via unconventional LAP proteins is a novel mechanism of metabolic
609 homeostatic regulation in other epithelia. Some *OCNL* gene associated clinical human diseases
610 are related to the phenotypes observed in this study, such as brain calcification, gestational
611 diabetes mellitus and developmental delay and other pathogenic conditions⁶⁷⁻⁶⁹. These lines of
612 evidence suggest that the correlation of *OCNL* with pathological conditions associated with
613 male infertility and metabolic diseases are worthwhile exploring for the potential therapeutic
614 and diagnostic development.

615

616 **Summary**

617 Our study shows that paraghagy at the TJ membranes of principal cells senses the luminal
618 lipophilic signals in the proximal compartment of epithelia and modulates the function of
619 epithelia via crosstalk across distinct compartments. In the male reproductive tract of *Ocln*-KO
620 mice, the arrested paraghagy and impaired phagolysosome function in the proximal epithelial
621 cells result in the subsequent cholesterol overload and ectopic lipoprotein deposition in distal
622 compartments, due to the dysregulated metabolism-promoted processes, including VK-cycle
623 dependent carboxylation. Epithelial paraghagy provides a new framework for future studies
624 aimed at unravelling the cellular mechanisms of sensing luminal lipophilic signals and
625 modulation of epithelial functions, including cholesterol homeostatic regulation as well as
626 lipoprotein transepithelial transport and metabolism.

627

628

629

ACKNOWLEDGEMENTS

630 We thank Dr. Sylvie Breton at MGH Harvard Medical School for providing the *Ocln*-KO mice
631 and V-ATPase antibody used in this study. We also thank all the staff of ShanghaiTech core
632 facilities, particularly Drs. Xiao Ming Li, Pi Liang Hao and Yin Xiong for their technical
633 support. We thank Drs. Tian Chi, Trevor Cooper, Xing Xu Huang for comments on the
634 manuscript. This work is supported by grants to WWS from National Natural Science
635 Foundation of China (NNSFC: 31871166) and Shanghai Municipal Commission for Science
636 and Technology (SMCST: 17JC1420103; 19140903400), Center for Excellence in Molecular
637 Cell Science (CAS) and ShanghaiTech University. The HA-*Ocln* mice was generated by
638 Genome Tagging Project (GTP) Center, CEMCS, CAS (SMCST: 19411951800).

639

640

REFERENCE

641 1 Fung, K. Y. Y., Fairn, G. D. & Lee, W. L. Transcellular vesicular transport in
642 epithelial and endothelial cells: Challenges and opportunities. *Traffic* **19**, 5-18,
643 doi:10.1111/tra.12533 (2018).

644 2 Tuma, P. & Hubbard, A. L. Transcytosis: crossing cellular barriers. *Physiol Rev* **83**,
645 871-932, doi:10.1152/physrev.00001.2003 (2003).

646 3 Garcia-Castillo, M. D., Chinnapen, D. J. & Lencer, W. I. Membrane Transport across
647 Polarized Epithelia. *Cold Spring Harb Perspect Biol* **9**,
648 doi:10.1101/cshperspect.a027912 (2017).

649 4 Saheki, Y. & De Camilli, P. Synaptic vesicle endocytosis. *Cold Spring Harb Perspect*
650 *Biol* **4**, a005645, doi:10.1101/cshperspect.a005645 (2012).

651 5 Wu, L. G., Hamid, E., Shin, W. & Chiang, H. C. Exocytosis and Endocytosis: Modes,
652 Functions, and Coupling Mechanisms. *Annu Rev Physiol* **76**, 301-331,
653 doi:10.1146/annurev-physiol-021113-170305 (2014).

654 6 De Camilli, P. & Takei, K. Molecular mechanisms in synaptic vesicle endocytosis
655 and recycling. *Neuron* **16**, 481-486, doi:10.1016/s0896-6273(00)80068-9 (1996).

656 7 Doherty, G. J. & McMahon, H. T. Mechanisms of endocytosis. *Annu Rev Biochem*
657 **78**, 857-902, doi:10.1146/annurev.biochem.78.081307.110540 (2009).

658 8 Flannagan, R. S., Jaumouille, V. & Grinstein, S. The cell biology of phagocytosis.
659 *Annu Rev Pathol* **7**, 61-98, doi:10.1146/annurev-pathol-011811-132445 (2012).

660 9 El-Sayed, A. & Harashima, H. Endocytosis of gene delivery vectors: from clathrin-
661 dependent to lipid raft-mediated endocytosis. *Mol Ther* **21**, 1118-1130,
662 doi:10.1038/mt.2013.54 (2013).

663 10 Mayor, S., Parton, R. G. & Donaldson, J. G. Clathrin-independent pathways of
664 endocytosis. *Cold Spring Harb Perspect Biol* **6**, doi:10.1101/cshperspect.a016758
665 (2014).

666 11 Heckmann, B. L. & Green, D. R. LC3-associated phagocytosis at a glance (vol 132,
667 jcs222984, 2019). *J Cell Sci* **132** (2019).

668 12 Sanjuan, M. A. *et al.* Toll-like receptor signalling in macrophages links the autophagy
669 pathway to phagocytosis. *Nature* **450**, 1253-1257, doi:10.1038/nature06421 (2007).

670 13 Heckmann, B. L. *et al.* LC3-Associated Endocytosis Facilitates beta-Amyloid
671 Clearance and Mitigates Neurodegeneration in Murine Alzheimer's Disease. *Cell* **178**,
672 536-551 e514, doi:10.1016/j.cell.2019.05.056 (2019).

673 14 Martinez, J. *et al.* Microtubule-associated protein 1 light chain 3 alpha (LC3)-
674 associated phagocytosis is required for the efficient clearance of dead cells.
675 *Proceedings of the National Academy of Sciences of the United States of America*
676 **108**, 17396-17401, doi:10.1073/pnas.1113421108 (2011).

677 15 Martinez, J. *et al.* Molecular characterization of LC3-associated phagocytosis reveals
678 distinct roles for Rubicon, NOX2 and autophagy proteins. *Nat Cell Biol* **17**, 893-906,
679 doi:10.1038/ncb3192 (2015).

680 16 Heckmann, B. L., Boada-Romero, E., Cunha, L. D., Magne, J. & Green, D. R. LC3-
681 Associated Phagocytosis and Inflammation. *J Mol Biol* **429**, 3561-3576,
682 doi:10.1016/j.jmb.2017.08.012 (2017).

683 17 Cunha, L. D. *et al.* LC3-Associated Phagocytosis in Myeloid Cells Promotes Tumor
684 Immune Tolerance. *Cell* **175**, 429-441 e416, doi:10.1016/j.cell.2018.08.061 (2018).

685 18 Simons, K. & Sampaio, J. L. Membrane organization and lipid rafts. *Cold Spring*
686 *Harb Perspect Biol* **3**, a004697, doi:10.1101/cshperspect.a004697 (2011).

687 19 Luo, J., Yang, H. & Song, B. L. Mechanisms and regulation of cholesterol
688 homeostasis. *Nat Rev Mol Cell Biol* **21**, 225-245, doi:10.1038/s41580-019-0190-7
689 (2020).

690 20 Huang, L. H., Elvington, A. & Randolph, G. J. The role of the lymphatic system in
691 cholesterol transport. *Front Pharmacol* **6**, 182, doi:10.3389/fphar.2015.00182 (2015).

692 21 Cantuti-Castelvetri, L. *et al.* Defective cholesterol clearance limits remyelination in
693 the aged central nervous system. *Science* **359**, 684-688, doi:10.1126/science.aan4183
694 (2018).

695 22 Kwan, B. C., Kronenberg, F., Beddhu, S. & Cheung, A. K. Lipoprotein metabolism
696 and lipid management in chronic kidney disease. *J Am Soc Nephrol* **18**, 1246-1261,
697 doi:10.1681/ASN.2006091006 (2007).

698 23 Robaire, B. & Hinton, B. T. in *Knobil and Neill's Physiology of Reproduction* (eds
699 T.M. Plant & A.J. Zeleznik) 691-771 (Academic Press, Elsevier Inc. , 2015).

700 24 Gervasi, M. G. & Visconti, P. E. Molecular changes and signaling events occurring in
701 spermatozoa during epididymal maturation. *Andrology* **5**, 204-218,
702 doi:10.1111/andr.12320 (2017).

703 25 Haidl, G. & Opper, C. Changes in lipids and membrane anisotropy in human
704 spermatozoa during epididymal maturation. *Hum Reprod* **12**, 2720-2723,
705 doi:10.1093/humrep/12.12.2720 (1997).

706 26 Saez, F. & Drevet, J. R. Dietary Cholesterol and Lipid Overload: Impact on Male
707 Fertility. *Oxid Med Cell Longev* **2019**, 4521786, doi:10.1155/2019/4521786 (2019).

708 27 Saez, F., Ouvrier, A. & Drevet, J. R. Epididymis cholesterol homeostasis and sperm
709 fertilizing ability. *Asian J Androl* **13**, 11-17, doi:10.1038/aja.2010.64 (2011).

710 28 Bjorkgren, I. *et al.* Imbalanced lipid homeostasis in the conditional Dicer1 knockout
711 mouse epididymis causes instability of the sperm membrane. *Faseb J* **29**, 433-442,
712 doi:10.1096/fj.14-259382 (2015).

713 29 Ouvrier, A. *et al.* LXR and ABCA1 control cholesterol homeostasis in the proximal
714 mouse epididymis in a cell-specific manner. *J Lipid Res* **50**, 1766-1775,
715 doi:10.1194/jlr.M800657-JLR200 (2009).

716 30 Maqdasy, S. *et al.* Cholesterol and male fertility: what about orphans and adopted?
717 *Mol Cell Endocrinol* **368**, 30-46, doi:10.1016/j.mce.2012.06.011 (2013).

718 31 Kasturi, S. S., Tannir, J. & Brannigan, R. E. The metabolic syndrome and male
719 infertility. *J Androl* **29**, 251-259, doi:10.2164/jandrol.107.003731 (2008).

720 32 Saitou, M. *et al.* Complex phenotype of mice lacking occludin, a component of tight
721 junction strands. *Mol Biol Cell* **11**, 4131-4142 (2000).

722 33 Noda, N. N. & Inagaki, F. Mechanisms of Autophagy. *Annu Rev Biophys* **44**, 101-
723 122, doi:10.1146/annurev-biophys-060414-034248 (2015).

724 34 Choi, A. M., Ryter, S. W. & Levine, B. Autophagy in human health and disease. *The*
725 *New England journal of medicine* **368**, 1845-1846, doi:10.1056/NEJMc1303158
726 (2013).

727 35 Shum, W. W. *et al.* Transepithelial projections from basal cells are luminal sensors in
728 pseudostratified epithelia. *Cell* **135**, 1108-1117, doi:10.1016/j.cell.2008.10.020
729 (2008).

730 36 Karasov, W. H. Integrative physiology of transcellular and paracellular intestinal
731 absorption. *J Exp Biol* **220**, 2495-2501, doi:10.1242/jeb.144048 (2017).

732 37 Schuetz, A., Radusheva, V., Krug, S. M. & Heinemann, U. Crystal structure of the
733 tricellulin C-terminal coiled-coil domain reveals a unique mode of dimerization. *Ann*
734 *N Y Acad Sci* **1405**, 147-159, doi:10.1111/nyas.13408 (2017).

735 38 Morita, K., Furuse, M., Fujimoto, K. & Tsukita, S. Claudin multigene family
736 encoding four-transmembrane domain protein components of tight junction strands.
737 *Proceedings of the National Academy of Sciences of the United States of America* **96**,
738 511-516, doi:10.1073/pnas.96.2.511 (1999).

739 39 Saewu, A. *et al.* Clusterin in the mouse epididymis: possible roles in sperm
740 maturation and capacitation. *Reproduction* **154**, 867-880, doi:10.1530/REP-17-0518
741 (2017).

742 40 Griffiths, G. S., Galileo, D. S., Aravindan, R. G. & Martin-DeLeon, P. A. Clusterin
743 Facilitates Exchange of Glycosyl Phosphatidylinositol-Linked SPAM1 Between
744 Reproductive Luminal Fluids and Mouse and Human Sperm Membranes. *Biology of*
745 *Reproduction* **81**, 562-570, doi:10.1095/biolreprod.108.075739 (2009).

746 41 Schurgers, L. J., Uitto, J. & Reutelingsperger, C. P. Vitamin K-dependent
747 carboxylation of matrix Gla-protein: a crucial switch to control ectopic
748 mineralization. *Trends Mol Med* **19**, 217-226, doi:10.1016/j.molmed.2012.12.008
749 (2013).

750 42 Ma, H. *et al.* Vitamin K2-Dependent GGCX and MGP Are Required for Homeostatic
751 Calcium Regulation of Sperm Maturation. *iScience* **14**, 210-225,
752 doi:10.1016/j.isci.2019.03.030 (2019).

753 43 Rishavy, M. A. *et al.* Warfarin alters vitamin K metabolism: a surprising mechanism
754 of VKORC1 uncoupling necessitates an additional reductase. *Blood* **131**, 2826-2835,
755 doi:10.1182/blood-2017-09-804666 (2018).

756 44 Chinnapen, D. J. *et al.* Lipid sorting by ceramide structure from plasma membrane to
757 ER for the cholera toxin receptor ganglioside GM1. *Dev Cell* **23**, 573-586,
758 doi:10.1016/j.devcel.2012.08.002 (2012).

759 45 Zhao, W. D. *et al.* Hemi-fused structure mediates and controls fusion and fission in
760 live cells. *Nature* **534**, 548-552, doi:10.1038/nature18598 (2016).

761 46 Solsona, C., Innocenti, B. & Fernandez, J. M. Regulation of exocytotic fusion by cell
762 inflation. *Biophys J* **74**, 1061-1073, doi:10.1016/S0006-3495(98)74030-5 (1998).

763 47 Henkel, A. W. & Almers, W. Fast steps in exocytosis and endocytosis studied by
764 capacitance measurements in endocrine cells. *Curr Opin Neurobiol* **6**, 350-357,
765 doi:10.1016/s0959-4388(96)80119-x (1996).

766 48 Glebov, O. O., Bright, N. A. & Nichols, B. J. Flotillin-1 defines a clathrin-
767 independent endocytic pathway in mammalian cells. *Nat Cell Biol* **8**, 46-54,
768 doi:10.1038/ncb1342 (2006).

769 49 Otto, G. P. & Nichols, B. J. The roles of flotillin microdomains--endocytosis and
770 beyond. *J Cell Sci* **124**, 3933-3940, doi:10.1242/jcs.092015 (2011).

771 50 Nakayama, K. *et al.* RNG105/caprin1, an RNA granule protein for dendritic mRNA
772 localization, is essential for long-term memory formation. *Elife* **6**,
773 doi:10.7554/eLife.29677 (2017).

774 51 Liao, Y. C. *et al.* RNA Granules Hitchhike on Lysosomes for Long-Distance
775 Transport, Using Annexin A11 as a Molecular Tether. *Cell* **179**, 147-+,
776 doi:10.1016/j.cell.2019.08.050 (2019).

777 52 Hurtado-Lorenzo, A. *et al.* V-ATPase interacts with ARNO and Arf6 in early
778 endosomes and regulates the protein degradative pathway. *Nat Cell Biol* **8**, 124-136,
779 doi:10.1038/ncb1348 (2006).

780 53 Breton, S. & Brown, D. Regulation of luminal acidification by the V-ATPase.
781 *Physiology (Bethesda)* **28**, 318-329, doi:10.1152/physiol.00007.2013 (2013).

782 54 Jager, S. *et al.* Role for Rab7 in maturation of late autophagic vacuoles. *J Cell Sci*
783 **117**, 4837-4848, doi:10.1242/jcs.01370 (2004).

784 55 Kuchitsu, Y. & Fukuda, M. Revisiting Rab7 Functions in Mammalian Autophagy:
785 Rab7 Knockout Studies. *Cells* **7**, doi:10.3390/cells7110215 (2018).

786 56 Wong, M. *et al.* Intestinal epithelial tight junction barrier regulation by autophagy-
787 related protein ATG6/beclin 1. *Am J Physiol Cell Physiol* **316**, C753-C765,
788 doi:10.1152/ajpcell.00246.2018 (2019).

- 789 57 Martinez, L. O. *et al.* Ectopic beta-chain of ATP synthase is an apolipoprotein A-I
790 receptor in hepatic HDL endocytosis. *Nature* **421**, 75-79, doi:10.1038/nature01250
791 (2003).
- 792 58 Tsukita, S. & Furuse, M. Occludin and claudins in tight-junction strands: leading or
793 supporting players? *Trends Cell Biol* **9**, 268-273, doi:10.1016/s0962-8924(99)01578-
794 0 (1999).
- 795 59 Magi, S., Piccirillo, S., Amoroso, S. & Lariccia, V. Excitatory Amino Acid
796 Transporters (EAATs): Glutamate Transport and Beyond. *Int J Mol Sci* **20**,
797 doi:10.3390/ijms20225674 (2019).
- 798 60 Klionsky, D. J. *et al.* Guidelines for the use and interpretation of assays for
799 monitoring autophagy. *Autophagy* **8**, 445-544, doi:10.4161/auto.19496 (2012).
- 800 61 Zhou, T. *et al.* Occludin protects secretory cells from ER stress by facilitating
801 SNARE-dependent apical protein exocytosis. *Proceedings of the National Academy*
802 *of Sciences of the United States of America* **117**, 4758-4769,
803 doi:10.1073/pnas.1909731117 (2020).
- 804 62 Deng, J. *et al.* FUS interacts with ATP synthase beta subunit and induces
805 mitochondrial unfolded protein response in cellular and animal models. *Proceedings*
806 *of the National Academy of Sciences of the United States of America* **115**, E9678-
807 E9686, doi:10.1073/pnas.1806655115 (2018).
- 808 63 Benador, I. Y., Veliova, M., Liesa, M. & Shirihai, O. S. Mitochondria Bound to Lipid
809 Droplets: Where Mitochondrial Dynamics Regulate Lipid Storage and Utilization.
810 *Cell Metab* **29**, 827-835, doi:10.1016/j.cmet.2019.02.011 (2019).
- 811 64 Zhao, Y., Van Berkel, T. J. & Van Eck, M. Relative roles of various efflux pathways
812 in net cholesterol efflux from macrophage foam cells in atherosclerotic lesions. *Curr*
813 *Opin Lipidol* **21**, 441-453, doi:10.1097/MOL.0b013e32833dedaa (2010).
- 814 65 Chen, Q. *et al.* Sperm tsRNAs contribute to intergenerational inheritance of an
815 acquired metabolic disorder. *Science* **351**, 397-400, doi:10.1126/science.aad7977
816 (2016).
- 817 66 Sharma, U. *et al.* Biogenesis and function of tRNA fragments during sperm
818 maturation and fertilization in mammals. *Science* **351**, 391-396,
819 doi:10.1126/science.aad6780 (2016).
- 820 67 O'Driscoll, M. C. *et al.* Recessive mutations in the gene encoding the tight junction
821 protein occludin cause band-like calcification with simplified gyration and
822 polymicrogyria. *Am J Hum Genet* **87**, 354-364, doi:10.1016/j.ajhg.2010.07.012
823 (2010).
- 824 68 Alazami, A. M. *et al.* Accelerating novel candidate gene discovery in neurogenetic
825 disorders via whole-exome sequencing of prescreened multiplex consanguineous
826 families. *Cell Rep* **10**, 148-161, doi:10.1016/j.celrep.2014.12.015 (2015).
- 827 69 Kasak, L., Rull, K., Vaas, P., Teesalu, P. & Laan, M. Extensive load of somatic CNVs
828 in the human placenta. *Sci Rep* **5**, 8342, doi:10.1038/srep08342 (2015).

829
830
831

FIGURE LEGENDS

832 **Figure 1**

833 ***Ocln*-KO have arrested paracellular heterophagy in *Ocln*-enriched plasma membrane**
834 **and degenerated phagolysosome in epididymal epithelial cells**

835 **a.** Typical HPF-TEM images showing the intracellular organelles in apical paracellular
836 domains of caput epididymidal principal cells of adult mice. White arrows: hemi-fused
837 Ω -shaped double-membrane vesicles beneath the proximal TJ paracellular membrane
838 (pm- Ω -DMVs). Double-arrow: a DMV containing TJ-like texture in the vesicle lumen
839 with its outer membrane still partially linked to the TJ components. Asterisks:
840 phagolysosomes. Scale bars: 0.2 – 1 μ m. (**a'**) Quantification of different vesicles (>10
841 cells from 3 mice per group).

842 **b.** HPF-TEM images and (**b'**) quantification of the vesicles (white arrows) docked to
843 paracellular membrane in caput epididymidal cells. Black arrows: plasma membrane-
844 associated vacuolar vesicles.

845 **c.** Double-immunolabeled for ZO1 and Cldn-3 of proximal caput (pCPT) of *Ocln*^{+/+} and
846 *Ocln*^{-/-} mice. Higher magnification images showing numerous vesicular structures of
847 heterogenous sizes in the TJs of WT epithelial cells but nearly absent in the same region
848 of KO epididymis.

849 **d.** Confocal projection images of immunolabelled mouse proximal caput epididymidis for
850 anti-HA-Ocln, ZO1 and B1-VATPase. Arrows: paraphagy-like structures near
851 tricellular corners. Double-arrow: paraphagy-like structures at paracellular TJs.
852 Arrowheads: weak paracellular level of HA-Ocln. Asterisk: a clear cell with negligible
853 level of HA-Ocln.

854 **e.** Kidney cortical collecting duct and (**f**) bronchial epithelium from HA-Ocln tag mice
855 stained for anti-HA antibody. (**e'** and **f'**) Higher magnification image showing the
856 paraphagy-like structures at paracellular TJs of renal principal cells (arrows) as well as
857 in endothelial capillary cells in choroid plexus (**g**). (**h** and **i**) Absence of dynamic
858 structures in the TJs stained for anti-HA-Ocln in epithelial cells of trachea and testis.
859 Red: ZO1 in h and i.

860 j. The presence of a vesicular-structure (arrows) derived from the anti-Ocln antibody
861 labelled TJs in human small intestine (H. Intestine).

862

863 **Figure 2**

864 **Ocln is essential to prevent cholesterol accumulation but not epithelial barrier integrity**

865 a. Typical HPF-TEM images showing paracellular junctional structures in caput epithelial
866 cells of adult *Ocln*^{+/+} and *Ocln*^{-/-} mice. TJ: arrows 1 to 2; ZA (zonula adhaerens): arrows
867 2 to 3; desmosome: double-arrow; adherens junctions: arrowheads. Junctional complex
868 (JC) composing TJ, ZA and desmosome occasionally present. Quantification of the
869 junctional structures (a'). ***P*<0.01 unpaired t-test (n=3 mice per group).

870 b. No detectable biotin immunofluorescent-staining in the lumen of epididymis of
871 perfused mice. Green: ZO-1.

872 c. TEM images of mouse caput epididymal cells perfused with paracellular tracer
873 lanthanum.

874 d. Electric cell-substrate impedance sensing (ECIS) measurement results showed no
875 difference in impedance and capacitance at higher frequencies nor resistance at low
876 frequencies, suggesting no difference in tight junction integrity, cell monolayer covered
877 surface area, as well as similar attachment and spreading of cellular behaviors in
878 *Ocln*^{+/+} and *Ocln*^{-/-} DC2 cells.

879 e. TEM images showing part of the paracellular plasma membrane (PM) in the caput
880 epididymal principal cells of mice. Quantification showing decreased membrane
881 thickness in *Ocln*^{-/-} vs WT cells.

882 f. Fluorescent images showing filipin-labelled (30min incubation) cholesterol in *Ocln*^{+/+}
883 and *Ocln*^{-/-} DC2 cells. Quantification of cholesterol levels in these cells.

884 g. Membrane fluidity of *Ocln*^{+/+} and *Ocln*^{-/-} DC2 cells.

- 885 **h.** Images showing accumulated lipophilic dye DiD-Cy5 after 22 h incubation with
886 *Ocln*^{+/+} and *Ocln*^{-/-} DC2 cells before fixation.
- 887 **i.** 3D-reconstruction of confocal stack images showing the features of paracellular
888 membranes in WT DC2 cells transfected with truncated KO Ocln-C-GFP or WT N-
889 GFP-Ocln, and *Ocln*-KO cells transfected with WT GFP-N-Ocln (**i'**).
- 890 **j.** Transepithelial transport assay of 3kDa dextran in *Ocln*^{+/+} and *Ocln*^{-/-} monolayer DC2
891 cells (n=9).
- 892 **k.** Filipin fluorescence profiles in the epididymal epithelial cells. (**k'**) Quantification of
893 filipin intensity in the luminal contents of different epididymal regions (n=3 mice per
894 group).
- 895 **l.** *Ocln*^{+/+} and *Ocln*^{-/-} spermatozoa (**l**), kidney tubules (**l'**) and liver (**l''**) labeled with
896 filipin.
- 897 Blue: DNA stained with DAPI. Scale bars: 10 μ m, unless specified.

898

899 **Figure 3**

900 **Ocln regulates phagosome-associated cholesterol transport and metabolic pathways**

- 901 **f.** Cytoscape plots of KEGG-based PathActNet analyses with shortlisted proteomic and
902 transcriptomic DEGs of caput-only and whole epididymis. Circle size: [-Log(*P*-value)],
903 border width: enrichment. Green: downregulated, red: upregulated, yellow: both down-
904 and up-regulated pathways.
- 905 (**b-f**) DEGs Expression profiles associated with cholesterol homeostatic pathways of
906 whole epididymis and caput epididymidis. (**b**) Cholesterol *de novo* synthesis, (**c**)
907 extracellular transport, (**d**) uptake, (**e**) intracellular trafficking, and (**f**) cholesterol efflux
908 and scavenging pathways. Data were means \pm SD (n=3 mice per group). **P*<0.05, **
909 *P*<0.01, *** *P*<0.001, unpaired student's *t*-test. Cross sign: undetectable level.

- 910 g. Venn graphs of categorized transcripts of the significant down- and up-regulated DEGs
911 datasets.
- 912 h. Graphic summary of a hypothetical model of Ocln-promoted paraphagy in cholesterol
913 transepithelial transport in epididymal epithelium.

914

915 **Figure 4**

916 **Ocln-mediated paraphagy confers protection from cholesterol accumulation and**
917 **lipophilic ectopic deposition, partly through vitamin-K dependent carboxylation**

- 918 a. Confocal projection images showing ApoJ subcellular localization in different regions
919 of *Ocln*^{+/+} and *Ocln*^{-/-} mouse epididymis. Quantification bar graph of luminal ApoJ
920 intensity (a') and scatter plot (a'') of ApoJ⁺ intensity in organelles of epithelial cells
921 measured on projected images with Volocity (n=3 mice per group).
- 922 b. Kidney cryosections immunostained for ApoJ showing its presence in principal cells of
923 cortical collecting duct of adult mice. V-ATPase: intercalated cells. G: glomerulus.
924 Arrows: renal cells with accumulated ApoJ. Insert: higher magnification of proximal
925 tubules.
- 926 c. No immunostaining signals for Lrp1 and Lrp2 in the apical surface (arrows) of caput
927 epithelial cells of adult mice.
- 928 d. The presence of numerous paraphagy-like structures (arrows) positive for Fcgr2b
929 (green) with ZO1 (red) at the TJs of WT caput epithelial cells and the contained co-
930 localization in the *Ocln*-KO caput cells. Doublearrows: scaffolding TJ membranes. (d')
931 Accumulated of Fcgr2b at the TJs in the *Ocln*^{-/-} caput cells compared to that of *Ocln*^{+/+}
932 mice. Yellow arrows indicate the position for the Fcgr2b immunofluorescent intensity
933 profiles as plotted in d''). Dispersed immunostained Fcgr2b intensity (arrows) beyond

- 934 the TJs structures (ZO1 in red) on the apex of *Ocln*^{+/+} caput cells versus the contained
935 Fcgr2b intensity within the TJs structures (asterisks) in *Ocln*^{-/-} caput cells.
- 936 e. Fcgr2b and GFP-N-Ocln co-localizations (arrow and arrowheads) in DC2 cells.
- 937 f. Fcgr2b and ApoJ co-localizations in the epididymal caput cells of adult WT mice.
- 938 g. Co-localizations (arrow and arrowheads) of MGP and GFP-N-Ocln in DC2 cells.
- 939 h. The presence of MGP within the ApoJ labelled cargo in epithelial cells of epididymis,
940 respiratory and kidney of *Ocln*^{+/+} and *Ocln*^{-/-} mice.
- 941 i. Double-immunostaining of Vkorc1 and Rab7 in proximal caput principal cells. Higher
942 magnification of 3D-orthogonal view showing colocalization of Vkorc1 and Rab7 in
943 *Ocln*^{+/+} but not in *Ocln*^{-/-} caput cells.
- 944 j. Increased immunofluorescence of total Gla-residues containing proteins in epididymal
945 epithelial cells (asterisks) of *Ocln*^{-/-} compared to *Ocln*^{+/+} mice.
- 946 k. Kidney cortical collecting duct (CCD) and proximal tubules (PTs).
947 *Lu*: Lumen. Scale bars: 10 μ m. Blue: DNA labelled with DAPI.

948

949 **Figure 5**

950 **Ocln facilitates rafted plasma membrane and flotillin-microdomains retrieval and**
951 **recycling via bulk-endocytosis**

- 952 a. Confocal images showing CTxB endocytosis assay on WT or *Ocln*-KO DC2 cells at
953 various time points and quantification of CTxB fluorescence signals using images of
954 same parameters.
- 955 b. Whole-cell patch-clamp measurement of passive membrane properties of WT and
956 *Ocln*-KO DC2 cells. (a) Whole-cell capacitance during repeatedly hyperpolarization
957 (C_{m-H}) and repolarization (C_{m-R}) and conductances (G_{m-H} and G_{m-R}). (b) Changes of
958 capacitance (ΔC_m) upon hyperpolarization of WT (n = 11) or *Ocln*-KO cells (n = 7). (c)

959 Digital subtracted capacitance ($\Delta C_{m\text{-subtraction}}$) of the repolarization-induced capacitance
960 from that of hypolarization-triggered response of the same cells. (d,e) Time constant of
961 the raised current upon repolarization and the pre-pulse resting conductance of the same
962 cells in *b* and *c*. Arrows: time lag before the sustained increment in membrane
963 capacitance of WT cells.

964 **c.** Increased of transporter Slc1a1 (arrows) in apical surface of dCPT principal cells of
965 *Ocln*^{-/-} compared to *Ocln*^{+/+} mice.

966 **d.** 3D-reconstruction images of immunostaining showing decreased flotillin in the
967 intracellular vesicles of principal cells of KO IS epididymidis.

968 **e.** Accumulated flotillin in the paracellular membranes of dCPT principal cells of *Ocln*-
969 KO compared to WT mice. (e') Intensity profile of flotillin along the yellow arrows as
970 in E.

971 **f.** Immunofluorescent staining for flotillin with *Ocln*-N-GFP transfected DC2 cells. Insert:
972 a nascent double-membrane-like vesicle budding from the paracellular membranes of
973 two adjacent cells.

974 **g.** Live-cell imaging showing endocytosis events at paracellular membranes of DC2 cells
975 expressing WT-*Ocln*-GFP and loaded with lysotracker.

976 *Lu*: Lumen. Scale bars: 10 μm . Blue: DNA labelled with DAPI.

977

978 **Figure 6**

979 ***Ocln*-promoted parapagy involves autophagy protein LC3 but not Beclin-1**

980 **a.** Venn graph of the autophagy DEGs and heatmap of significant changed DEGs in the
981 transcriptomic and proteomics of CPT epididymidis of *Ocln*^{+/+} vs *Ocln*^{-/-} mice.

982 **b.** 3D-reconstruction confocal images of LC3 and E-cadherin in the IS segment of WT
983 and KO mice showing the presence of vesicular-like structure at the apical domain of

- 984 one WT principal cells. Insert: a phagocytotic-like large vesicle labelled for LC3 near
985 the paracellular membranes (double-arrow).
- 986 **c.** Colocalization of LC3-RFP and Ocln-GFP in co-transfected DC2 cells.
- 987 **d.** Confocal projection and 3D-reconstruction images (inserts) showing the colocalization
988 of LC3 with ZO1 at the peri-TJ membranes in WT IS and pCPT epididymidis. Yellow
989 arrows indicate the position for the intensity profiles as plotted in E.
- 990 **e.** Asterisks: enriched LC3 levels in the ZO1-labeled paraphagic-like structures at TJs;
991 arrows: increased LC3 near ZO1-labelled TJs in WT cells.
- 992 **f.** Double-labelling of anti-LC3 and ApoJ in *Ocln*^{+/+} and *Ocln*^{-/-} pCPT epididymidis. The
993 LC3 on the ApoJ⁺ vacuoles is more frequent in WT (double-arrow) than in KO principal
994 cells. A line of ApoJ is visible in the apical surface of KO principal cells but not in that
995 of WT cells.
- 996 **g.** The presence of Beclin-1 labelling on the TJs (ZO1) of intestine epithelial cells, but not
997 in epididymal CPT epithelial cells.

998 Scale bars: 10 μ m. Blue: DNA labelled with DAPI.

999

1000 **Figure 7**

1001 **Ocln promotes the transport of ApoJ and ApoA1 to ATP5b in the caput epididymidis**

- 1002 **a.** Enrichment terms of IP-MS proteome from DC2 cells overexpressed Ocln-N-Flag
1003 plasmid. (A') Ocln-N-Flag protein co-IP with anti-flag antibody from overexpressed
1004 DC2 cells following immunoblotting for ATP5b.
- 1005 **b.** 3D-reconstruction image showing immunostaining of ATP5b with Ocln-N-GFP
1006 transfected DC2 cells.

- 1007 **c.** Confocal projection image and higher magnification of 3D-reconstruction images of
1008 ATP5b and HA-Ocln of mouse IS epididymidis. Arrows: co-localization of ATP5b and
1009 HA-Ocln at the TJ.
- 1010 **d.** Double-immunostaining for ApoA1 and ATP5b in CPT and CPS epididymidis of *Ocln*^{-/-}
1011 and *Ocln*^{+/+} males. Arrow: the ApoA1-labelled cellular debris-like remnants
1012 surrounding WT sperm acrosomes. Double-arrow: weak ApoA1 in stereocilia of KO
1013 principal cells.
- 1014 **e.** 3D-reconstruction images for ApoA1 and ATP5b in pCPT of *Ocln*^{-/-} and *Ocln*^{+/+} mice.
- 1015 **f.** 3D-reconstruction images for ApoA1 and HA-Ocln of CPT segments. Inserts: strong
1016 co-localization in cargoes. Asterisks: weak ApoA1 and HA-Ocln levels on the surface
1017 of basal cells. Double-arrows: dynamics vesicular events at the paracellular membranes
1018 of principal cells.
- 1019 **g.** Co-localization of ApoJ and HA-Ocln in pCPT (arrows) at the TJ with a vesicle in close
1020 proximity.
- 1021 **h.** Co-localization of ATP5b and ApoJ in pCPT of *Ocln*^{-/-} and *Ocln*^{+/+} mice in the small
1022 vesicular structures (arrows). Asterisk: a clear cell. Magenta arrows: pm-Ω-DMV-like
1023 ApoJ⁺ vesicle at the apical paracellular space of principal cells.
- 1024 **i.** Double-immunostaining of Rab7 and Lamp1 with anti-HA of pCPT epididymidis from
1025 HA-Ocln mice.
- 1026 **j.** Subcellular localization of Rab7, Lamp and Eea1 with ApoJ in pCPT epididymidis of
1027 *Ocln*^{+/+} and *Ocln*^{-/-} mice.
- 1028 **k.** Scatter plot of ApoJ immunofluorescence profiles in the organelles of *Ocln*-KO DC2
1029 cells transfected with the plasmid either of WT-Ocln-GFP, truncated Ocln-KO-GFP, or
1030 WT-Cldn3-GFP, or a rescue plasmid of Cldn3/Ocln-TM-GFP in which the four

1031 transmembrane domains of Cldn3 were replaced with those of Ocln. Data represent
1032 results of cell numbers as indicated.

1033 *Lu*: Lumen. Scale bars: 10 μ m. Blue: DNA labelled with DAPI.

1034

1035 **Figure 8**

1036 **Schematic representation of paraphagy the TJs and transepithelial cholesterol transport**

1037 **of epithelial cells.** Ocln in the epithelial cells of proximal compartment promotes paraphagy

1038 at TJs to take up lipophilic cargoes by involving surface membrane receptor Fcgr2b and

1039 intracellular HDL receptor ATP5b, subsequently facilitating raft-membrane retrieval and

1040 recycling. Paraphagosomes maintains phagolysosome function and redox-promoted VK-

1041 dependent MGP carboxylation, which in turn facilitates lipoprotein ApoJ uptake. Impaired

1042 paraphagy leads to cholesterol accumulation and ApoJ deposition in the distal compartment.

1043 For more details, see the main text.

1044

1045

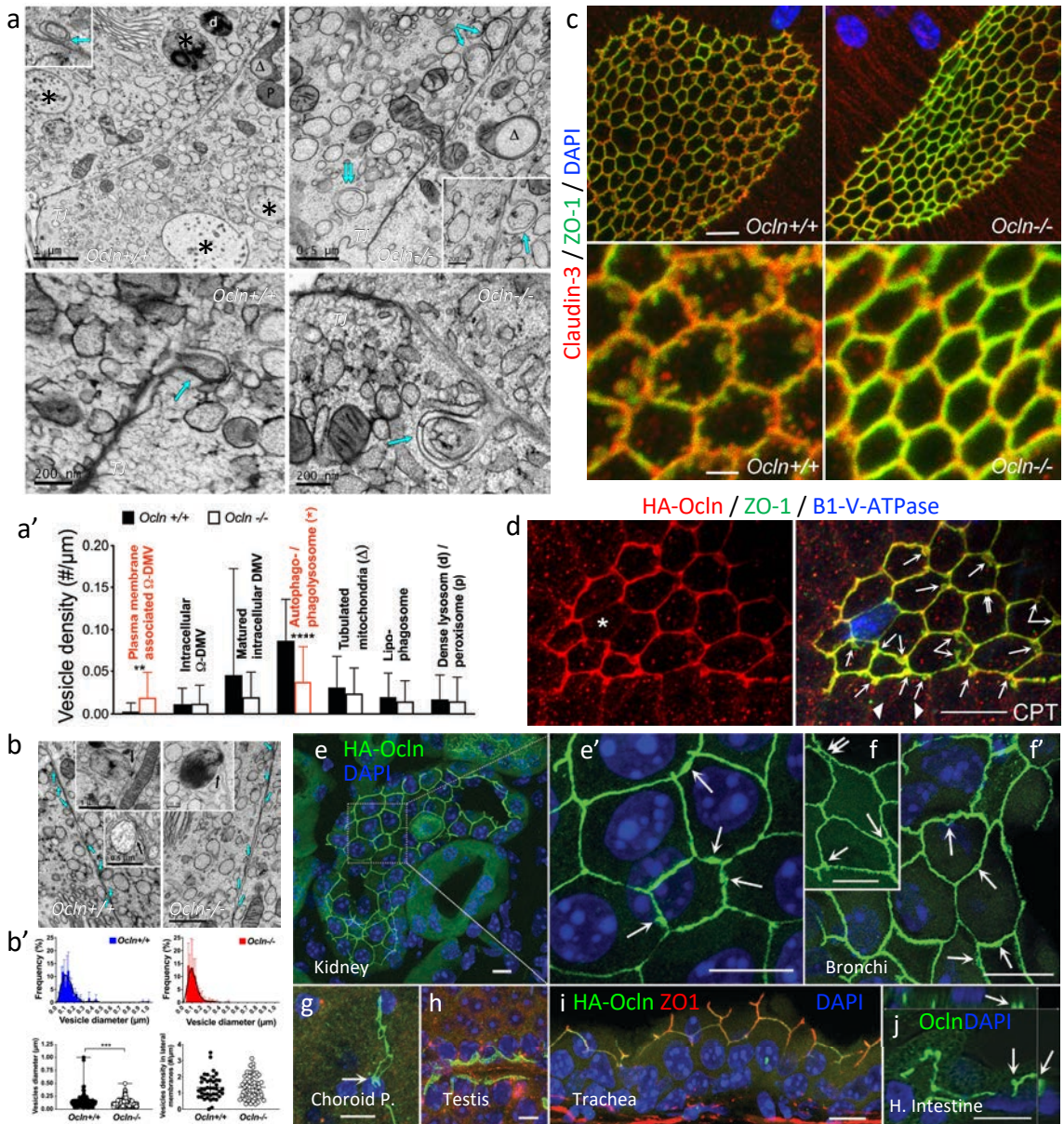


Fig. 1

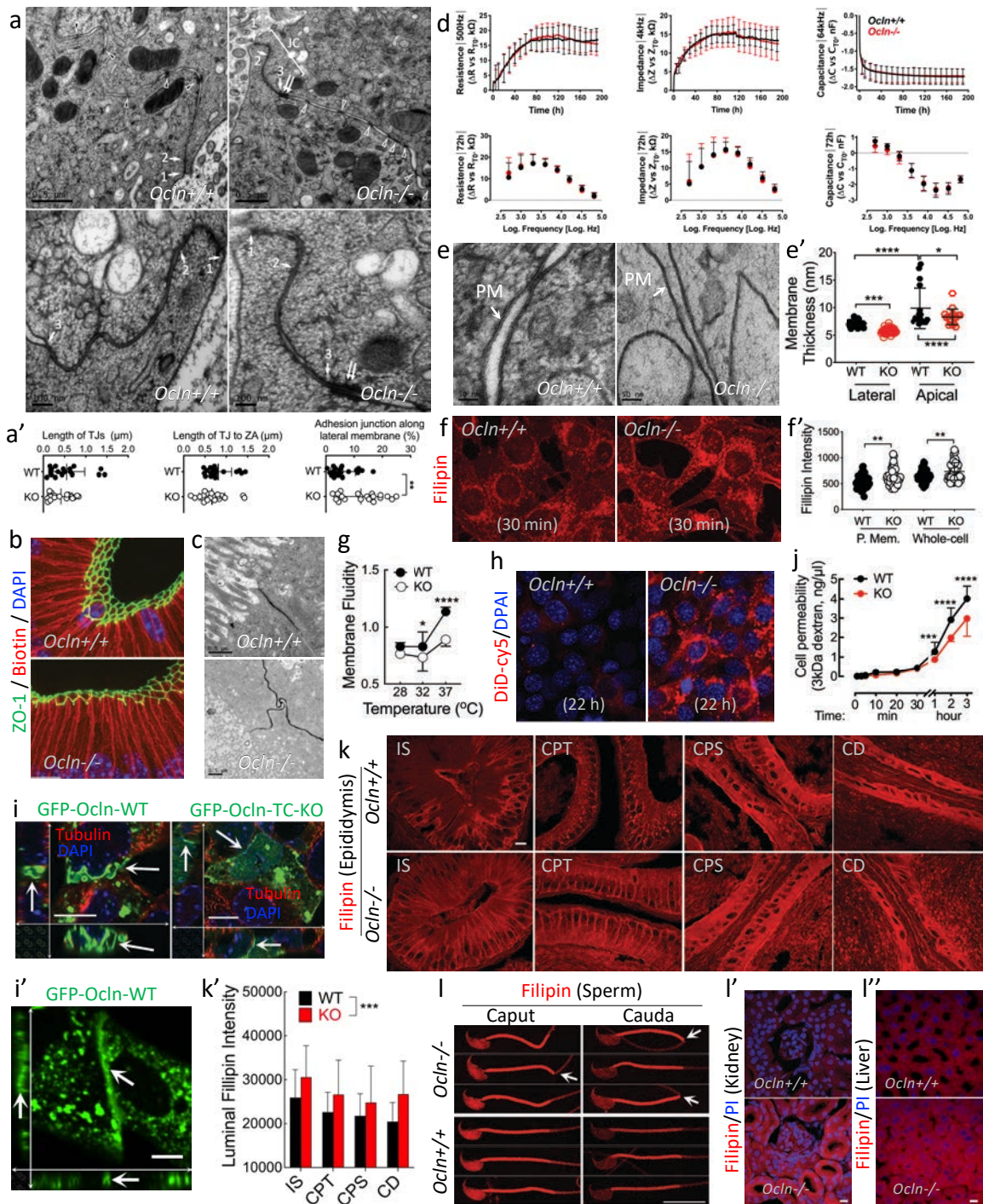
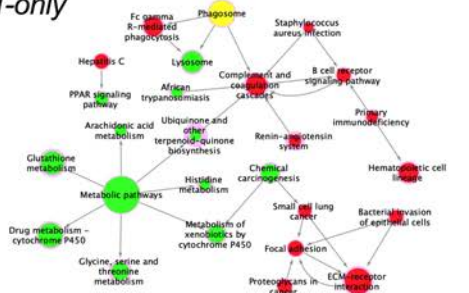
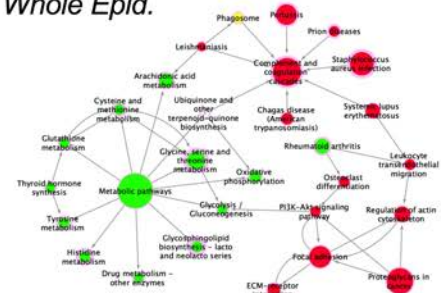


Fig. 2

a. CPT-only

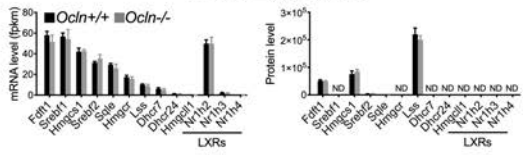


a'. Whole Epid.

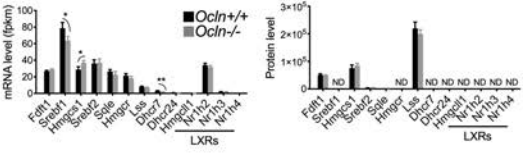


b. Cholesterol de novo synthesis & transcription

Whole Epididymis

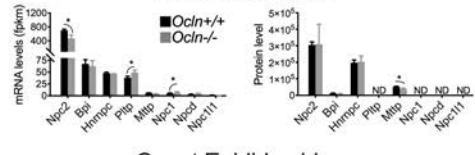


Caput Epididymidum

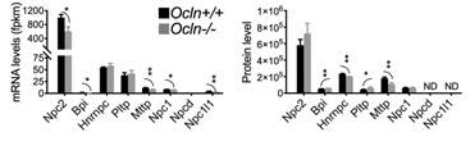


e. Cholesterol intracellular trafficking

Whole Epididymis

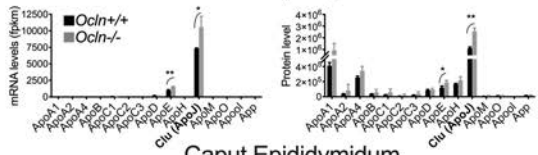


Caput Epididymidum

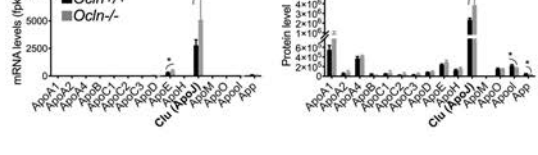


c. Cholesterol/lipid transport

Whole Epididymis

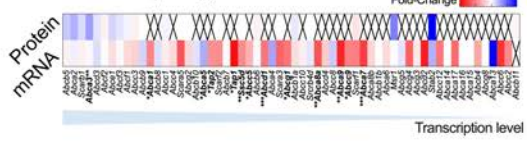


Caput Epididymidum

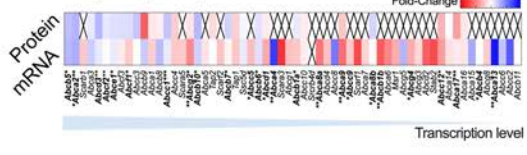


f. Cholesterol efflux & scavenging

Whole Epididymis

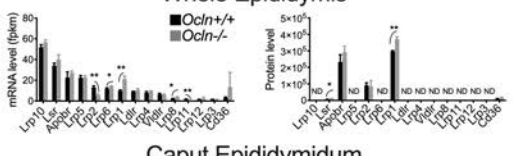


Caput Epididymidum

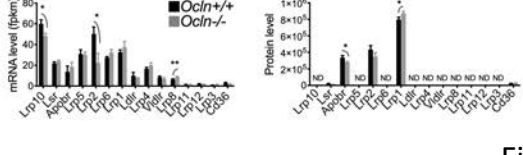


d. Cholesterol/lipid uptake

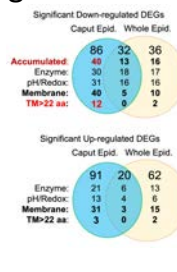
Whole Epididymis



Caput Epididymidum



g.



h.

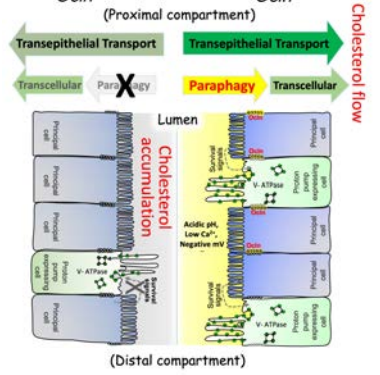


Fig. 3

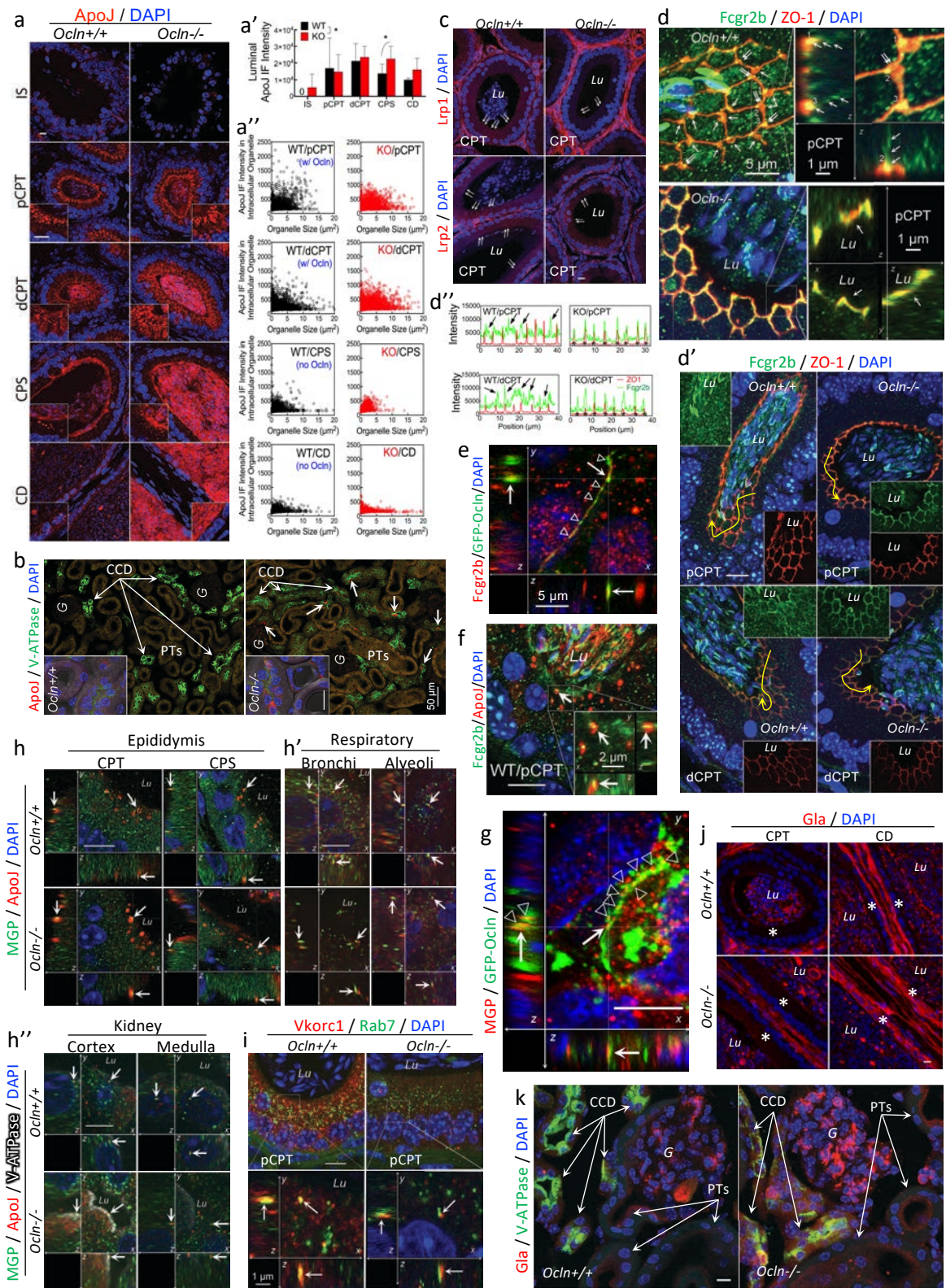


Fig. 4

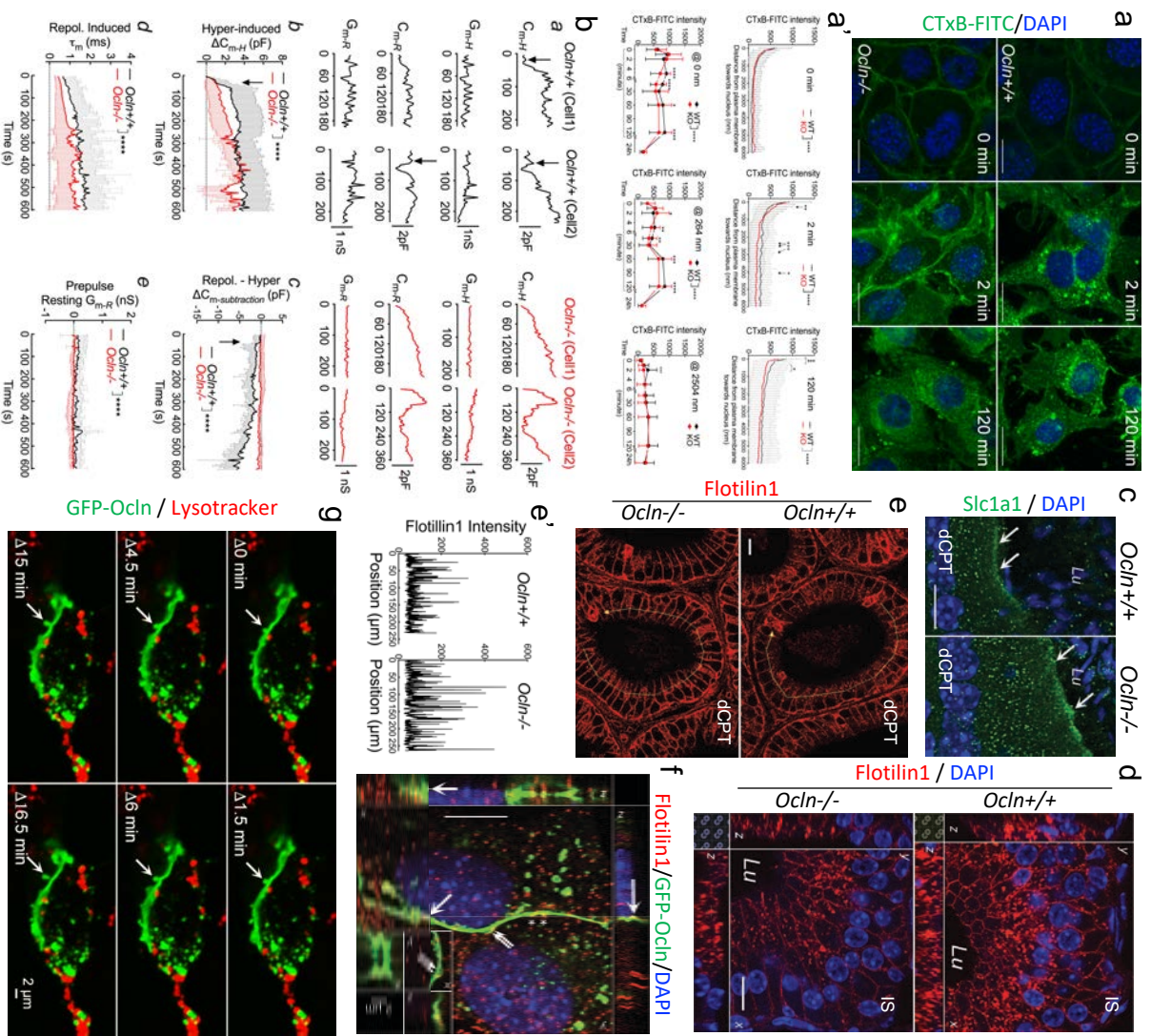


Fig. 5

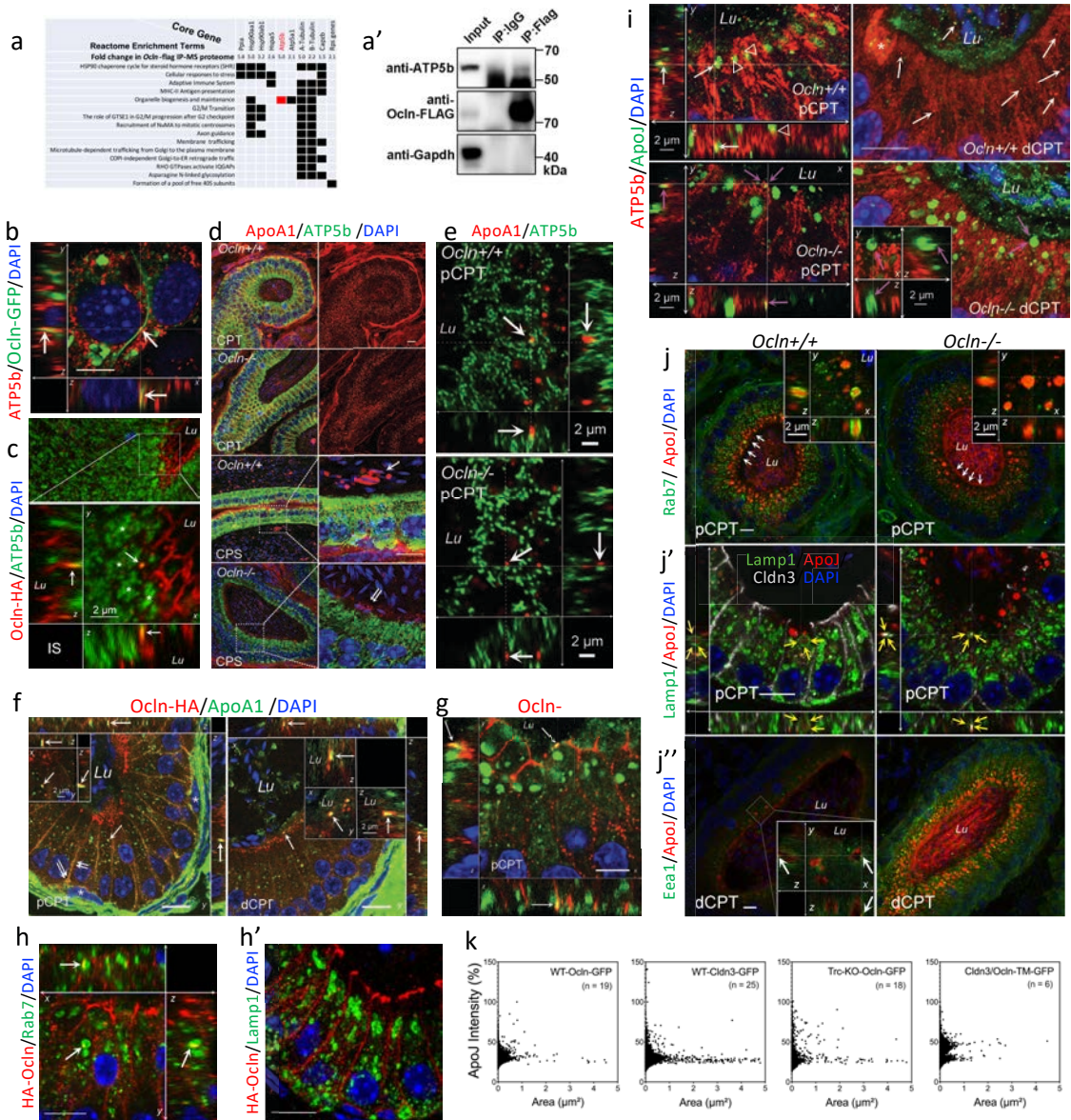


Fig. 7

Epithelial parapahgy

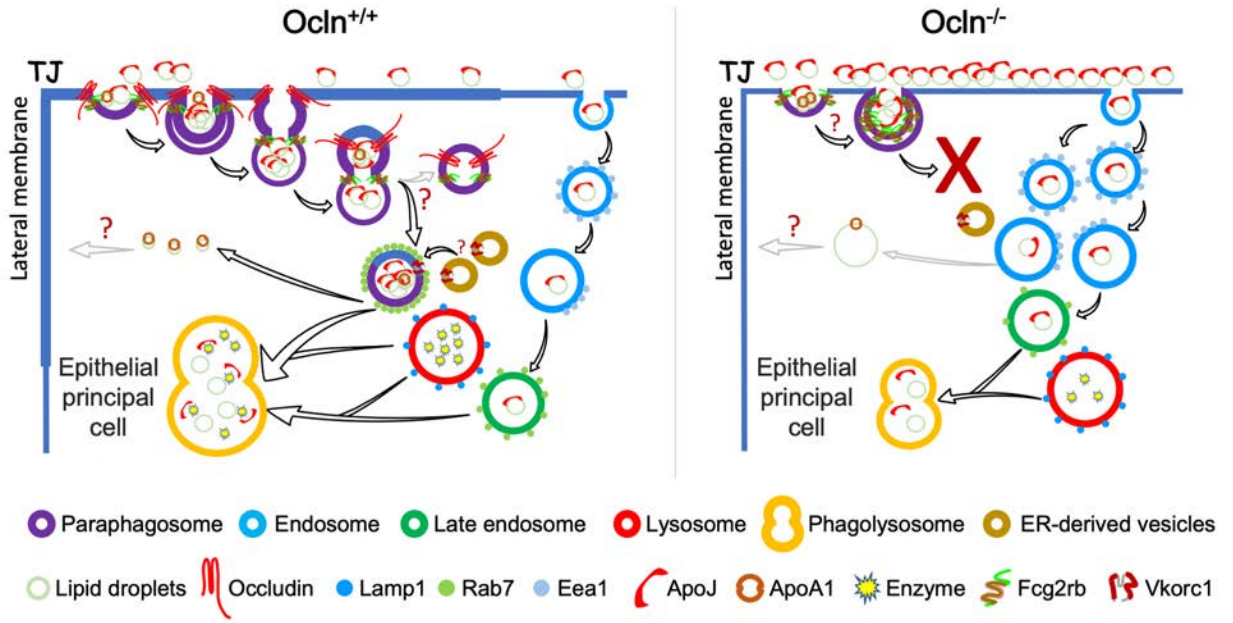


Fig. 8

Supplementary Fig. S1 (related to Fig. 1):

Expression pattern of *Ocln*^{+/+} mRNA in different epithelial tissues of male WT and *Ocln*-KO mice. Insert: mRNA levels in different postnatal age of male WT and *Ocln*-KO mice

Supplementary Fig. S2 (related to Fig. 1):

Specialized regional and cellular localization of Ocln protein in mouse epididymal epididymis.

- a. Immunofluorescent staining of WT, HE and *Ocln*-KO caput epididymal cryosections for Ocln.
- b. WB with the same antibody in WT and *Ocln*-KO DC2 cells.
- c. Regional and cellular specialized localization of Ocln protein in WT mouse epididymis. Epi-fluorescent images of different regions of epididymal cryosection immunostaining for anti-Ocln antibody (green) showing enriched in initial segment (IS) and caput (CPT) epididymidis. In initial segment, Ocln only present in the tight junctions (TJs) of principal cells. In the caput principal cells, Ocln also presents in the apical paracellular membranes (arrows). The quality of this antibody was confirmed by the absence of immunofluorescent labelled cellular structures in the epididymis of *Ocln*-KO versus WT mice, and the absence of 60-kDa band detected by WB analysis of protein extracts of *Ocln*-KO cells compared to WT DC2 cells as in B.
- d. Immunostaining for anti-HA-antibody different regions of epididymis showing enriched cellular localization of HA-Ocln in initial segment (IS) and caput (CPT) segments, particularly apical TJs as well as lateral membranes of principal cells, but undetectable in corpus (CPS) and cauda (CD) epididymidis of HA-Ocln tagged mice. Strong false positive of anti-HA immunostaining in the WT CPS and CD regions and weak level in the IS, suggesting endogenous HA expression in these regions and the false positive for HA-Ocln in these regions.
- e. Higher magnification confocal projection images showing co-localisation of ZO1 (red) with the enriched HA-Ocln (green) in the TJs (arrows) of caput epididymidis and weak levels in the lateral membranes (arrowheads) of cryosections from HA-Ocln mice.
- f. Higher magnification confocal projection images showing the intense fluorescence immune-stained using anti-HA antibody in the corpus epididymidis of both HA-Ocln and WT mice. Endogenous HA proteins were visible at a weak level in the initial segment and abundantly in the distal part of WT epididymis by using anti-HA antibody. WT controls were always included to prevent false positive interpretation.
- g. 3D-reconstruction confocal z-series images of immunolabelled mouse proximal caput epididymidis showing the absence of HA-Ocln (red) expression in the ZO1 (green) labelled membranes of clear marker B1-VATPase (blue).

Blue: DAPI. Scale bars: 10 μ m.

Supplementary Fig. S3 (related to Fig. 1):

Decreased late endocytotic vesicles and phalloidin-F-actin labelled granules in the caput principal cells in *Ocln*-KO compared with WT epididymis of adult mice.

- a. Confocal projection images showing the immunofluorescent staining of lysosome marker Lamp1 in caput epididymal principal cells of cryosections from *Ocln*-KO and WT mice
- b. The low magnification image of epididymal proximal regions showing the immunofluorescence for late endocytotic marker Rab7 was decreased in *Ocln*-KO compared with WT mice.
- c. Mouse caput epididymidis labelled for F-actin marker Phalloidin-TRITC (red). Very strong staining is seen in the principal cells stereocilia (arrows), smooth muscle cells

on the basal side, and in the numerous intracellular granular structures in the subapical domain of principal cells.

- d. Regional staining of F-actin marker Phalloidin-TRITC in epididymis of WT and *Ocln* KO mice showing decreased F-actin in the proximal epididymis where expressed high level of *Ocln*.

Blue: spermatozoa and DNA labeled with DAPI. *Lu*: lumen. Scale bars: 10 μ m.

Supplementary Fig. S4 (related to Fig. 1):

***Ocln*-KO results in altered cellular localization of claudin-3 at the apical and paracellular junctions of caput epididymal principal cells**

- a. Claudin-1, claudin-3 and claudin-4 immunofluorescent staining (red) in the different regions of epididymis from adult WT and KO mice. Clear cells were labeled for B1-V-ATPase in green. In the epididymis from KO mice, claudin-1 is found to upregulate throughout the entire length of epididymis with more prominent in the proximal parts. Claudin-3 protein is obviously upregulated in the proximal regions where *Ocln* is also enriched. Claudin-4 is upregulated prominently in the distal part of epididymis in KO mice, whereas the expression level in proximal parts is slightly decreased.
- b. Higher magnification confocal projection images showed significant upregulated claudin-3 in the tight junctions of caput principal cells in the KO epididymis, particularly the tricellular corners (arrows). Arrowheads indicate the large vesicle-like structures at the lower part of lateral membranes of epithelial cells.
- c. Upregulation of claudin-1 in the lateral membranes but not tight junctions of principal cells in the *Ocln*-KO compared to WT epididymis. The immunostaining intensity in basal cells remained unchanged (arrows).
Green: clear cells labeled with B1-V-ATPase, blue: spermatozoa and DNA labeled with DAPI. *Lu*: lumen. Scale bars: 10 μ m.

Supplementary Fig. S5 (related to Fig. 2):

High pressure freeze TEM images showing different kinds of intracellular vesicular organelles with arrested membrane fusion near the apical domains of principal cells of *Ocln*^{-/-} compared to *Ocln*^{+/+} proximal caput epididymis. PM: plasma membrane.

Supplementary Fig. S6 (related to Fig. 3):

Comparative analysis of transcriptomic and proteomic data.

- a. Volcano plots of all differential expressed genes (DEGs) obtained from RNAseq measurement using whole epididymis or caput epididymis of WT and *Ocln*-KO adult mice (n = 3 per group).
- b. Volcano plots of statistically significant DEGs in the datasets in penal a (Log fold-change > 1 or <1, false discovery rate (FDR) < 0.05).
- c. Venn graph showing the overlap of DEGs between the proteomics of whole epididymis and caput epididymis of WT and *Ocln*-KO adult mice (n = 3 per group).
- d. Venn graph showing the overlap of the matched transcriptomics statistically significant DEGs of (datasets in penal B) with proteomics (dataset in penal C) of whole epididymis and caput epididymis of WT and *Ocln*-KO adult mice. Proteomic data cut-off was 0.833 for down- and 1.2 for up-fold change of expression. The significant transcriptomic different expressed genes (DEGs) were obtained by matching the corresponding proteomes to give the shortlisted 150 DEGs in whole-epididymis, 230 in caput-only, and 52 common in both datasets.

Supplementary Fig. S7 (related to Fig. 3):

GO terms and KEGG pathway-enrichment analyses of the 150 genes shortlisted from the matched differential expressed mRNA seq and proteomic datasets of whole epididymis of *Ocln*-KO mutant compared to WT mice. (a) The bar graphs showing the up-regulated GO terms for biological processes (BP), molecular functions (MF), and cellular compartments (CC). (b) Downregulated GO terms. (c) Up-regulated KEGG pathway-enrichment terms. (d) Down-regulated KEGG pathway-enrichment terms.

Supplementary Fig. S8 (related to Fig. 3):

GO terms and KEGG pathway-enrichment analyses of the 230 genes shortlisted from the matched differential expressed transcriptomic and proteomic datasets of caput epididymidis of *Ocln*-KO mutant compared to WT mice. (a) The bar graphs show the up-regulated GO terms for biological processes (BP), molecular functions (MF), and cellular compartments (CC). (b) Downregulated GO terms. (c) Up-regulated KEGG pathway-enrichment terms. (d) Down-regulated KEGG pathway-enrichment terms.

Supplementary Fig. S9 (related to Fig. 3):

Integrative bioinformatic analysis of DEGs of *Ocln*-KO versus WT epididymis identify the key-core pathways involving phagosome, lysosome and immunometabolism networks

- a. Heatmaps of the 52 down- (a') and up-regulated (a'') DEGs that were common in the datasets of caput epididymidis and whole epididymis.
- b. Heatmaps of the key-core DEGs in the 178 down- (b') and up-regulated (b'') caput-only dataset. DEGs with negligible protein levels were excluded. Values are means of 3 animals per group per dataset.
- c. Heatmaps of the statistically significant transcriptomic DEGs in the 98 whole-epididymis dataset matched with whole-epididymis proteome. DEGs with negligible protein levels were excluded. Values are means of 3 animals per group per dataset.

Supplementary Fig. S10 (related to Fig. 3):

Additional integrative bioinformatic analyses of DEGs of *Ocln*-KO versus WT datasets.

- a. GO terms (a) and KEGG pathway-enrichment terms (b) of the 454 accumulated DEGs in the caput-only dataset with unchanged transcriptomic levels ($P > 0.05$) but significantly increased protein levels (protein fold-change > 1.2 , $P < 0.05$, $n = 3$ animals).
- c. Cytoscape plot of the enriched pathway network with terms in B. Circle size: $[-\text{Log}(P\text{-value})]$, border width: enrichment. Blue nodes: unique terms in this network compared to caput-only and whole-epididymis networks as shown in Fig. 3.

Supplementary Fig. S11 (related to Fig. 4):

Expression at the TJ and colocalization of Fcgr2b (green) with ZO1 (red) in various epithelial tissues. a. Kidney; b. small intestine; c. airway bronchia; d. endothelium in the blood vessels of choroid plexus. Blue: DAPI. Scale bars: 10 μm , unless indicated.

Supplementary Fig. S12 (related to Fig. 4):

Mosaic image of immunofluorescent stained for Vkorc1 (red) of epididymis cryosections of WT and *Ocln*-KO mice. The Vkorc1 immunofluorescence is higher in WT epididymis, particularly in the CPS region where weak or negligible *Ocln* is expressed (see Figure S1). The overall expression level of Vkorc1 is significantly decreased in the KO tissues, whereas expression in IS segment remains relative higher than the downstream segments. Insert: Transcriptomic and proteomic profiles of DEGs

in VK-dependent carboxylation pathway of *Ocln*-KO and WT of whole epididymis and caput epididymidis. Data were means \pm SD (n=3 mice per group). * P <0.05, ** P <0.01, **** P <0.0001, unpaired student's t -test. Because the unmatched cellular localization between *Vkorc1* and *Ocln*, these results suggest that the regulation of *Vkorc1* expression by *Ocln* is indirect. Scale bar: 1000 μ m.

Supplementary Fig. S13 (related to Fig. 4):

- a. Regional and cellular specialized localization of the downstream substrate of *Ggcx/Vkorc1* cycle dependent carboxylation pathway, MGP (green), and ApoJ (red) in *Ocln*-KO compared with WT mouse epididymis. In the WT initial segment (IS), MGP is mainly present Golgi network, indicating its secretion in this region. In the WT caput, corpus and cauda epididymidis, MGP is mainly in small granular form throughout the epithelial cells as well as in the luminal contents. In some of the intracellular endocytotic vesicles, co-localisations of MGP and ApoJ were observed in both WT and *Ocln*-KO epithelial cells, but the overall expression of MGP was higher in WT than in the *Ocln*-KO epididymis.
- b. The levels of Gla proteins, all the downstream substrate of *Ggcx/Vkorc1* cycle dependent carboxylation pathway, were determined by using anti-Gla-residues antibody (red). The overall level of Gla-residues is an indicative of carboxylation level and the activity of *Ggcx*-mediated VK-dependent redox cycle. The increased Gla-residues in the *Ocln*-KO epididymal epithelial cells suggested an increased *Ggcx*-mediated VK-dependent redox-sensitive carboxylation activity.
Scale bar: 10 μ m. Blue: DNA labelled with DAPI. IS: initial segment; pCPT & dCPT: proximal and distal caput; CPS: corpus; dCD: distal cauda epididymidis.

Supplementary Fig. S14 (related to Fig. 4):

Increased immunofluorescence of total Gla-residues containing proteins in airway bronchi and lung alveoli of *Ocln*^{-/-} compared to *Ocln*^{+/+} mice. Scale bars: 10 μ m. Blue: DNA labelled with DAPI.

Supplementary Fig. S15 (related to Fig. 5):

Quantification summary of the CTxB endocytosis assay with monolayer of WT or *Ocln* KO DC2 cells pre-loaded CTxB on cold following challenged to rewarm to 37°C for different times, before PLP fixation on cold and immunostained using CTxB antibody. Quantification of CTxB fluorescence signals in cells were performed on images acquired with same parameters. Each data point of CTxB endocytosis measurements represents at least 15 cells from images of 3 individual experiments, and per each cell 3 lines of CTxB intensity were measured from plasma membrane (zero position) towards nuclear.

Supplementary Fig. S16 (related to Fig. 5):

Whole-cell recordings of passive membrane properties of WT and *Ocln*-KO DC2 cells.

- a. Typical current response of a cell to the 10-mV hyperpolarization step with a holding potential of -60 mV.
- b. Tracings showing the transient current responses during the 10-mV hyperpolarization steps evoked with a WT or a KO DC2 cell.
- c. Tracings showing the transient currents of an outlier KO cell and a normal WT cell in response to repolarization.
- d. Representative whole-cell capacitance during the time course of repeatedly hyperpolarization (C_{m-H}) and repolarization (C_{m-R}) and the corresponding conductance (G_{m-H} and G_{m-R}) in WT and KO cells.

- e, f**) Quantification of the changes of capacitance (ΔC_m) and conductance (ΔG_m) of WT (n = 10) and Ocln KO cells (n = 6). **g**) Digital subtracted capacitance ($\Delta C_{m-subtraction}$) of the repolarization-induced capacitance from that of hypolarization-triggered response of the same cells. **g, i**) Time constant of the raised current upon repolarization and the pre-pulse resting current density of the same cells as in panels e and f. Arrows indicate the time lag in tens of seconds before the sustained increment in cell membrane capacitance of WT cells. Data were mean \pm SD. * $P < 0.05$, **** $P < 0.001$, two-way ANOVA.

Supplementary Fig. S17 (related to Fig. 5):

3D-reconstruction and orthogonal view of immunofluorescent staining for anti-flotillin-1 antibody showing its presence in the intracellular vesicular organelles and the apical and paracellular membranes of WT caput cells. Punctae of flotillin-1 were also found on the luminal face of the TJs of caput principal cells. Scale bar: 10 μ m. Blue: DNA labelled with DAPI.

Supplementary Fig. S18 (related to Fig. 5):

Live cell imaging showing macro-endocytosis in cells expressing GFP-tagged Ocln protein (green) and loaded with lysotracker (red). Images with indicated time showing the vesicle-like structures dynamically forming along the Ocln-expressed paracellular membranes between adjacent cells. Arrows indicate the time series of endocytosis process of a vesicle which can lateral diffuse before invagination and later pitching off from the membrane, and interestingly, the vesicle is elongated after the first invagination before completely detaching off from the membrane. Transient GFP-tagged Ocln protein expressed DC2 cells were grown to monolayer with cell-cell adhesion maturely formed as revealed by the uniform Ocln-GFP expression along the paracellular membranes between the two adjacent cells. Scale bar, 2 μ m.

Supplementary Fig. S19 (related to Fig. 7):

Immunoprecipitation following mass-spectrometry analysis of Ocln-N-Flag proteome with an anti-flag antibody from overexpressed DC2 cells.

- a.** KEGG pathways and reactome enrichment terms of the top key-core genes obtained from IP-MS proteome of overexpressed with Ocln-N-Flag plasmid in DC2 cells (n=3, two rounds of mass spectrometry).
- b, (b-c)** 3D-reconstruction and orthogonal view of double-immunolabelling for antigen-presenting protein Capzb (**b**) or Ppia (**c**) and with ZO1 (red) of WT and *Ocln*-KO mouse epididymis. Arrowheads: Capzb at TJ. Asterisks in B: Capzb-positive immunological cells. **(d)** Confocal projection of images showing double-immunolabelling for exosome marker Hsp90 (green) and ZO1 (red). Inset: higher 3D-reconstruction and orthogonal view of HSP90 on the ZO1-labeled TJs of caput principal cells of WT and *Ocln*-KO mice. Arrows in Double-arrow in d: Hsp90-positive granules around stereo-cilia of principal cells.

Scale bar: 10 μ m. Blue: DNA labelled with DAPI. *Lu*: lumen.

Supplementary Fig. S20 (related to Fig. 7):

- a.** Confocal images showing the regional for the co-localisations of ATP5b (green) and HA-Ocln (red) in proximal segments of mouse epididymis of HA-Ocln mice.
- b.** Confocal images showing the regional for the co-localisations ApoJ (green) and HA-Ocln (red) in proximal segments of mouse epididymis of HA-Ocln mice.
- c.** 3D-reconstruction of higher magnification confocal images showing the numerous co-localisations of ATP5b (green) and HA-Ocln (red) in the paracellular membranes and

in the intracellular vesicular structures of principal cells of distal caput epididymidis. Arrows indicate one example of the co-localisation.

- d. 3D-reconstruction of higher magnification confocal images showing the co-localisation of ApoJ (green) and HA-Ocln (red). Arrows indicate the co-localisation near the apical surface.

Blue: spermatozoa and DNA labeled with DAPI. *Lu*: lumen. Scale bars: 5-10 μm .

Supplementary Fig. S21 (related to Fig. 7):

Regional and cellular specialized localization of early endosome Eea1 (green) and ApoJ (red) in *Ocln*-KO compared with that of WT epididymis. Scale bar: 10 μm . Blue: DNA labelled with DAPI. IS: initial segment; pCPT: proximal caput; CPS: corpus; pCD: proximal cauda epididymidis.

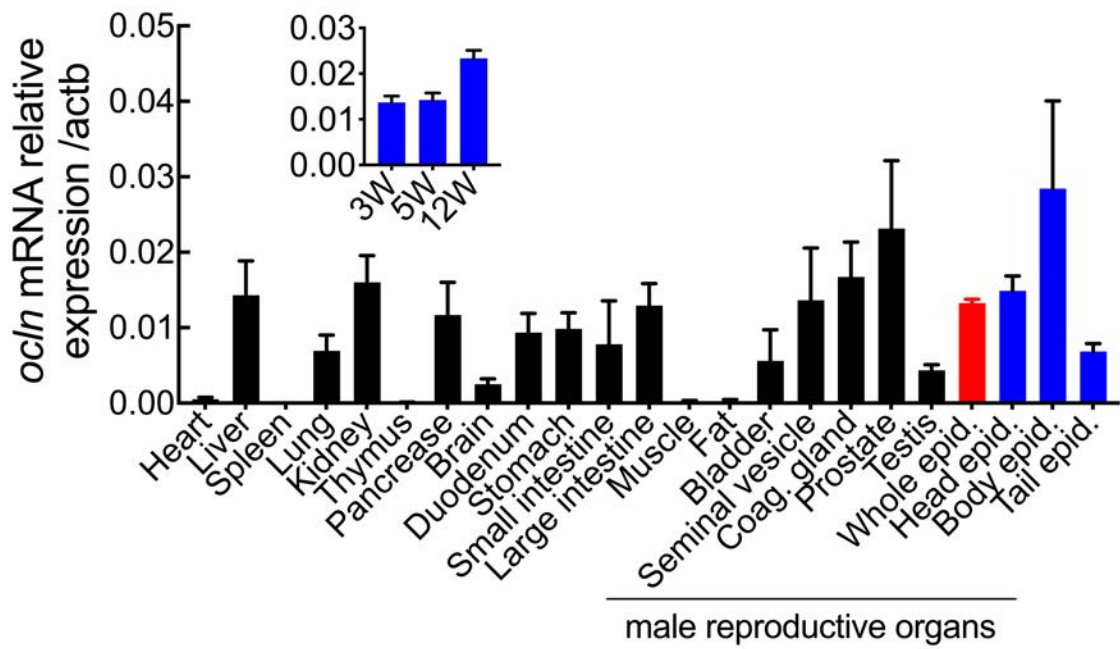


Fig. S1_(related to Fig. 1)

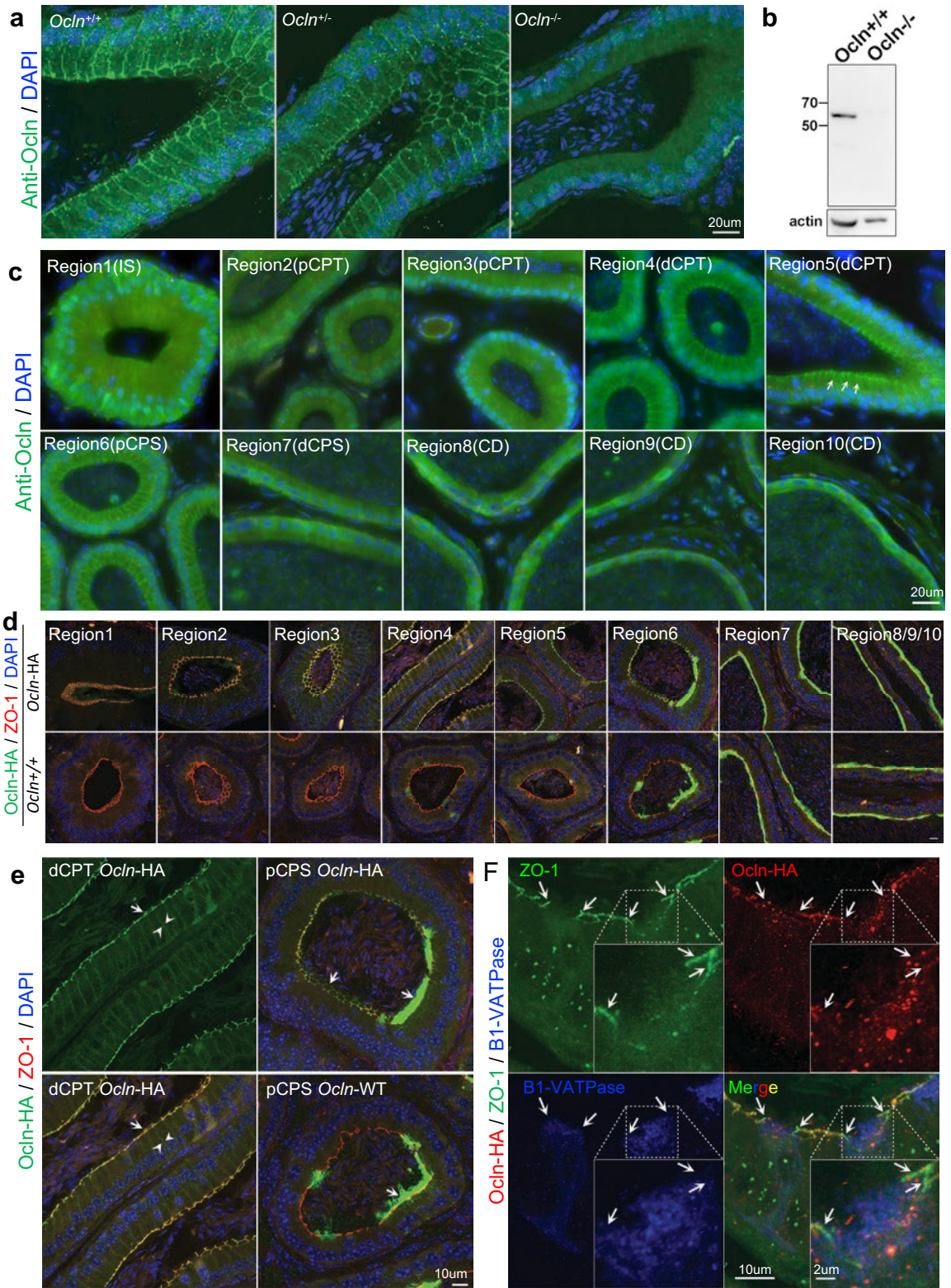


Fig. S2_(related to Fig. 1)

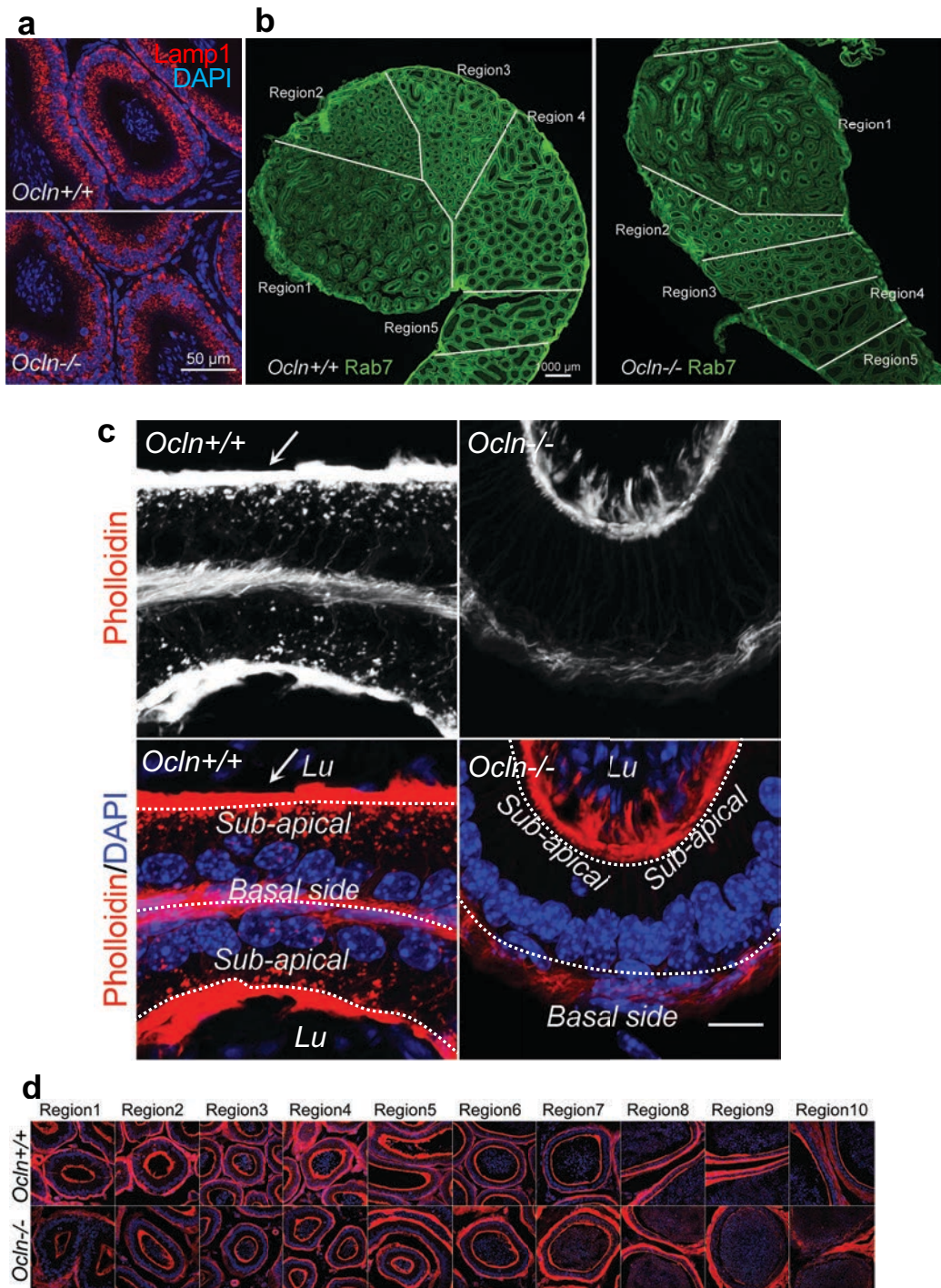


Fig. S3_(related to Fig. 1)

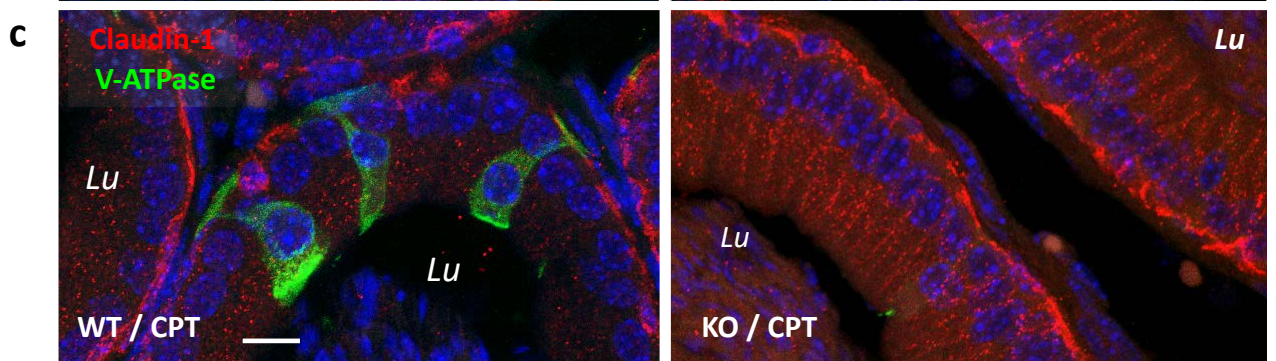
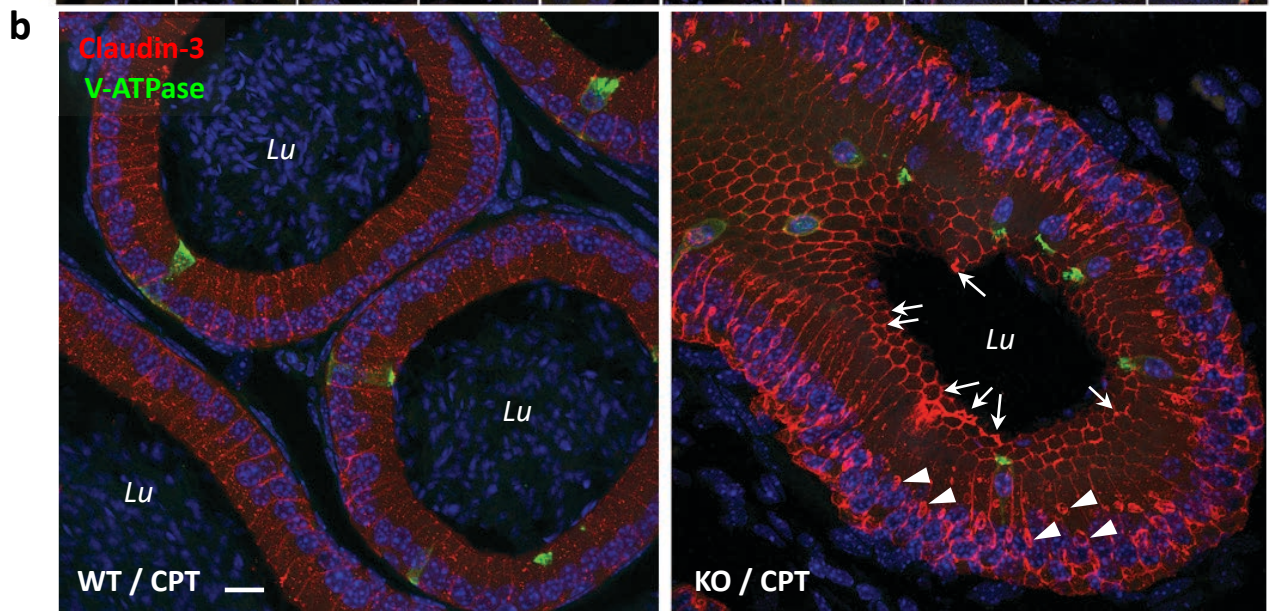
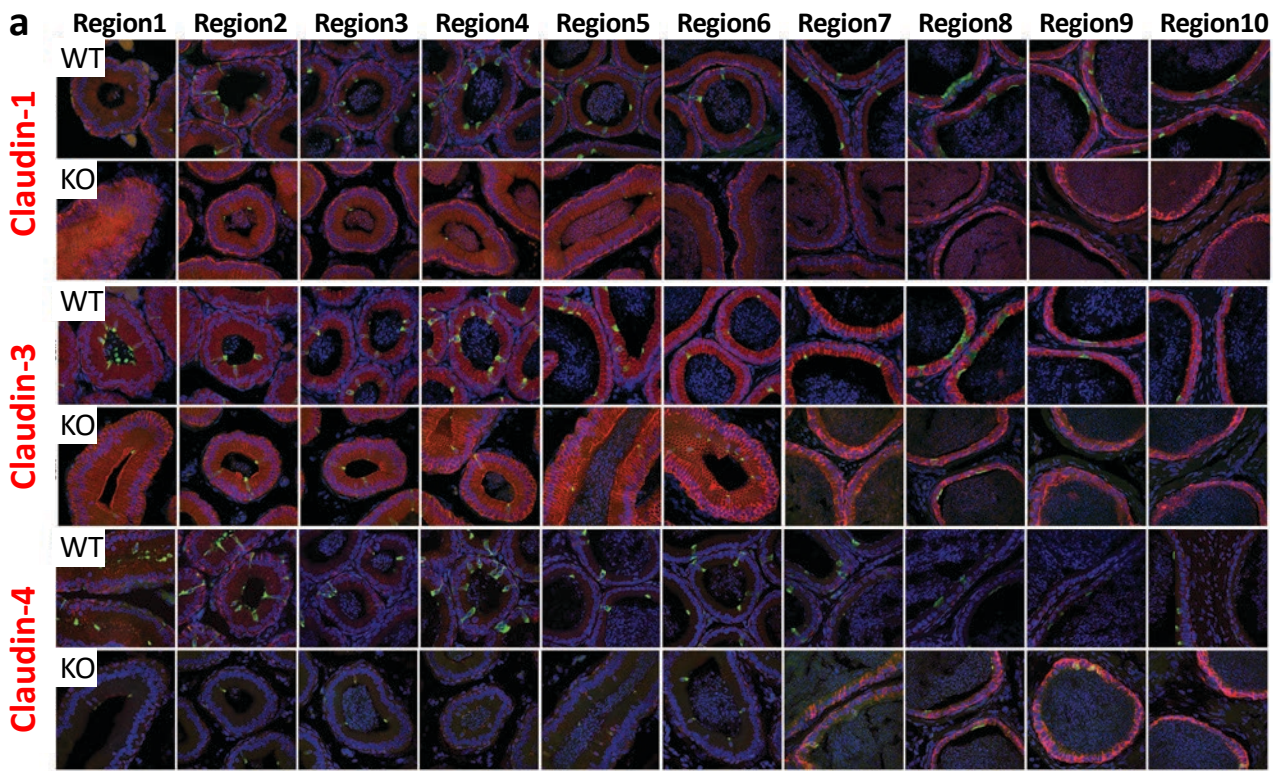


Fig. S4_(related to Fig. 1)

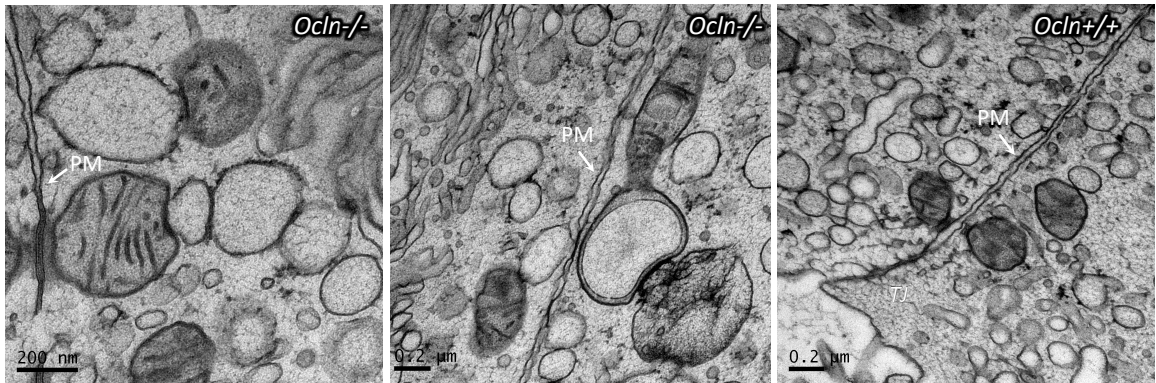


Fig. S5_(related to Fig. 2):

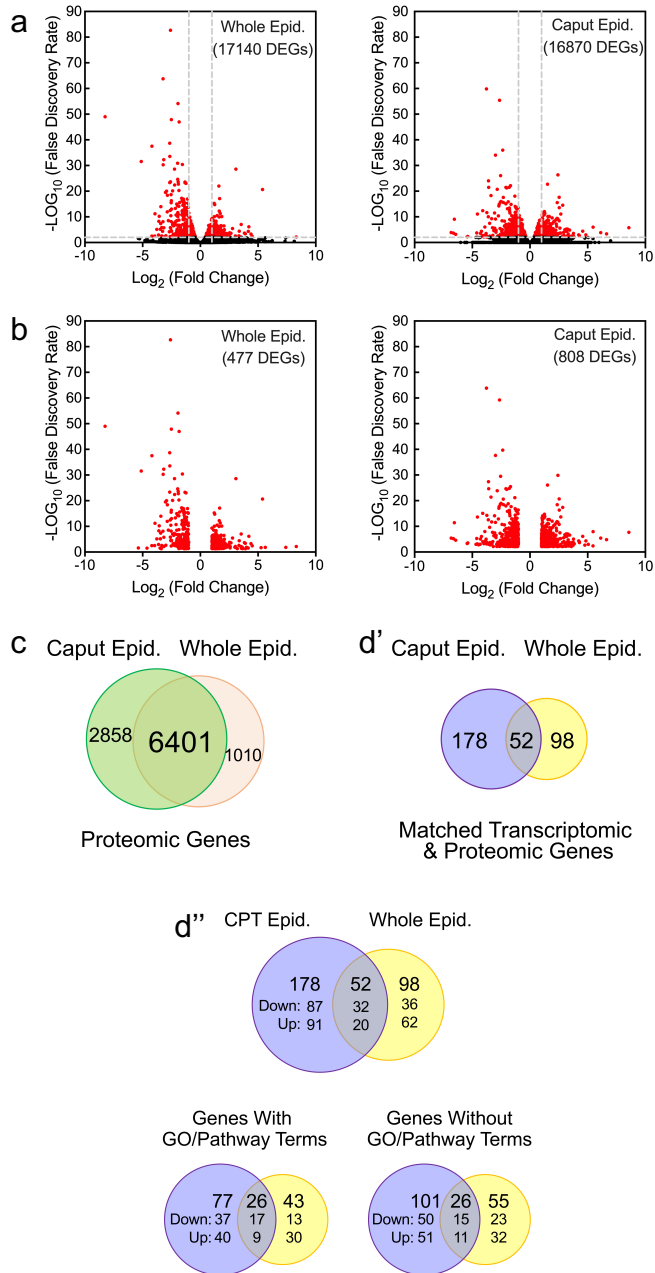


Fig. S6 (related to Fig. 3)

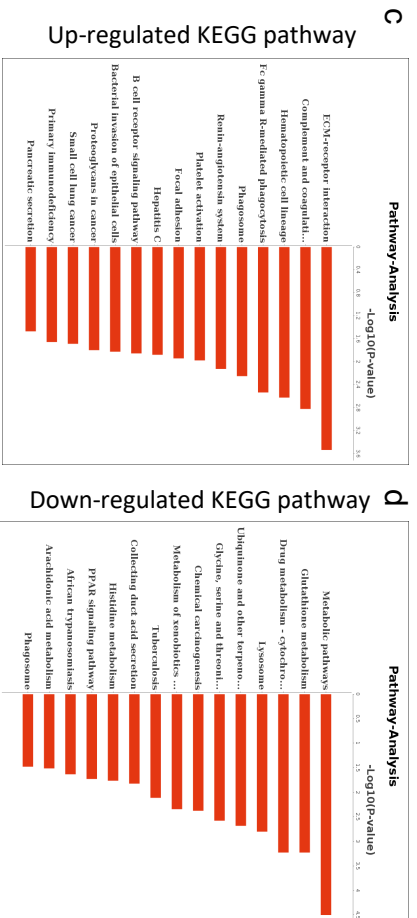
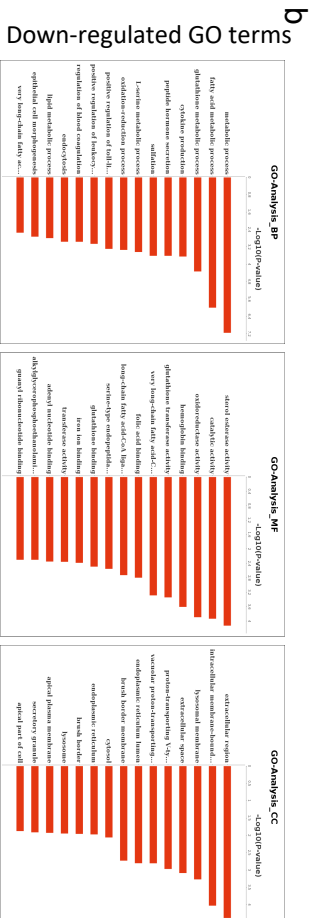
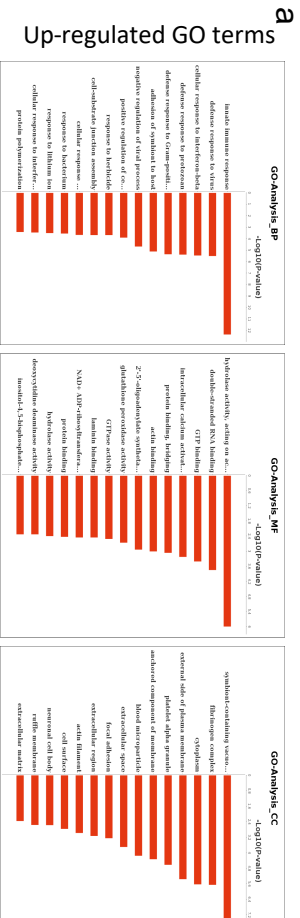


Fig. S8 (related to Fig. 3)

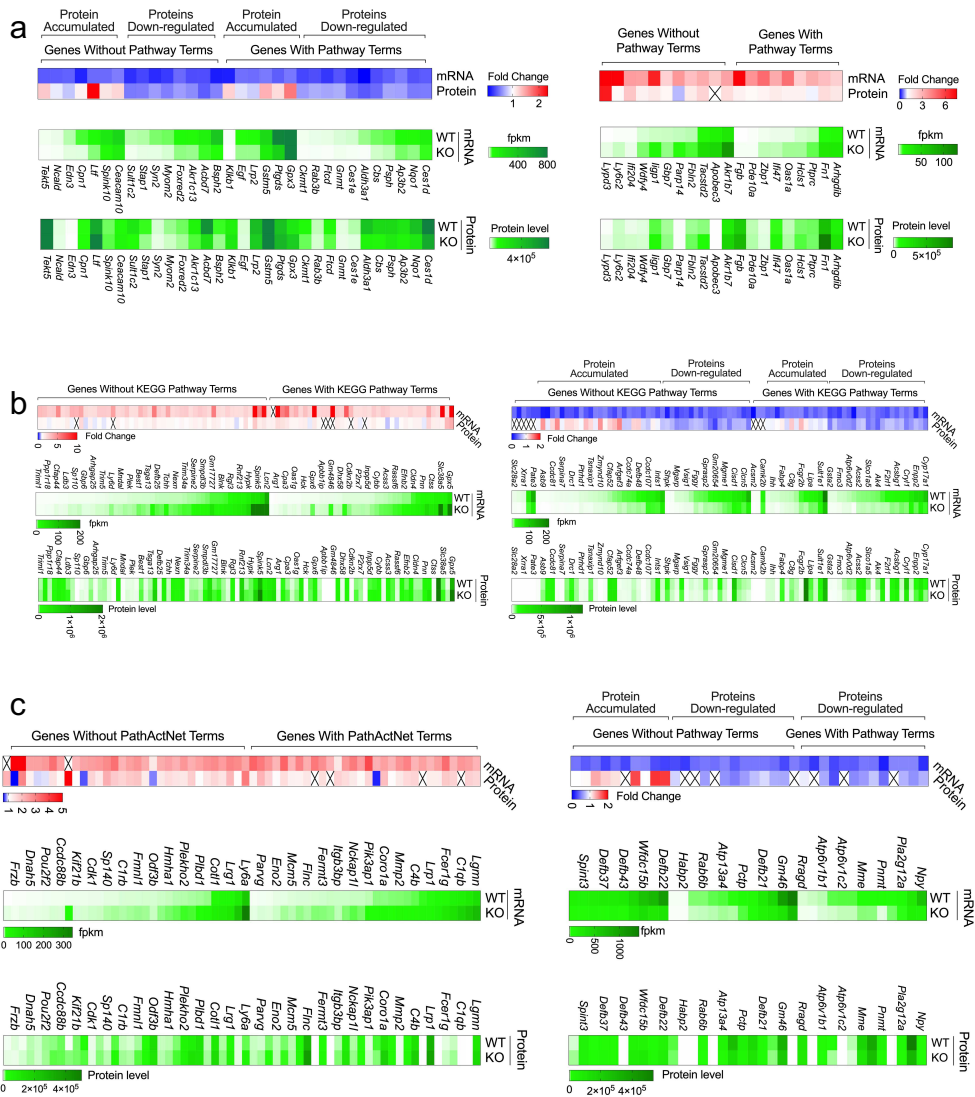


Fig. S9 (related to Fig. 3)

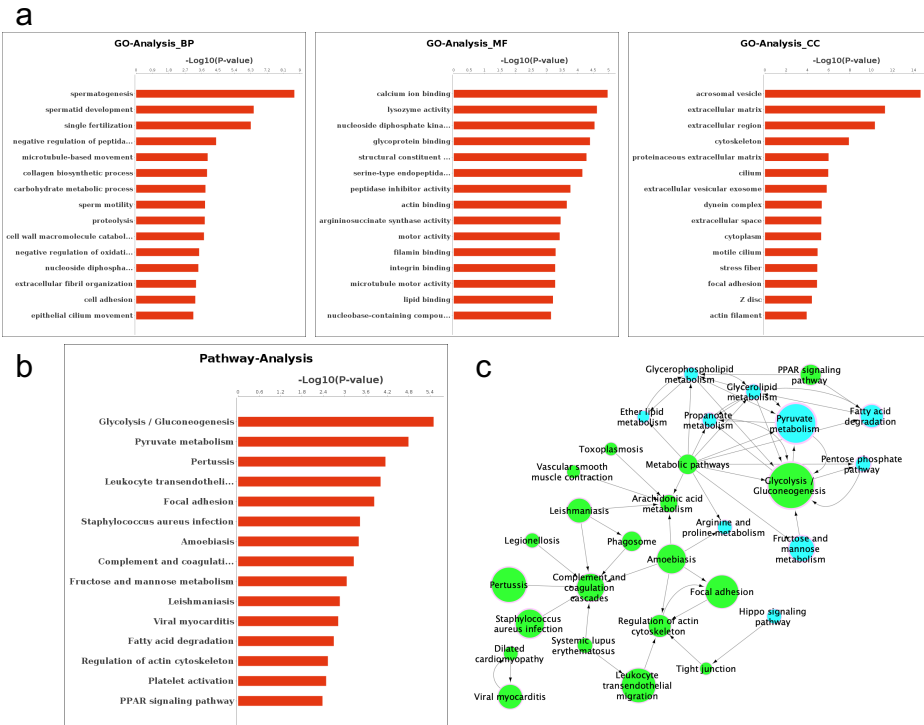


Fig. S10 (related to Fig. 3)

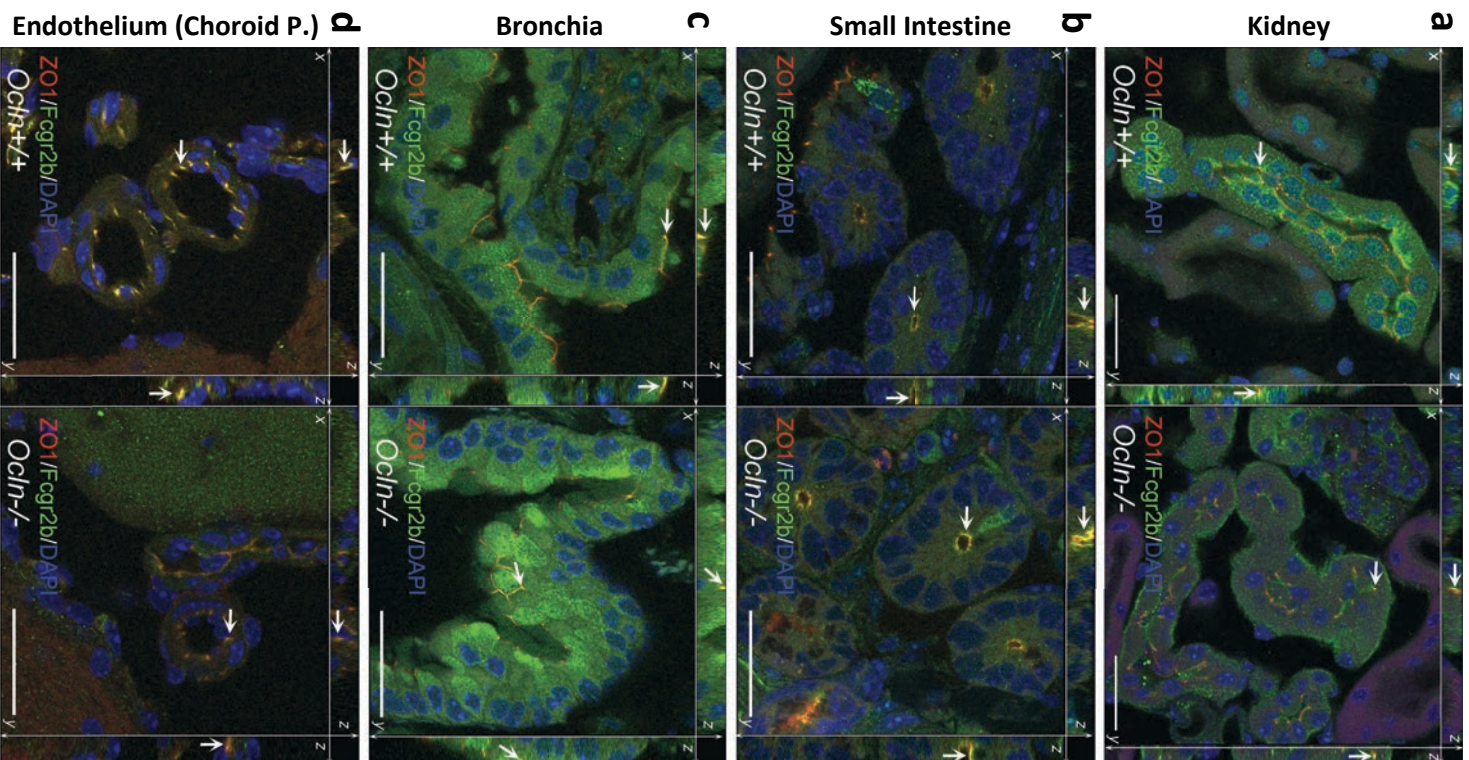


Fig. S11_(related to Fig. 1)

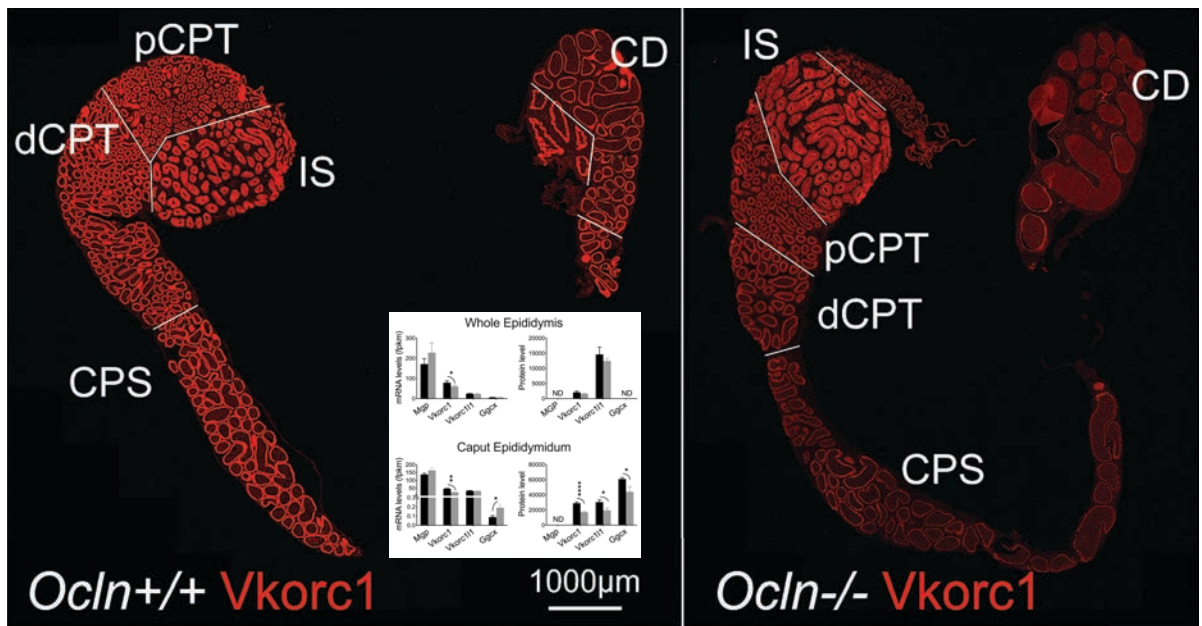


Fig. S12 (related to Fig. 4)

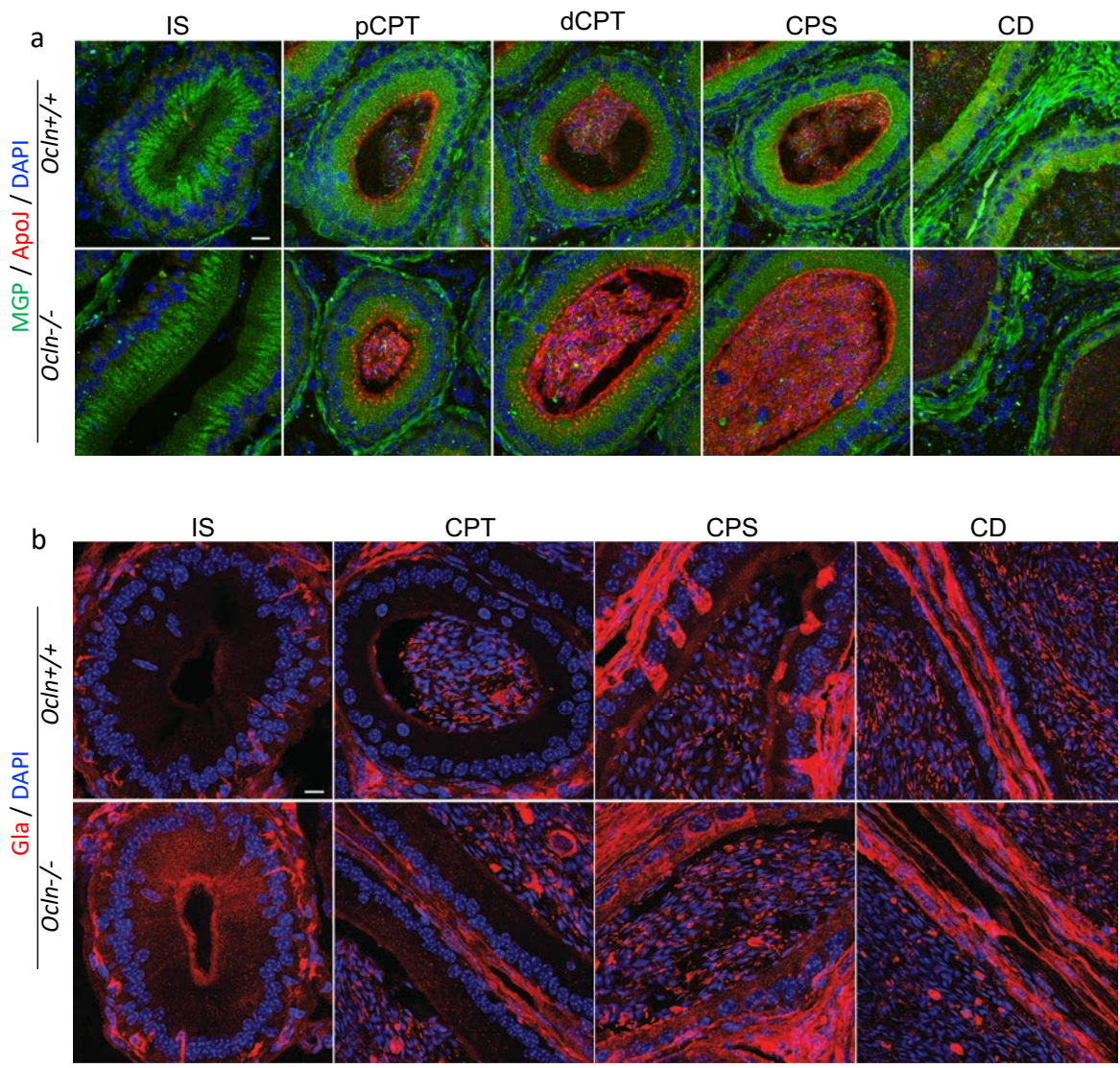


Fig. S13 (related to Fig. 4)

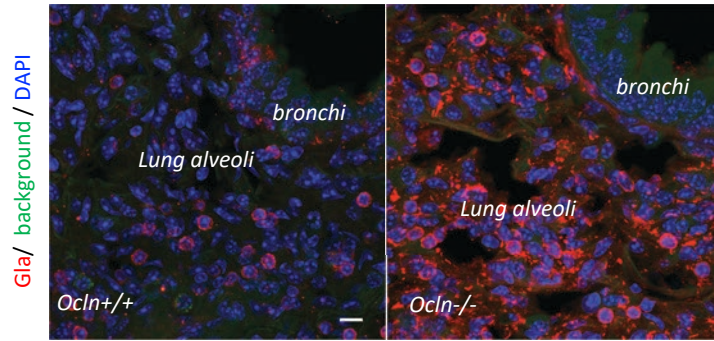


Fig. S14_(related to Fig. 1)

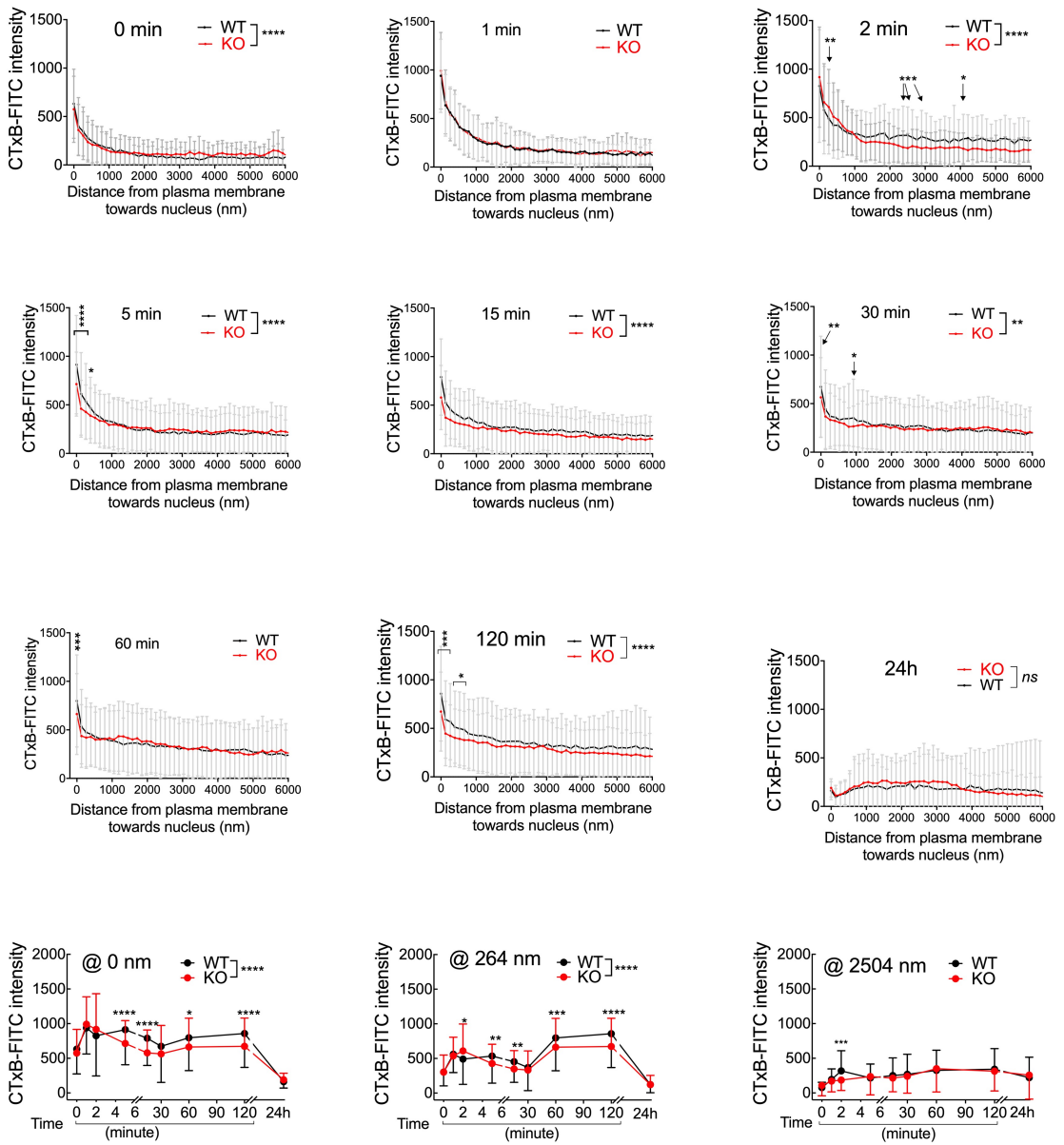


Fig. S15 (related to Fig. 5):

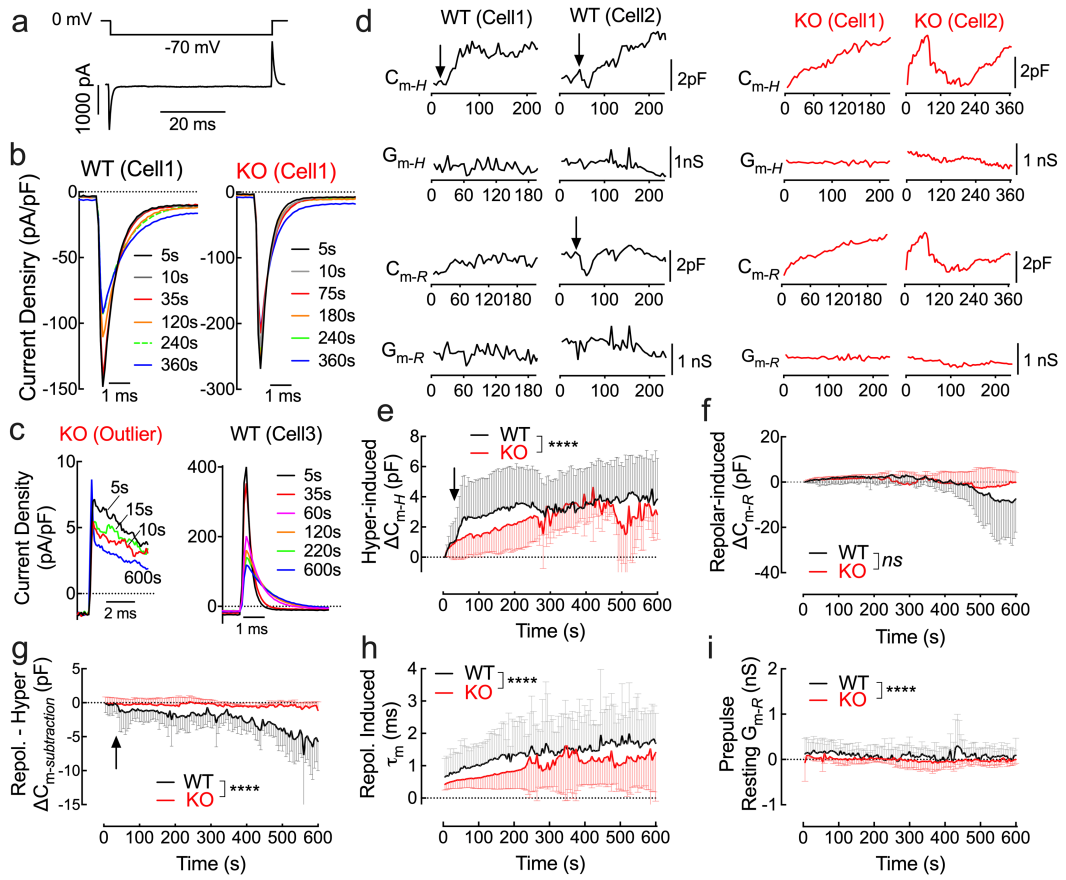


Fig. S16 (related to Fig. 5):

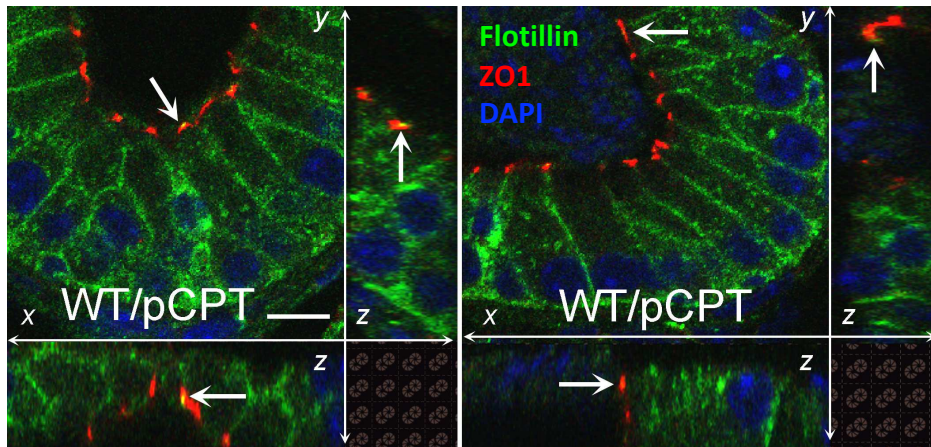


Fig. S17 (related to Fig. 5):

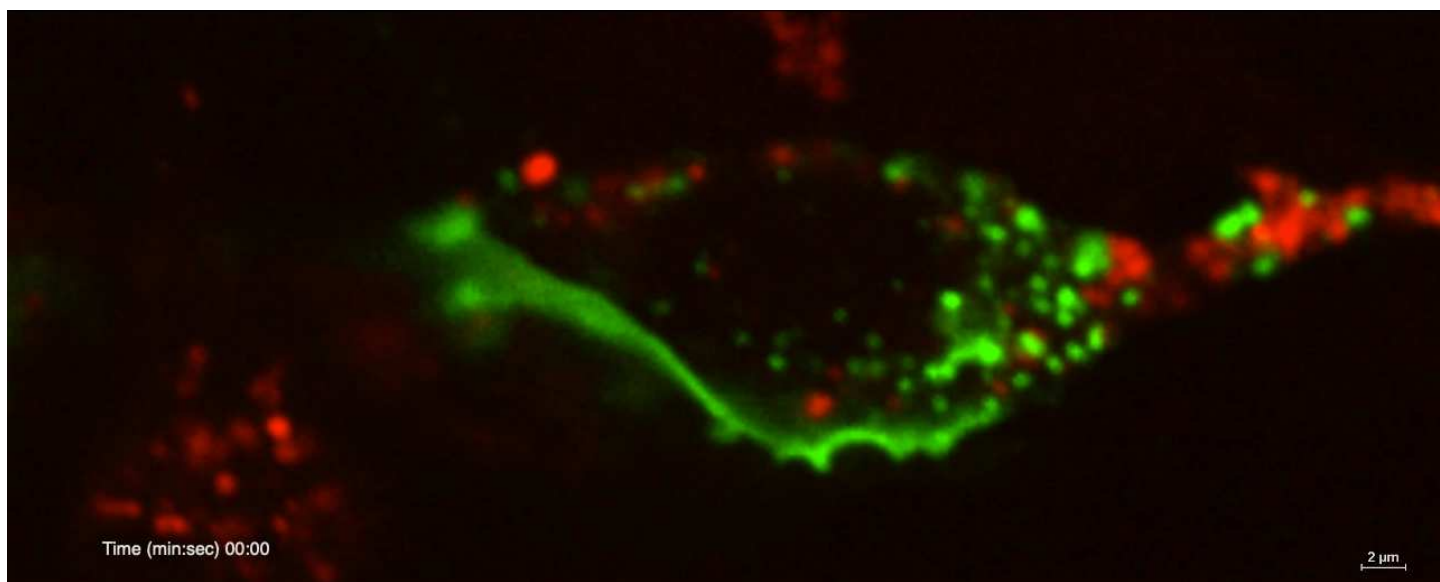


Fig. S18 (movie)(related to Fig. 5):

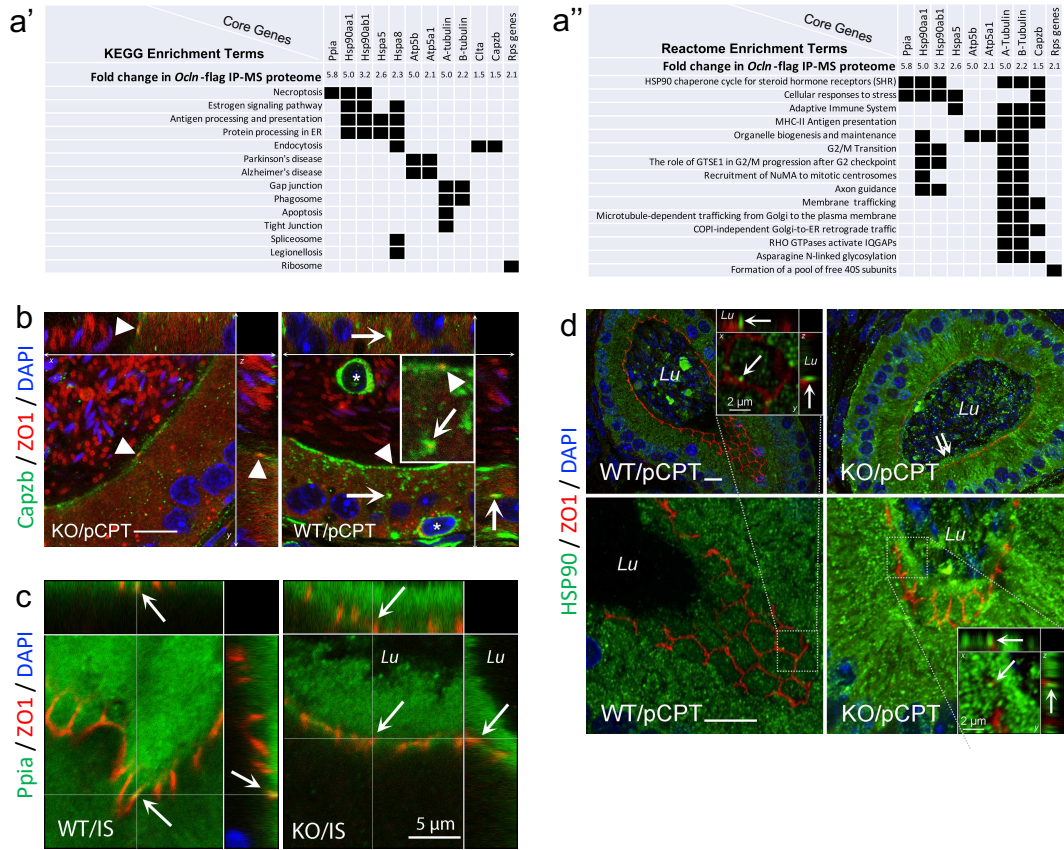


Fig. S19 (related to Fig. 7)

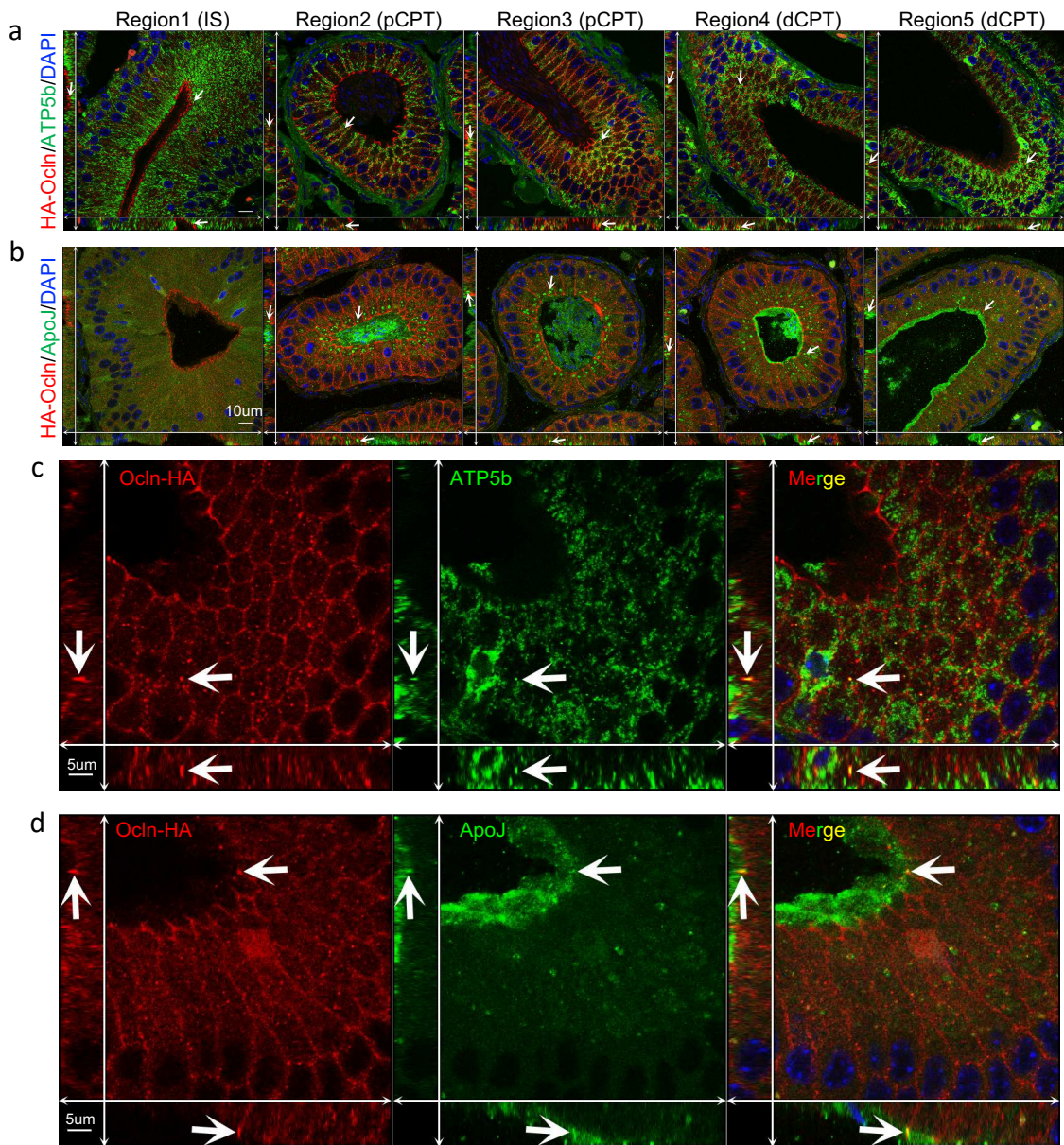


Fig. S20 (related to Fig. 7)

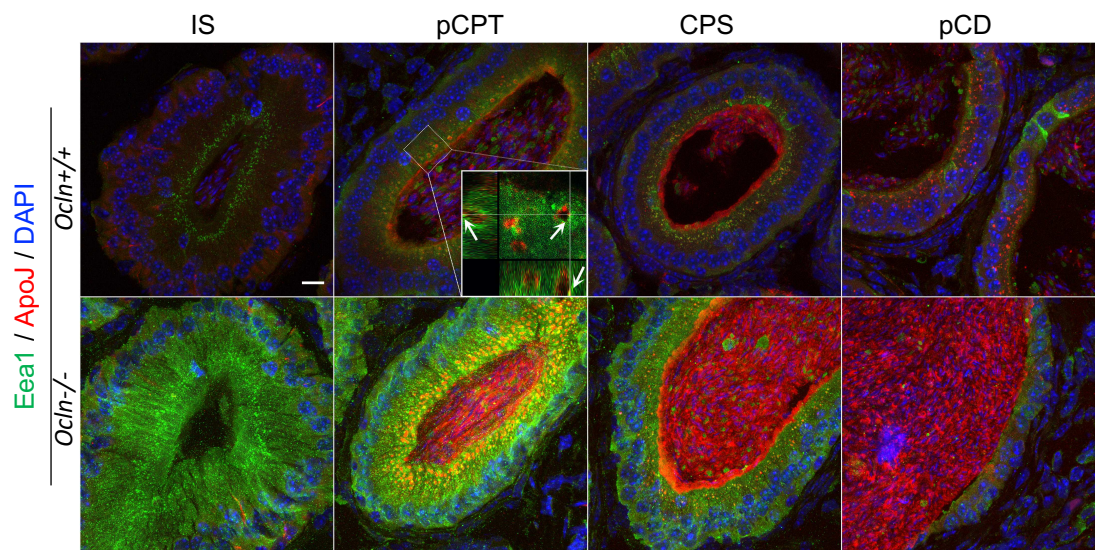


Fig. S21 (related to Fig. 7)

Figures

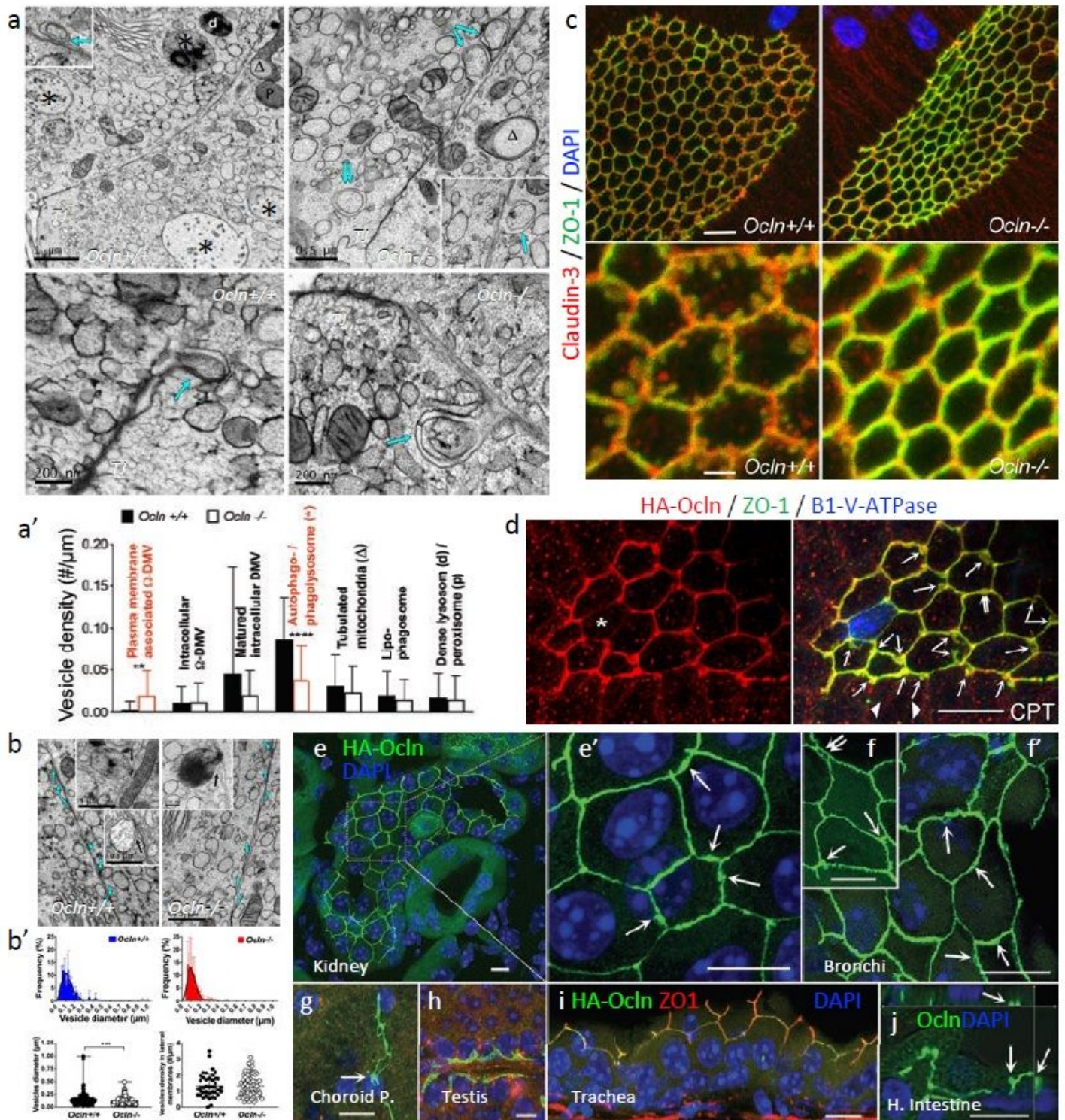


Figure 1

Ocln-KO have arrested paracellular heterophagy in *Ocln*-enriched plasma membrane and degenerated phagolysosome in epididymal epithelial cells. Typical HPF-TEM images showing the intracellular organelles in apical paracellular domains of caput epididymal principal cells of adult mice. White

arrows: hemi-fused W-shaped double-membrane vesicles beneath the proximal TJ paracellular membrane (pm-W-DMVs). Double-arrow: a DMV containing TJ-like texture in the vesicle lumen with its outer membrane still partially linked to the TJ components. Asterisks: phagolysosomes. Scale bars: 0.2 – 1 μ m. (a') Quantification of different vesicles (>10 cells from 3 mice per group). b. HPF-TEM images and (b') quantification of the vesicles (white arrows) docked to paracellular membrane in caput epididymidal cells. Black arrows: plasma membrane associated vacuolar vesicles. c. Double-immunolabeled for ZO1 and Cldn-3 of proximal caput (pCPT) of Ocln+/+ and Ocln-/- mice. Higher magnification images showing numerous vesicular structures of heterogenous sizes in the TJs of WT epithelial cells but nearly absent in the same region of KO epididymis. d. Confocal projection images of immunolabelled mouse proximal caput epididymidis for anti-HA-Ocln, ZO1 and B1-VATPase. Arrows: paraphagy-like structures near tricellular corners. Double-arrow: paraphagy-like structures at paracellular TJs. Arrowheads: weak paracellular level of HA-Ocln. Asterisk: a clear cell with negligible level of HA-Ocln. e. Kidney cortical collecting duct and (f) bronchial epithelium from HA-Ocln tag mice stained for anti-HA antibody. (e' and f') Higher magnification image showing the paraphagy-like structures at paracellular TJs of renal principal cells (arrows) as well as in endothelial capillary cells in choroid plexus (g). (h and i) Absence of dynamic structures in the TJs stained for anti-HA-Ocln in epithelial cells of trachea and testis. Red: ZO1 in h and i. j. The presence of a vesicular-structure (arrows) derived from the anti-Ocln antibody labelled TJs in human small intestine (H. Intestine).

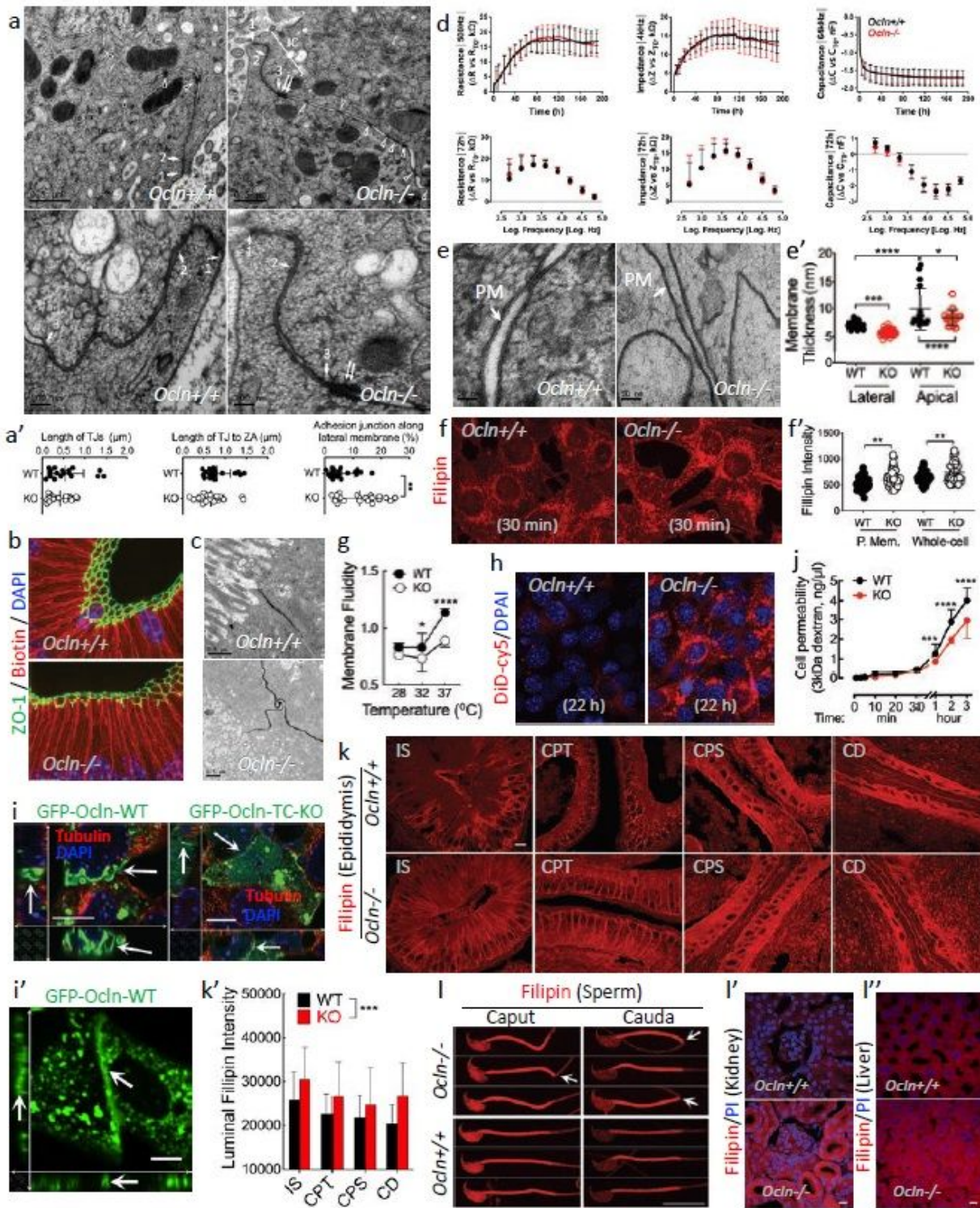


Figure 2

Ocln is essential to prevent cholesterol accumulation but not epithelial barrier integrity a. Typical HPF-TEM images showing paracellular junctional structures in caput epithelial cells of adult *Ocln*^{+/+} and *Ocln*^{-/-} mice. TJ: arrows 1 to 2; ZA (zonula adhaerens): arrows 2 to 3; desmosome: double-arrow; adherens junctions: arrowheads. Junctional complex (JC) composing TJ, ZA and desmosome occasionally present. Quantification of the junctional structures (a'). ** $P < 0.01$ unpaired t-test (n=3 mice)

per group). b. No detectable biotin immunofluorescent-staining in the lumen of epididymis of perfused mice. Green: ZO-1. c. TEM images of mouse caput epididymal cells perfused with paracellular tracer lanthanum. d. Electric cell-substrate impedance sensing (ECIS) measurement results showed no difference in impedance and capacitance at higher frequencies nor resistance at low frequencies, suggesting no difference in tight junction integrity, cell monolayer covered surface area, as well as similar attachment and spreading of cellular behaviors in *Ocln*^{+/+} and *Ocln*^{-/-} DC2 cells. e. TEM images showing part of the paracellular plasma membrane (PM) in the caput epididymal principal cells of mice. Quantification showing decreased membrane thickness in *Ocln*^{-/-} vs WT cells. f. Fluorescent images showing filipin-labelled (30min incubation) cholesterol in *Ocln*^{+/+} and *Ocln*^{-/-} DC2 cells. Quantification of cholesterol levels in these cells. g. Membrane fluidity of *Ocln*^{+/+} and *Ocln*^{-/-} DC2 cells. h. Images showing accumulated lipophilic dye DiD-885 Cy5 after 22 h incubation with *Ocln*^{+/+} and *Ocln*^{-/-} DC2 cells before fixation. i. 3D-reconstruction of confocal stack images showing the features of paracellular membranes in WT DC2 cells transfected with truncated KO *Ocln*-C-GFP or WT N GFP-*Ocln*, and *Ocln*-KO cells transfected with WT GFP-N-*Ocln* (i'). j. Transepithelial transport assay of 3kDa dextran in *Ocln*^{+/+} and *Ocln*^{-/-} monolayer DC2 cells (n=9). k. Filipin fluorescence profiles in the epididymal epithelial cells. (k') Quantification of filipin intensity in the luminal contents of different epididymal regions (n=3 mice per group). l. *Ocln*^{+/+} and *Ocln*^{-/-} spermatozoa (l), kidney tubules (l') and liver (l'') labeled with6 filipin. Blue: DNA stained with DAPI. Scale bars: 10 μ m, unless specified.

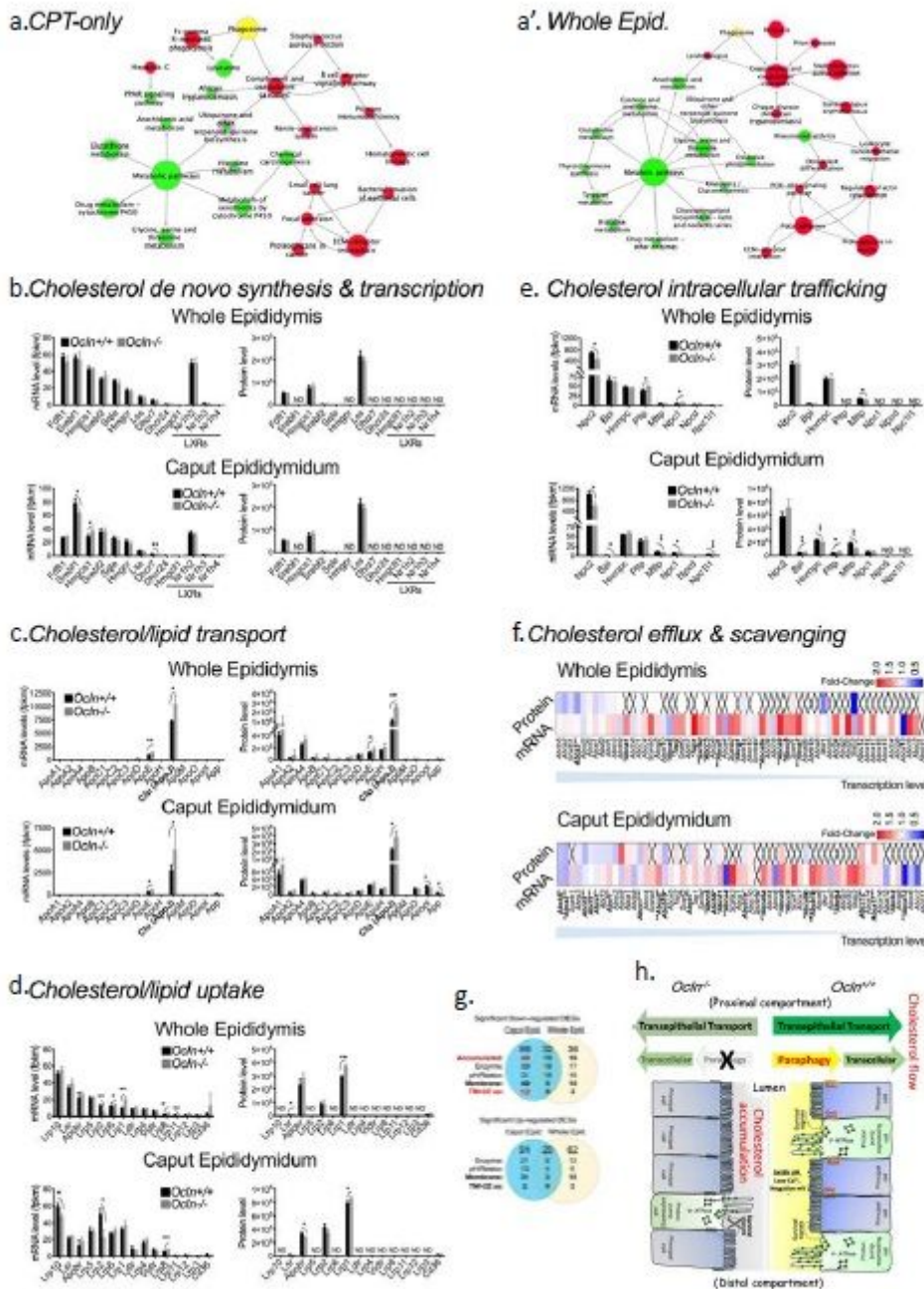


Figure 3

Ocln regulates phagosome-associated cholesterol transport and metabolic pathways. Cytoscape plots of KEGG-based PathActNet analyses with shortlisted proteomic and transcriptomic DEGs of caput-only and whole epididymis. Circle size: $[-\log(P\text{-value})]$, border width: enrichment. Green: downregulated, red: upregulated, yellow: both downregulated and up-regulated pathways. (b-f) DEGs Expression profiles associated with cholesterol homeostatic pathways of whole epididymis and caput epididymidis. (b) Cholesterol de novo synthesis, (c) extracellular transport, (d) uptake, (e) intracellular trafficking, and (f) cholesterol efflux and scavenging pathways. Data were means \pm SD (n=3 mice per group). *P<0.05, ** P<0.01, *** P<0.001, unpaired student's t-test. Cross sign: undetectable level. g. Venn graphs of categorized transcripts of the significant 910 down- and up-regulated DEGs datasets. h. Graphic summary of a

hypothetical model of Ocln-promoted parapagy in cholesterol transepithelial transport in epididymal epithelium.

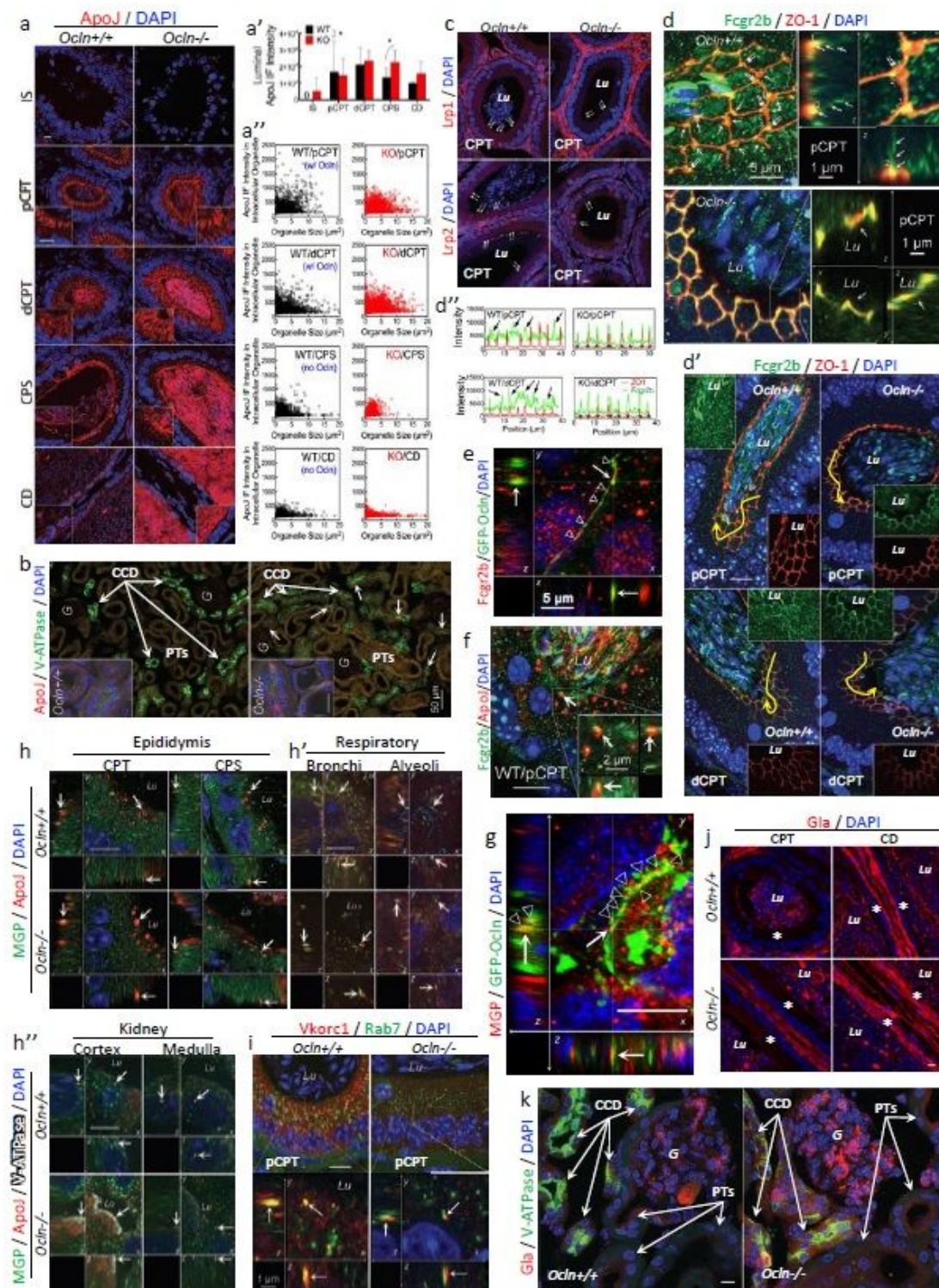


Figure 4

Ocln-mediated parapagy confers protection from cholesterol accumulation and lipophilic ectopic deposition, partly through vitamin-K dependent carboxylation. a. Confocal projection images showing ApoJ subcellular localization in different regions of Ocln^{+/+} and Ocln^{-/-} mouse epididymis.

Quantification bar graph of luminal ApoJ intensity (a') and scatter plot (a'') of ApoJ+ intensity in organelles of epithelial cells measured on projected images with Volocity (n=3 mice per group). b. Kidney cryosections immunostained for ApoJ showing its presence in principal cells of cortical collecting duct of adult mice. V-ATPase: intercalated cells. G: glomerulus. Arrows: renal cells with accumulated ApoJ. Insert: higher magnification of proximal tubules. c. No immunostaining signals for Lrp1 and Lrp2 in the apical surface (arrows) of caput epithelial cells of adult mice. d. The presence of numerous paraphagy-like structures (arrows) positive for Fcgr2b (green) with ZO1 (red) at the TJs of WT caput epithelial cells and the contained co localization in the Ocln-KO caput cells. Doublearrows: scaffolding Accumulated of Fcgr2b at the TJs in the Ocln-/- caput cells compared to that of Ocln+/+ mice. Yellow arrows indicate the position for the Fcgr2b immunofluorescent intensity profiles as plotted in d''. Dispersed immunostained Fcgr2b intensity (arrows) beyond the TJs structures (ZO1 in red) on the apex of Ocln+/+ caput 934 cells versus the contained Fcgr2b intensity within the TJs structures (asterisks) in Ocln-/- caput cells. e. Fcgr2b and GPF-N-Ocln co-localizations (arrow and arrowheads) in DC2 cells. f. Fcgr2b and ApoJ co-localizations in the epididymal caput cells of adult WT mice. g. Co-localizations (arrow and arrowheads) of MGP and GPF-N-Ocln in DC2 cells. h. The presence of MGP within the ApoJ magnification of 3D-orthogonal view showing colocalization of Vkorc1 and Rab7 in Ocln+/+ but not in Ocln-/- caput cells. j. Increased immunofluorescence of total Gla-residues containing proteins in epididymal epithelial cells (asterisks) of Ocln-/- compared to Ocln+/+ mice. k. Kidney cortical collecting duct (CCD) and proximal tubules (PTs). Lu: Lumen. Scale bars: 10 μ m. Blue: DNA labelled with DAPI.

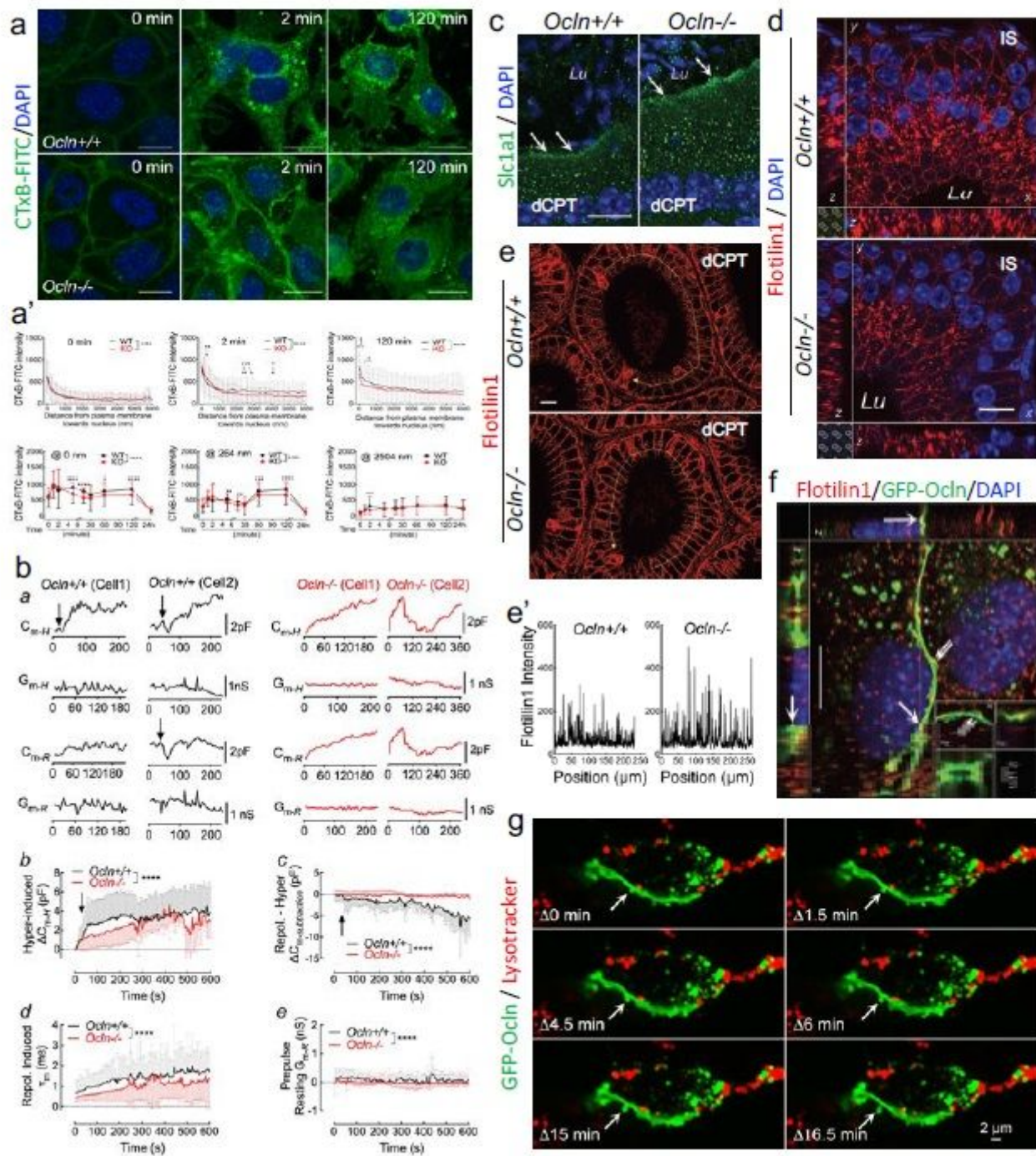


Figure 5

Ocn facilitates rafted plasma membrane and flotillin-microdomains retrieval and recycling via bulk-endocytosis a. Confocal images showing CTxB endocytosis assay on WT or Ocln-KO DC2 cells at various time points and quantification of CTxB fluorescence signals using images of same parameters. b. Whole-cell patch-clamp measurement of passive membrane properties of WT and Ocln-KO DC2 cells. (a) Whole-cell capacitance during repeatedly hyperpolarization (Cm-H) and repolarization (Cm-R) and conductances (Gm-H and Gm-R). (b) Changes of capacitance (ΔC_m) upon hyperpolarization of WT (n = 11) or Ocln-KO cells (n = 7). (c) Digital subtracted capacitance (ΔC_m -subtraction) of the repolarization-959 induced

capacitance from that of hypolarization-triggered response of the same cells. (d,e) Time constant of the raised current upon repolarization and the pre-pulse resting conductance of the same cells in b and c. Arrows: time lag before the sustained increment in membrane capacitance of WT cells. c. Increased of transporter Slc1a1 (arrows) in apical surface of dCPT principal cells of *Ocln*^{-/-} compared to *Ocln*^{+/+} mice. d. 3D-reconstruction images of immunostaining showing decreased flotillin in the intracellular vesicles of principal cells of KO IS epididymidis. e. Accumulated flotillin in the paracellular membranes of dCPT principal cells of *Ocln*⁻⁹⁶⁹ KO compared to WT mice. (e') Intensity profile of flotillin along the yellow arrows as in E. f. Immunofluorescent staining for flotillin with *Ocln*-N-GFP transfected DC2 cells. Insert: a nascent double-membrane-like vesicle budding from the paracellular membranes of two adjacent cells. g. Live-cell imaging showing endocytosis events at paracellular membranes of DC2 cells expressing WT-*Ocln*-GFP and loaded with lysotracker. Lu: Lumen. Scale bars: 10 μ m. Blue: DNA labelled with DAPI.

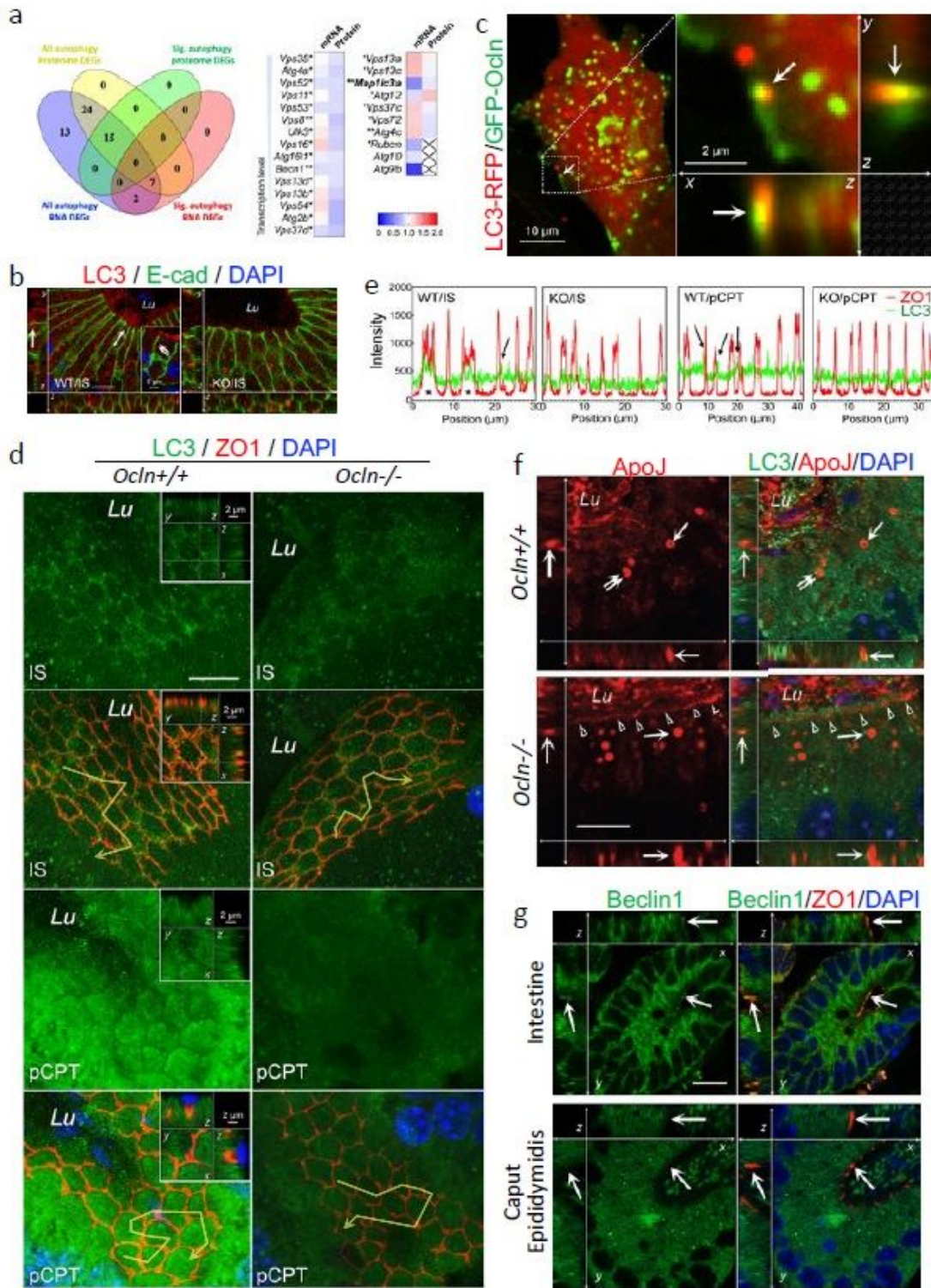


Figure 6

Ocln-promoted parapathy involves autophagy protein LC3 but not Beclin-1 a. Venn graph of the autophagy DEGs and heatmap of significant changed DEGs in the transcriptomic and proteomics of CPT epididymidis of *Ocln*^{+/+} vs *Ocln*^{-/-} mice. b. 3D-reconstruction confocal images of LC3 and E-cadherin in the IS segment of WT and KO mice showing the presence of vesicular-like structure at the apical domain of one WT principal cells. Insert: a phagocytotic-like large vesicle labelled for LC3 near the paracellular

membranes (double-arrow). c. Colocalization of LC3-RFP and OcIn-GFP in co-transfected DC2 cells. d. Confocal projection and 3D-reconstruction images (inserts) showing the colocalization of LC3 with ZO1 at the peri-TJ membranes in WT IS and pCPT epididymidis. Yellow arrows indicate the position for the intensity profiles as plotted in E. e. Asterisks: enriched LC3 levels in the ZO1-labeled paraphagic-like structures at TJs; arrows: increased LC3 near ZO1-labelled TJs in WT cells. f. Double-labelling of anti-LC3 and ApoJ in OcIn+/+ and OcIn-/- pCPT epididymidis. The LC3 on the ApoJ+ vacuoles is more frequent in WT (double-arrow) than in KO principal cells. A line of ApoJ is visible in the apical surface of KO principal cells but not in that of WT cells. g. The presence of Beclin-1 labelling on the TJs (ZO1) of intestine epithelial cells, but not in epididymal CPT epithelial cells. Scale bars: 10 μ m. Blue: DNA labelled with DAPI.

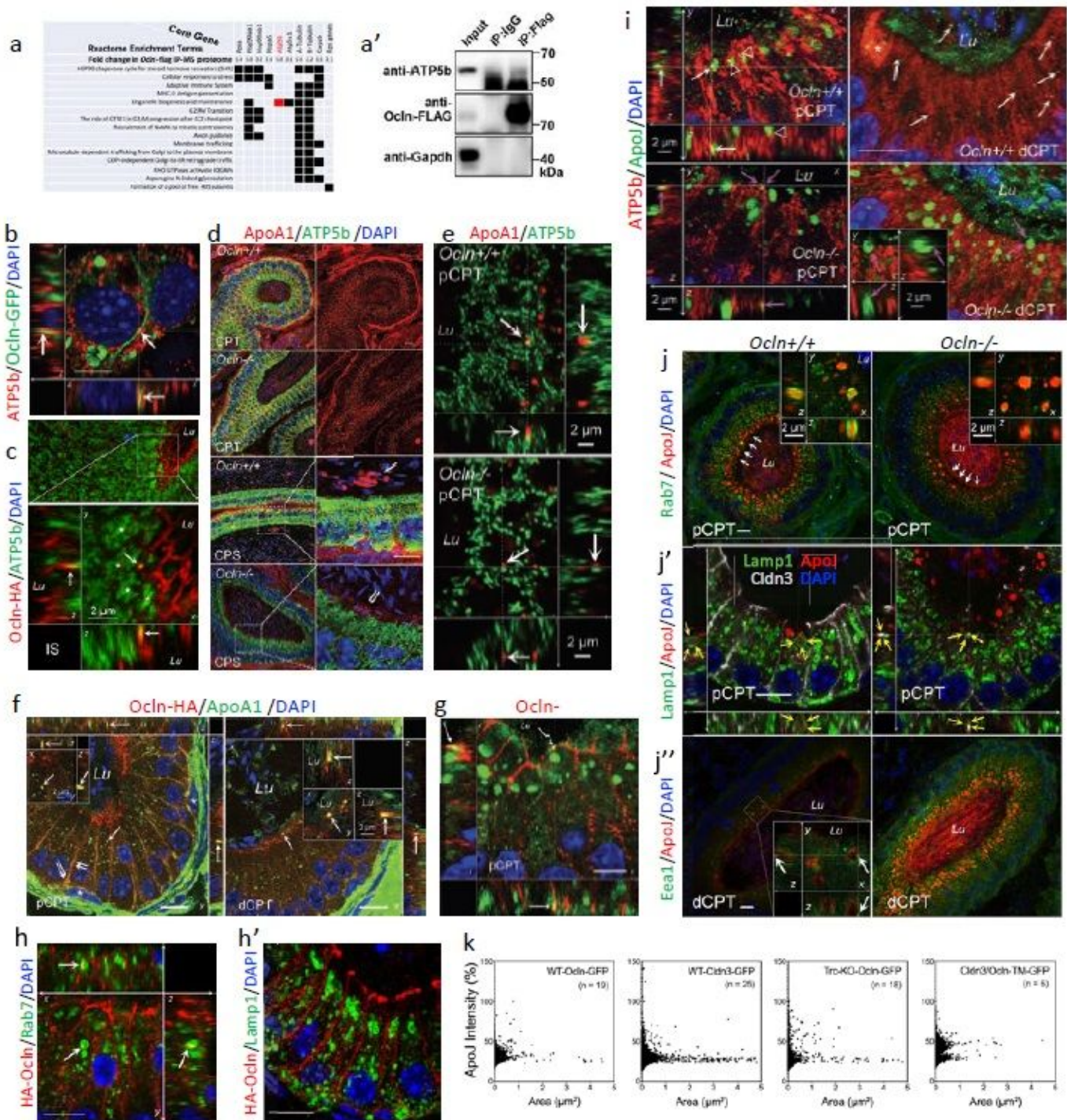


Figure 7

Ocln promotes the transport of ApoJ and ApoA1 to ATP5b in the caput epididymidis. **a**. Enrichment terms of IP-MS proteome from DC2 cells overexpressed Ocln-N-Flag plasmid. **(A)** Ocln-N-Flag protein co-IP with anti-flag antibody from overexpressed DC2 cells following immunoblotting for ATP5b. **b**. 3D-reconstruction image showing immunostaining of ATP5b with Ocln-N-GFP transfected DC2 cells. **c**. Confocal projection image and higher magnification 1007 of 3D-reconstruction images of ATP5b and HA-Ocln of mouse IS epididymidis. Arrows: co-localization of ATP5b and HA-Ocln at the TJ. **d**. Double-

immunostaining for ApoA1 and ATP5b in CPT and CPS epididymidis of *Ocln*^{-/-} and *Ocln*^{+/+} males. Arrow: the ApoA1-labelled cellular debris-like remnants surrounding WT sperm acrosomes. Double-arrow: weak ApoA1 in stereocilia of KO principal cells. e. 3D-reconstruction images for ApoA1 and ATP5b in pCPT of *Ocln*^{-/-} and *Ocln*^{+/+} mice. f. 3D-reconstruction images for ApoA1 and HA-Ocln of CPT segments. Inserts: strong co-localization in cargoes. Asterisks: weak ApoA1 and HA-Ocln levels on the surface of basal cells. Double-arrows: dynamics vesicular events at the paracellular membranes of principal cells. g. Co-localization of ApoJ and HA-Ocln in pCPT (arrows) at the TJ with a vesicle in close proximity. h. Co-localization of ATP5b and ApoJ in pCPT of *Ocln*^{-/-} and *Ocln*^{+/+} mice in the small vesicular structures (arrows). Asterisk: a clear cell. Magenta arrows: pm-W-DMV-like ApoJ⁺ vesicle at the apical paracellular space of principal cells. i. Double-immunostaining of Rab7 and Lamp1 with anti-HA of pCPT epididymidis from HA-Ocln mice. j. Subcellular localization of Rab7, Lamp and Eea1 with ApoJ in pCPT epididymidis of *Ocln*^{+/+} and *Ocln*^{-/-} mice. k. Scatter plot of ApoJ immunofluorescence profiles in the organelles of *Ocln*-KO DC2 cells transfected with the plasmid either of WT-Ocln-GFP, truncated Ocln-KO-GFP, or WT-Cldn3-GFP, or a rescue plasmid of Cldn3/Ocln-TM-GFP in which the four transmembrane domains of Cldn3 were replaced with those 1031 of Ocln. Data represent results of cell numbers as indicated. Lu: Lumen. Scale bars: 10 μ m. Blue: DNA labelled with DAPI.

Epithelial parapahgy

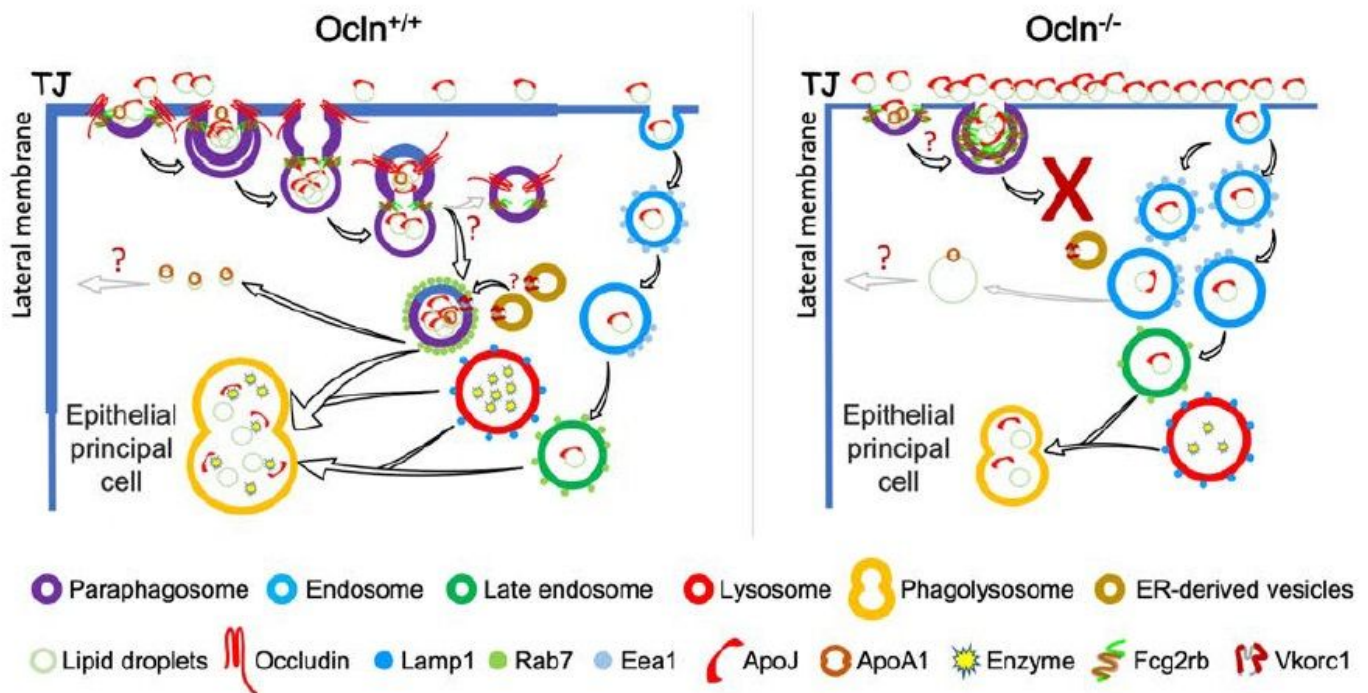


Figure 8

Schematic representation of parapahgy the TJs and transepithelial cholesterol transport of epithelial cells. *Ocln* in the epithelial cells of proximal compartment promotes parapahgy at TJs to take up lipophilic cargoes by involving surface membrane receptor *Fcgr2b* and intracellular HDL receptor *ATP5b*, subsequently facilitating raft-membrane retrieval and recycling. Paraphagosomes maintains

phagolysosome function and redox-promoted VK dependent MGP carboxylation, which in turn facilitates lipoprotein ApoJ uptake. Impaired paraphagy leads to cholesterol accumulation and ApoJ deposition in the distal compartment. For more details, see the main text.

Supplementary Files

This is a list of supplementary files associated with this preprint. Click to download.

- [50cInMETHODSFinal202101.docx](#)
- [FigureS14LYSOTRACKEROCNGFP.mov](#)
- [ParaphagyMETHODSFinal202101.docx](#)